

Investigation of Surface Electromagnetic Waves with Multi-Heterodyne Scanning Near-Field Optical Microscopy

THÈSE N° 4671 (2010)

PRÉSENTÉE LE 28 MAI 2010

À LA FACULTÉ SCIENCES ET TECHNIQUES DE L'INGÉNIEUR
LABORATOIRE D'OPTIQUE APPLIQUÉE
SECTION DE MICROTECHNIQUE

ÉCOLE POLYTECHNIQUE FÉDÉRALE DE LAUSANNE

POUR L'OBTENTION DU GRADE DE DOCTEUR ÈS SCIENCES

PAR

Tristan SFEZ

acceptée sur proposition du jury:

Prof. P.-A. Farine, président du jury
Prof. H. P. Herzig, directeur de thèse
Dr M.-P. Bernal, rapporteur
Prof. W. Nakagawa, rapporteur
Prof. V. Sandoghdar, rapporteur



ÉCOLE POLYTECHNIQUE
FÉDÉRALE DE LAUSANNE

Lausanne, EPFL

2010

In this thesis, we present the development of a tunable Multi-Heterodyne Scanning Near-Field Optical Microscope (MH-SNOM). This instrument has been built and evaluated for the investigation of optical near fields in amplitude, phase and polarization. With this microscope, the response of a structure illuminated with two orthogonally polarized beams can be simultaneously measured both in amplitude and phase. Moreover, the integral state of polarization at the surface of a specimen can be retrieved under specific conditions.

We demonstrate the capabilities of the system through a series of measurements involving Surface Electromagnetic Waves (SEWs). We have mainly focused our attention on a particular class of SEWs known as Bloch Surface Waves (BSWs). The propagation of BSWs on the outer surface of a silicon nitride multilayer has been studied in detail. Furthermore, we show that this propagation is affected by the presence of shallow dielectric corrugations such as a subwavelength grating or at the straight interface with a coated portion of the multilayer. In particular, we demonstrate that ultra-thin (thickness $< \lambda/10$) dielectric ridges may act as BSW waveguides. Combining the detection capabilities of the MH-SNOM with a numerical treatment of the experimental data, we are able to separate the transverse and longitudinal field components of the three modes propagating within a specific BSW waveguide. This new structure provides interesting opportunities in waveguide-based biosensing schemes in which the ridge is realized with functionalized molecular layers of nanometric thickness.

Finally, we investigate a structure sustaining another type of SEW: Surface Plasmon Polaritons (SPPs). This structure is designed for the asymmetrical coupling of SPPs at normal incidence. Through a detailed analysis of the spatial spectra, we show that, in addition to SPPs, the field contains other near-field components.

All these experiments demonstrate the expected MH-SNOM capabilities of measuring the amplitude, phase and polarization of optical near fields. The MH-SNOM therefore serves as a powerful tool for the investigation with subwavelength resolution of optical near fields generated in structures such as integrated optics, photonic crystals, cavities, resonators, etc.

Abstract

Keywords: heterodyne, multi-heterodyne, near field, scanning microscopy, SNOM, phase, polarization, multilayer, surface electromagnetic wave, Bloch surface wave, Snell, subwavelength grating, ridge waveguide, surface plasmon polariton, BLACES, asymmetric coupling.

Résumé

Dans cette thèse, nous présentons le développement d'un microscope optique en champ proche multi-hétérodyne et accordable (MH-SNOM). Cet instrument a été réalisé dans le but d'observer et de déterminer l'amplitude, la phase et la polarisation du champ proche. Ce microscope mesure simultanément, en amplitude et phase, la réponse d'une structure illuminée par deux faisceaux polarisés orthogonalement. Dans certaines conditions particulières, une mesure intégrale de l'état de polarisation à la surface de l'échantillon peut être effectuée.

Nous démontrons ses capacités par une série de mesures impliquant des ondes électromagnétiques de surface (*Surface Electromagnetic Waves* - SEWs). Nous avons principalement porté notre attention sur une classe particulière de SEWs connues sous le nom d'onde de Bloch de surface (*Bloch Surface Waves* - BSWs). Une étude détaillée de la propagation des BSWs à la surface d'un multicouche en nitrure de silicium a été réalisée. Nous montrons de quelle manière cette propagation est affectée par la présence de très fines corrugations diélectriques telles qu'un réseau sub-longueur d'onde, ou une marche diélectrique déposée sur le multicouche. En particulier, nous démontrons qu'une bande diélectrique ultrafine ($\lambda/10$) peut servir de guide d'onde pour les BSWs. Combinant les capacités de détection du MH-SNOM avec un traitement numérique des données expérimentales, nous sommes capables de séparer les composantes transverses et longitudinales des trois modes propageant dans un guide d'onde particulier. Cette nouvelle structure fournit d'intéressantes opportunités en bio-détection basée sur le guidage d'ondes de surface. Le guide pourrait en effet être réalisé par des couches de molécules fonctionnalisées et d'épaisseurs nanométriques.

Finalement, nous étudions une structure supportant un autre type d'ondes électromagnétiques de surface : les plasmons de surface (*Surface Plasmon Polaritons* - SPPs). Cette structure a été conçue pour le couplage asymétrique de SPPs à incidence normale. Au travers d'une analyse détaillée du spectre spatial, nous montrons qu'en plus des SPPs, le champ proche optique contient d'autres composantes singulières.

Toutes ces expériences démontrent les capacités prévues du MH-SNOM à mesurer l'amplitude, la phase et la polarisation du champ proche optique. Le MH-SNOM devient par conséquent un instrument puissant pour l'investigation sub-longueur d'onde de champs générés par des structures telles que les cristaux photoniques, les cavités, les résonateurs, etc.

Mots-clés: hétérodyne, multi-hétérodyne, champ proche, microscopie à balayage, SNOM, phase, polarisation, multicouche, onde optique de surface, onde de Bloch, Snell, réseau sub-longueur d'onde, guide d'onde rectangulaire, plasmon de surface, BLACES, couplage asymétrique.

Contents

Contents	5
1 Introduction	9
1.1 Classical diffraction limit	10
1.2 Scanning Near-field Optical Microscopy (SNOM)	11
1.3 Motivation and thesis outline	12
2 Heterodyne detection	17
2.1 Principle	18
2.2 Noise in the detection	20
2.2.1 Johnson noise	20
2.2.2 Shot noise	21
2.3 Amplitude and phase accuracy of the heterodyne detection	22
2.3.1 Signal to noise ratio	22
2.3.2 Amplitude and phase accuracy	24
2.4 Conclusion	25
3 Multi-heterodyne interferometry	27
3.1 States of polarization and orthogonality	28
3.1.1 Representation of a state of polarization	28
3.1.2 Orthogonality of two states of polarization	30
3.2 Multi-heterodyne principle	31
3.2.1 Multi-heterodyne interferometer	31
3.2.2 Optical field at the detection plane	32
3.3 Detection	33
3.3.1 Optical detection with one detector	34

CONTENTS

3.3.2	Optical detection with two detectors	36
3.4	Signal to noise ratio, amplitude and phase accuracy	39
3.5	Conclusion	42
4	MH-SNOM	43
4.1	Set-up	44
4.1.1	Optical interferometer	46
4.1.2	Detection system	48
4.1.3	Data acquisition	52
4.1.4	Probe motion	55
4.1.5	SNOM head	56
4.2	Amplitude and phase in polarization-sensitive mode	58
4.2.1	Field at the detector	58
4.2.2	Amplitude and phase accuracy	60
4.2.3	Complex Fourier analysis	63
4.3	Tunability	65
4.3.1	Power fluctuations due to wavelength tuning	65
4.3.2	Spurious heterodyne frequencies	68
4.3.3	Orthogonality of the reference and object channels	69
4.4	Phase drifts	71
4.5	Conclusion	72
5	Bloch Surface Waves at a planar interface	75
5.1	Amorphous silicon nitride multilayer	76
5.2	Far-field characterization	78
5.2.1	Far-field characterization technique	79
5.2.2	Propagation constant and attenuation length	80
5.3	Near-field experiment	81
5.4	Bloch surface waves near-field distribution	82
5.5	Field enhancement	87
5.6	Multilayer covered with a thin dielectric layer	89
5.7	Conclusion	91

6	BSWs in a multilayer covered by a dielectric grating	93
6.1	Experiment	94
6.2	Field at the band edges	96
6.3	Field outside the band edges	98
6.4	Conclusion	99
7	Refraction of Bloch surface waves	101
7.1	Experiment	102
7.2	Refraction of Bloch surface waves: intensity measurements	104
7.3	Refraction of Bloch surface waves: phase measurements	106
7.4	From near to far field	107
7.5	Conclusion	108
8	Ultra-thin ridge waveguides for Bloch surface waves	109
8.1	Experiment	112
8.2	Numerical method	112
8.3	Guiding Bloch Surface Waves	113
8.3.1	Near-field demonstration	113
8.3.2	Fundamental mode analysis	115
8.4	Detailed analysis of waveguide modes	117
8.4.1	Sample and calculations	117
8.4.2	Selective excitation of the modes	118
8.4.3	Vectorial components	121
8.4.3.1	Method	121
8.4.3.2	Phase correction	124
8.4.3.3	Transverse and longitudinal components	125
8.4.4	Dispersion relations of the modes	127
8.5	Conclusion	130
9	Asymmetrical excitation of SPPs on a blazed grating	133
9.1	Principle	135
9.2	Sample design and fabrication	136
9.3	Experiment	137
9.4	Analysis in the spatial domain	138
9.5	Analysis in the Fourier domain	141

CONTENTS

9.6 Conclusion	145
10 Conclusions	147
List of abbreviations	151
Bibliography	153
Acknowledgments	167
List of appendices	169
.1 Publications and conferences	171
.2 Curriculum Vitae	174
.3 Curriculum Vitae	175

1

Introduction

Since human beings began to consider the external world as a field of investigation, they dreamt of pushing their limits of perception to very distant and very small objects. In this regard, the invention of the lens initiated a new era extending the limits of human perception.

As early as 1683, Antony von Leeuwenhoek, a Dutch tradesman and unlikely scientist, built microscopes with a single, small lens displaying magnifications of up to 270x. This enabled him to discover protozoa (single-celled organisms). In 1873, Abbe published an important theoretical work revealing a fundamental limit – the classical diffraction limit – intrinsically limiting the resolution of the microscope. Scientists had to wait until 1984 for an important breakthrough in microscopy: the realization of the first near-field microscope. The classical diffraction limit was not a limit anymore.

1.1 Classical diffraction limit

In conventional microscopy, the sample is imaged with a lens, or a set of lenses, and a magnified image of the object is created. The interaction of the incident light with the structure generates propagating and non-propagating components in the immediate vicinity of the sample. While non-propagating components carrying the highly-detailed features remain confined very close to the interface (near field), the radiative components reach the imaging lens (far field) and construct the image. Only structures with lateral dimensions larger than

$$d_{min} = \frac{\lambda}{2n \sin \theta} \quad (1.1)$$

can be imaged with accuracy [1]. The medium n separating the sample and the imaging system, as well as the aperture angle θ , act therefore as a low-pass filter: some information is lost during the propagation from the near to the far field. The resolution however can be improved by decreasing the probe radiation wavelength λ . This fundamental limit is imposed by the physical nature of light itself and is known as *Abbe's barrier* or the *far-field diffraction limit*. It represents the lower bound to the size of the spatial features that can be resolved with a conventional microscope.

The limit of resolution is only slightly smaller than the wavelength of the probe illumination. For subwavelength resolution, the optical system should therefore be able to capture evanescent waves, which contain the high spatial frequencies and exist only in the immediate vicinity of the sample

In 1928, Synge, an Irish scientist, described an experimental scheme that would allow optical resolution to extend to the nanometer regime [2]. Given that visible light has wavelengths in the range 400 – 700 nm, this is significantly below the far-field diffraction limit. He proposed to generate a strong light source behind a thin, opaque metal film with a 100 nm diameter hole used as a very small light source. Such a tiny spot should be used to locally illuminate a thin biological specimen. In order to guarantee the local illumination, he required that the tiny source be closer than 100 nm from the sample. Images were to be recorded point by point detecting the light transmitted by the biological section by means of a sensitive photodetector. At the time, the proposed experiment was impractical because of the difficulties in placing a sample so close to a planar screen.

1.2 Scanning Near-field Optical Microscopy (SNOM)

With the invention of the Scanning Tunneling Microscope (STM) in 1982 [3], and shortly afterward the development of the Atomic Force Microscope (AFM) [4], the ability to position a sharp probe very close to a surface emerged. In the former, the Coulomb interaction is used to control the nanometric distance between the probe and the surface, whereas in the latter, inter-atomic forces contribute to the approach. STM and AFM provide topographical knowledge of the sample surface. The idea rapidly of replacing the existing probes with a subwavelength optical aperture at the apex of a sharply pointed transparent tip coated with metal rapidly emerged. In 1984, Pohl *et al.* from the IBM R uschlikon Research Laboratory realized the first Scanning Near-field Optical Microscope (SNOM) at a visible wavelength and showed image recordings with a resolution of $\lambda/20$ [5]. Independently, a similar scheme was proposed and developed by Lewis *et al.* at Cornell University [6].

The SNOM uses AFM techniques to position the probe close to the surface of the sample in order to detect the optical near-field. The probe can be used as a subwavelength sensor (collection mode), as a subwavelength emitter (illumination mode), as both (illumination/collection mode), or as a local near-field scatterer (apertureless SNOM). Commonly used probe designs include tapered optical fibers, functionalized probes based on fluorescent or metallic nanoparticles, and silicon/quartz micro-machined tips mounted on an AFM cantilever. A metal coating can be deposited at the apex in order to better define a small aperture.

Near-field microscopy implements many of the well known mechanisms used in classical microscopy, leading to a broad variety of SNOM configurations. Among them, we may cite interferometric techniques leading to phase measurements [7–10], spectroscopic methods that allow comparison of many images of the same scene at different wavelengths [11, 12], the polarization-contrast mechanism for structural analysis of materials [13, 14], fluorescence detection schemes dedicated to subwavelength biological applications or single molecule detection [15, 16], time-resolved techniques for the observation of the light pulse propagation within micro and nanostructures [17], or micro- and nano-lithography with the SNOM probe

[18, 19].

It is worth noting that SNOM is not the only method of overcoming the diffraction limit or investigating guided fields. In fluorescence microscopy, the Stimulated Emission Depletion (STED) microscope uses stimulated emission to saturate the fluorescence on an annular region around the fluorescent spot [20, 21], leading to a subwavelength fluorescent area. Other techniques rely on far-field imaging (real or Fourier space) and on a careful physical investigation of the losses [22–24], or introduce artificial scatterers such as gratings to convert a fraction of the evanescent field into propagating components [25, 26]. Compared to SNOM, they offer the advantage of fast direct imaging. However, their superresolution capabilities depend on the experimental configuration (i.e. the sample), which cannot be modified arbitrarily, whereas the SNOM resolution is linked to the probe size, which can be made extremely small. The coating of the probe also provides the net advantage of significantly suppressing unwanted background signals. The SNOM therefore remains the instrument of choice for a general approach to the investigation of near-field optical phenomena.

Nowadays, SNOM is an important tool for many research domains in optics. The development of SNOM gives rise to a large number of applications, in biology, materials science or surface chemistry, for example. In addition, in integrated photonics, SNOM is also required for the characterization of new nanostructured devices.

1.3 Motivation and thesis outline

At a given wavelength, a coherent optical field is fully characterized by its amplitude, phase and polarization. While near-field amplitude and phase measurements are routinely performed nowadays, measuring the polarization remains a delicate task. This is essentially due to the fact that the near-field polarization may show a highly three-dimensional (3D) orientation, whereas the propagation from the probe-sample system to the detector involves a propagative field, i.e., a field whose polarization has a two-dimensional (2D) orientation. A mapping of 3D to 2D fields therefore occurs, resulting in a loss of information if sufficient care is not taken.

The first and main motivation of this thesis is to build an instrument able to investigate the amplitude, phase and polarization properties of the optical near field generated by a structure. The strategy was to extract this information simultaneously through a multi-heterodyne interferometer working around $\lambda = 1550$ nm (C- and L-bands of telecommunications networks). The multi-heterodyne interferometer involves four beams: two orthogonal and linearly polarized reference beams and two orthogonal object beams. From a didactic point of view, the system may be seen in two different ways. Either we consider the interference produced by a particular reference beam with the two object beams, or the interference occurring between one specific object beam with the two reference beams. In the first case, the system simultaneously provides the amplitude and phase of the fields generated at the sample surface by two orthogonally polarized illuminating beams. The polarization contrast response of the structure is hence measured. With a standard heterodyne SNOM, this procedure would involve two successive measurements with a rotation of the object beam polarization. In the second case, the field collected by the probe is projected onto two orthogonal reference beams. The vectorial properties of the object beam are hence recorded, both in amplitude and phase. With a traditional heterodyne SNOM, this would also require two successive measurements with a rotation of the reference beam polarization. The multi-heterodyne SNOM (MH-SNOM) therefore simultaneously provides information that would necessitate four successive measurements with a standard heterodyne SNOM, with the great advantage that all of the signals can be accurately compared. These signals have indeed been acquired at exactly the same probe position with the assurance that the optical properties of the probe are the same (same state of deterioration). Although the optical properties of the probe are important, they are not investigated in this work.

The second goal of this thesis is to demonstrate the expected capabilities of the MH-SNOM through the characterization of micro-fabricated structures. We begin with some measurements on dielectric multilayers sustaining particular optical surface modes known as Bloch Surface Waves (BSWs). This activity sets the tone for later experimental work that mainly deals with BSWs. A related but distinct component of this work involves a different kind of surface optical mode: Surface Plasmon Polaritons (SPPs). The experimental work constituting

this thesis is thus in essence related to surface optical states. The dimensions of the structures involved do not necessarily possess highly subwavelength features, but the *direct* observation of surface states, which are by nature bound to the interfaces, requires the ability to observe the optical near field.

This thesis contains nine chapters. In **Chapter 2**, the basic concept of heterodyne detection is introduced. This interferometric technique provides an elegant and powerful way to measure the complex amplitude of an optical field. Considerations concerning the noise and the accuracy of this method are discussed. This chapter is strongly connected to **Chapter 3**, which develops a multi-heterodyne scheme devoted to polarization measurements. In addition to the description of the multi-heterodyne interferometer, two detection systems are discussed. The contrast between them highlights the capabilities and limitations of the MH-SNOM presented in this work.

Chapter 4 presents a detailed description of the tunable MH-SNOM. The development and investigation of this system is one of the primary goals of this thesis. This SNOM works in collection mode with dielectric or metal coated tapered optical fibers, and with wavelengths between 1460 and 1580 nm. We show how a multi-heterodyne interferometer can be combined with a scanning probe optical microscope with the aim of measuring the amplitude, phase and polarization in the near and far field. The concrete implementation of the system is presented, including hardware and software developments. The amplitude and phase accuracy are evaluated in order to correctly establish the detection accuracy for all further measurements. Then, the difficulties that arise because of the tunability are discussed. Finally, we assess the phase drifts occurring within the system.

Chapter 5 initiates a series of chapters on BSWs. A carefully designed dielectric multilayer sustaining BSWs is studied in detail. The spatial distribution of the mode, its propagation constant as well as its confinement (field enhancement) are measured. Comparisons with far-field measurements are provided. This multilayer constitutes the basic structure of the samples investigated in the following chapters.

In **Chapter 6**, the multilayer is covered with a shallow subwavelength dielectric grating that creates a bandgap within the wavelength range accessible by

the MH-SNOM. We will investigate the field behavior at the band edges as well as outside the bandgap. Interesting phenomena such as standing waves or light coupling through the -1 evanescent order of the grating are directly observed.

Chapter 7 investigates another ultra-thin dielectric structure deposited on the multilayer. In this study, we use the interface of a wide dielectric ridge to carry out an experiment demonstrating the refraction of BSWs. Measurements reveal that the BSWs in the multilayer behave as 2D waves, and that their refraction can be described by the well known Snell's law.

In **Chapter 8**, polarization-resolved measurements are reported. We follow with the concept of dielectric ridges deposited on the multilayer and show that they can be used as ultra-thin (thicknesses $\lambda < 10$) BSW waveguides. For a particular waveguide structure, we demonstrate through near-field measurements that it sustains three modes and show how to independently excite them by tuning the wavelength and choosing the incident polarization. The individual dispersion curves of the three modes are also measured. Exploiting the ability of the MH-SNOM detect two arbitrary orthogonal components of paraxial (perpendicular to the probe axis) near fields, we show how a numerical treatment of the experimental data leads to the vectorial components of the modes.

Chapter 9 deals with SPPs. A subwavelength periodic structure designed for asymmetrical coupling of SPPs at normal incidence is characterized. This experiment illustrates the difficulty of measuring weak phenomena in the vicinity of an intense optical field (the zero order undiffracted beam). A Fourier analysis of the complex fields enables the discrimination of SPPs and other near-field components.

Finally in **Chapter 10**, we conclude this work and summarize its main results.

The entire development of the MH-SNOM has been carried out within the framework of a project supported by the *Swiss National Science Foundation*. Although the majority of the work presented in this thesis was performed by the author, a number of elements were the result of collaborative efforts. The structures involving the silicon nitride multilayers were mainly designed and realized at the Materials and Microsystems Laboratory χ Lab, Politecnico di Torino, Italy. Some of the far-field characterization of these structures was performed at

the Dipartimento di Energetica, SAPIENZA, Università di Roma and CNISM, Italy. The calculations related to the ultra-thin ridge waveguide for BSWs were performed at the Nanophotonics and Metrology Laboratory, Ecole Polytechnique Fédérale de Lausanne, Switzerland. The design and fabrication of the asymmetrical coupler for SPPs was carried out at the Department of Physics and Mathematics, University of Joensuu, Finland.

2

Heterodyne detection

Optics is the branch of physics which studies the behavior and properties of light, including its interactions with matter and the construction of instruments that use or detect it. Optics usually describes the behavior of visible, ultraviolet, and infrared light. At these wavelengths, the frequency of the electromagnetic field is so high (typically 10^{14} Hz in the visible range) that photodetectors cannot follow the instantaneous oscillation of the electric field. They only detect the time-averaged energy that hits them, i.e., the intensity of the light. This measurement is incomplete (even when neglecting other degrees of freedom such as polarization) because an electromagnetic field has not only an intensity, but also a phase, which is systematically lost in such a measurement. The phase part contains valuable information about the specimen under study. For example, it can reveal refractive index differences, the propagation directions of field components, the effective wavelength in media, differences in optical paths, etc. Dealing with the phase is

one of the major concerns of interferometry. This technique has become crucial for scientific and industrial purposes since the development of the laser in the 1960's.

Interferometric techniques based on phase shifting (dynamic technique) can be placed in two categories: quasi-heterodyne and heterodyne interferometry [27]. In the quasi-heterodyne technique, the relative phase difference between the interferometer arms is changed step-wise, using at least three different values. This technique is suitable for moderate phase resolutions ($\lambda/100$) and allows recordings of two-dimensional interference patterns with CCD cameras. The phase information is then deduced at any point of the image. However, the step-wise translation of the reference can be replaced with a continuously increasing phase shift, i.e., a frequency shift. This technique is known as heterodyne interferometry and leads to phase resolutions up to $\lambda/1000$ [28].

Although the optical heterodyne technique has been known since the beginning of the 1960's, the first description and realization of a phase-resolving heterodyne interferometer is due to Polster [29] in 1969. In the past, several methods have been developed to shift the frequency. Among them, we may cite Bragg reflectors [30], rotating half-wave plates [29], or rotating radial gratings [31]. The improvements in high-power and high-frequency power supplies brought commercial Bragg reflectors – also known as Acousto-Optic Modulators (AOMs) – to become the most reliable solution.

2.1 Principle

The basic idea of heterodyne detection is to introduce a small frequency shift between the two interfering beams [28]. A typical heterodyne interferometer is shown in Fig. 2.1. The laser light of frequency ν is separated with a beam splitter (BS) into two beams. These two beams constitute the reference and the object channels, and their frequencies are respectively shifted by f_1 and f_2 by means of AOMs. They are finally superposed with a second BS before reaching the photodetector. The frequency difference $\Delta f = f_2 - f_1$ leads to a sinusoidal beat signal whose frequency is chosen to be small enough to fall within the bandwidth of the detector. In principle, only one AOM is required to generate a frequency

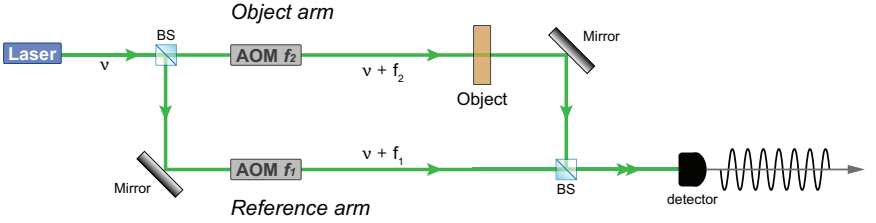


Figure 2.1: (Color online) Typical heterodyne interferometer.

difference. However, as typical AOM frequencies are in the MHz range, two AOMs whose frequency difference lies in the kHz range lead to a beat signal easily measured with common lock-in amplifiers.

In scalar theory, the object and reference waves can be describe by their complex signal

$$V_o = \text{Re}\{A_o e^{i\varphi_o} \cdot e^{i2\pi(\nu+f_1)t}\} \quad (2.1)$$

$$\text{and } V_r = \text{Re}\{A_r e^{i\varphi_r} \cdot e^{i2\pi(\nu+f_2)t}\}. \quad (2.2)$$

At the detector plane, the superposition of the reference and the signal leads to an intensity

$$I = A_o^2 + A_r^2 + 2A_o A_r \cos[2\pi\Delta f t + (\varphi_o - \varphi_r)]. \quad (2.3)$$

The interference between the reference wave r and the object wave o produces a sinusoidal intensity modulation of amplitude $2A_o A_r$ at the beat frequency Δf , superposed on a dc signal $A_o^2 + A_r^2$. Since A_o and φ_o are constant, the object information is therefore given by the amplitude $2A_o A_r$ and the relative phase $\varphi_o - \varphi_r$. Both amplitude and phase of the sinusoidal modulation can be measured by means of synchronous detection, i.e., by comparing it with a known electronic signal of same frequency.

The great advantage of heterodyne detection can be seen from Eq. 2.3. In static or quasi-heterodyne interferometric techniques ($\Delta f = 0$), the interference term is a mixture of the object amplitude and phase. A step-wise phase shift must therefore be introduced in the reference to measure them. In heterodyne

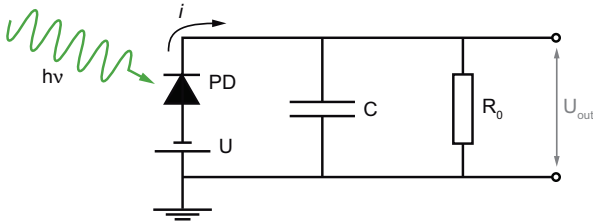


Figure 2.2: (Color online) Schematic electronic circuit of the detector. It consists of a photodiode PD (with bias voltage U), a capacitor C and a resistor R_0 . The output voltage is U_{out} .

detection, the object phase can be measured essentially independently of the amplitude of the modulated signal: the optical phase difference is converted into the phase of the beat frequency signal.

2.2 Noise in the detection

The study of the noise in the detection process is of great importance because it is the main factor that affects the accuracy of the measurements. In the context of heterodyne detection, the noise will alter the amplitude and phase accuracy. The noise in the detection process mainly arises at the photodetector level. The detector is composed of a photodiode and an electronic circuit. The photodetection involves several sources of noise. However, the dominant contributions are Johnson noise and the shot noise.

2.2.1 Johnson noise

A schematic view of the electronic circuit constituting the photodetector is shown in Fig. 2.2. The incoming photons of energy $h\nu$ are converted into photoelectrons by the photodiode PD, and collected by the capacitor C . The photodiode is supplied with a bias voltage U . The resistor R_0 is added to create a current i that leads to an output voltage U_{out} . This RC circuit introduces a limited bandwidth B for the detection.

Johnson noise, or Nyquist noise, describes the voltage fluctuations across a dissipative circuit element. These fluctuations are most often caused by the thermal motion of the electrons. That is why this source of noise is also referred as *thermal noise*. Thermal noise is independent of the detected optical power and its power P_{TN} can be expressed at the output of the detector as [32]

$$P_{TN} = 4kTB, \quad (2.4)$$

where $k = 1.38 \cdot 10^{-23}$ J/K is the Boltzmann constant, and T the absolute temperature.

2.2.2 Shot noise

Shot noise, or quantum noise, is a fundamental noise limit that arises because of the discrete nature of light. When the energy quanta (photons) hit the detector, photoelectrons are created according to a Poisson distribution [33]. The variance of the shot noise is therefore equal to the mean number of collected photoelectrons n_e during a characteristic time interval, called integration time $\tau = 1/(2B)$, where B is the detection bandwidth [33]. The ratio of the number of photoelectrons n_e to the number of impinging photons n_p is called the *quantum efficiency* $\eta = n_e/n_p$ ($\eta_{max} = 1$). The ratio of the current i (proportional to the photoelectrons produced per unit of time) and the optical power P_{opt} is called the *spectral sensitivity*

$$S = \frac{i}{P_{opt}} = \frac{\eta e}{h\nu}, \quad (2.5)$$

where $e = 1.602 \cdot 10^{-19}$ A · s is the elementary charge, $h = 6.626 \cdot 10^{-34}$ J · s the Planck's constant and ν the light frequency. An accurate look at current generated by the shot noise shows that it is composed of two contributions [32]: the current i_{p-n} produced by the conversion of the photons and the dark-current i_d , which is the remaining current when the photodetector is not exposed to light. Within the detection bandwidth B , the electric power corresponding to the shot noise generated by the circuit on Fig. 2.2 is [32]

$$P_{SN} = 2eB(SP_{tot} + i_d)R_0, \quad (2.6)$$

where $P_{tot} = P_r + P_o$ is the sum of the reference and object power. In the following work, the reference will be large enough to exceed considerably the dark current

i_d . The electrical power generated by the shot noise at the output of the detector becomes therefore

$$P_{SN} = 2eBS P_{tot} R_0. \quad (2.7)$$

2.3 Amplitude and phase accuracy of the heterodyne detection

2.3.1 Signal to noise ratio

The *signal to noise ratio* (SNR) in heterodyne detection is defined by the ratio of the electrical heterodyne signal P_{AC} to the total noise power P_N :

$$\text{SNR} = \frac{P_{AC}}{P_N} = \frac{P_{AC}}{P_{SN} + P_{TN}}. \quad (2.8)$$

The heterodyne optical power at the photodiode is deduced from Eq. 2.3

$$P(t) = P_o + P_r + 2\sqrt{P_o P_r} \cos(2\pi\Delta ft + \varphi), \quad (2.9)$$

where P_o and P_r are the object and reference power respectively, and $\varphi = \varphi_o - \varphi_r$. This equation represents however an ideal case. In reality, the amplitude of the signal is reduced by a factor m ($0 \leq m \leq 1$), called the *relative interference amplitude* [34]. This factor accounts for the interference quality, i.e., the polarization, the temporal and spatial coherence. Equation 2.9 then becomes

$$P(t) = P_{tot} + 2m\sqrt{P_o P_r} \cos(2\pi\Delta ft + \varphi). \quad (2.10)$$

From Eq. 2.5, the current generated by the photodiode is

$$\begin{aligned} i(t) &= S \left[P_{tot} + 2m\sqrt{P_o P_r} \cos(2\pi\Delta ft + \varphi) \right] \\ &= i_{dc} + i_{ac} \cos(2\pi\Delta ft + \varphi), \end{aligned} \quad (2.11)$$

where $i_{dc} = SP_{tot}$ is the *dc* current, and $i_{ac} = 2mS\sqrt{P_o P_r}$ the amplitude of the *ac* current $i(t) = i_{ac} \cos(2\pi\Delta ft + \varphi)$. The electrical power of the heterodyne signal is therefore

$$P_{AC} = R_0 \langle i_{AC}^2 \rangle = \frac{1}{2} R_0 i_{ac}^2 = 2m^2 S^2 P_o P_r R_0. \quad (2.12)$$

2.3 Amplitude and phase accuracy of the heterodyne detection

The SNR definition 2.8 becomes

$$\text{SNR} = \frac{m^2 S^2 P_o P_r R_0}{e B S R_0 (P_o + P_r) + 2kTB}. \quad (2.13)$$

As the reference contributes to the shot noise power, it can be increased up to the point where shot noise exceeds Johnson noise. In this case the detection is called *shot noise limited* and only the unavoidable discrete nature of light significantly contributes to the noise.

The minimum reference power P_r^{min} leading to shot noise limited detection can be derived from Eqs. 2.4 and 2.7. Stating $P_{SN} = P_{TN}$ and assuming $P_r \gg P_o$, we get

$$P_r^{\text{min}} = \frac{2kT}{eR_0S}. \quad (2.14)$$

If we keep increasing P_r , the SNR reaches a constant value

$$\text{SNR} = \frac{P_{AC}}{P_{SN}} = m^2 \frac{\eta}{h\nu B} \frac{P_o P_r}{P_o + P_r}. \quad (2.15)$$

When $P_r \gg P_o$ and $m = 1$, it becomes

$$\text{SNR} = \frac{\eta}{h\nu B} P_o. \quad (2.16)$$

The above equation can be rewritten by considering the number of photoelectrons n_e^o and photons n_p^o corresponding to the power P_o . The number of photons received during the integration time $\tau = 1/(2B)$ is $n_p^o = \tau P_o/h\nu$. Equation 2.16 can therefore be expressed as

$$\text{SNR} = 2 \frac{\tau P_o}{h\nu} \eta = 2n_e^o. \quad (2.17)$$

This equation clearly shows that if $P_r \gg P_o$ and $P_r \gg P_r^{\text{min}}$, then the SNR is only limited by shot noise. Compared to direct detection, the SNR is increased by a factor of 2, called the *heterodyne gain*. It is worth noting that the higher the quantum efficiency η , the higher the SNR. This is the reason InGaAs photodiodes are preferred to photomultipliers for wavelengths around $\lambda = 1500$ nm. The quantum efficiency of a photodiode is indeed larger than that of a photomultiplier ($\eta_{\text{InGaAs}} \simeq 85\%$, $\eta_{\text{PM}} \leq 10\%$).

The bandwidth B comes from the detector electronics. However, it can be drastically decreased using a post-detection measurement system such as a lock-in

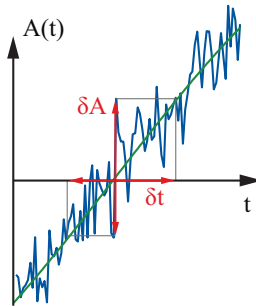


Figure 2.3: (Color online) Zero-crossing for a noisy time-dependent heterodyne signal.

amplifier or a spectrum analyzer. For example, the detector used in the following work has a bandwidth of 7.5 MHz (see Sec. 4.1.2), whereas a lock-in amplifier with an integration time of 10 ms has a typical bandwidth of 25 Hz.

2.3.2 Amplitude and phase accuracy

From Eq. 2.9, the time-dependent optical heterodyne signal is

$$P(t) = 2\sqrt{P_o P_r} \cos(2\pi\Delta f t + \varphi), \quad (2.18)$$

with an optical amplitude $P_0 = 2\sqrt{P_o P_r}$ and a phase $\phi = 2\pi\Delta f t + \varphi$. The measured electric heterodyne amplitude A is therefore proportional to $\sqrt{P_0}$: $A = b\sqrt{P_0}$, where b is a constant. In the presence of optical noise P_N , the electric amplitude fluctuations $\delta A = b\sqrt{P_N}$ lead to a relative standard deviation of amplitude

$$\frac{\delta A}{A} = \frac{1}{\sqrt{SNR}}. \quad (2.19)$$

The amplitude fluctuations generate an uncertainty on the time δt as depicted in Fig. 2.3. This uncertainty is maximal for zero-crossing and $\delta t = \delta A / (2\pi\Delta f A)$. Since the phase and the time fluctuations are related through $\delta\phi = 2\pi\Delta f \delta t$, the accuracy of the phase measurement becomes

$$\delta\phi = \frac{1}{\sqrt{SNR}}. \quad (2.20)$$

It is instructive to present a numerical example that shows the order of magnitude of the quantities involved in a typical case. Let us assume shot noise-limited detection with an object power $P_o = 1$ pW, a bandwidth of 25 Hz, a quantum efficiency $\eta = 85\%$ and a wavelength $\lambda = 1520$ nm. From Eq. 2.17, we find $n_e^o \simeq 130 \cdot 10^3$ and a SNR of about 54 dB. The amplitude and phase accuracy become $\delta A/A \simeq 2 \cdot 10^{-3}$ and $\delta\varphi \simeq 2$ mrad (0.1 deg or $2\pi/3180$).

The condition of shot noise-limited detection is reached when $\text{SNR} = 1$. From Eq. 2.17, it corresponds to half a photoelectron ($n_e^o = 1/2$) arising from the object power P_o . The minimum detectable power therefore becomes

$$P_o^{min} = \frac{h\nu B}{\eta}. \quad (2.21)$$

Using the previous example, $B = 25$ Hz, $\eta = 1$, $\lambda = 1500$ nm, the minimum detectable optical power with heterodyning is found to be $P_o^{min} = 3.8 \cdot 10^{-18}$ W. As the photon energy is $h\nu = 1.3 \cdot 10^{-19}$ J, this corresponds to nearly 30 photons.

2.4 Conclusion

With the aim of gaining better amplitude and phase resolution, heterodyne detection proves to be a powerful technique compared to step-wise interferometric methods. With this technique, shot noise limited detection can be reached at the expense of a minor effort: an increase of the reference power. Moreover, the signal to noise ratio is enhanced by a factor of 2 with respect to direct detection. Together with the fact that the detection bandwidth B can be made very small through a post-detection process, signal to noise ratio greater than 50 dB are easily obtained. Optical signals as low as 10^{-18} W can be detected with a phase accuracy of approximately $2\pi/3000$. In practice, this accuracy is however limited by optical and mechanical stability, and by the resolution of digital data acquisition devices.

Based on this robust method for measuring amplitude and phase, a more complex system will be presented in the next chapter. The motivation for this system is to measure the third unknown parameter of the optical field: the polarization.

3

Multi-heterodyne interferometry for polarization measurements

In the last chapter, the standard heterodyne detection has been discussed. This technique involves two heterodyne arms: the reference and object channels. It is suitable for amplitude and phase detection. In the present chapter will be presented an interferometer involving four heterodyne channels: two reference and two object arms. Throughout this work, the term *multi-heterodyne* will refer to this specific four-channel interferometer. The particular configuration of this interferometer makes it suitable for polarization detection without involving step-wise measurements. The problem of retrieving the state of polarization (SOP) of the field at the surface of a sample should be clearly separated into two distinct issues. The first is to measure the SOP at the detection plane (detector). The second consists of finding the polarization transfer function that relates the field in the detection plane to the field at the sample level. In this chapter, we only

consider the polarization in the detection plane.

As the polarization is of concern, a first section will briefly recall how to fully characterize a SOP and what orthogonality between two SOPs means. In the next section, the canonical arrangement of the multi-heterodyne interferometer will be presented. Two detection systems involving respectively one and two detectors will then be discussed. Although only the single detector system has been implemented, the contrast between these two methods highlights the capabilities and limitations of the developed system. Finally, we will show how to evaluate the associated signal to noise ratios and their corresponding amplitude and phase accuracies.

3.1 States of polarization and orthogonality

3.1.1 Representation of a state of polarization

In the most general case, the polarization of light is determined by the temporal evolution of the orientation of the electric-field vector. For coherent and monochromatic light, it describes an ellipse whose orientation and characteristics depend on the position in space. In this work, light will always be detected with detectors placed in front of fiber outputs: paraxial optics holds¹. The ellipse therefore lies in a plane orthogonal to the propagation direction, and the electric field may be described by a 2D vector field.

In a Cartesian coordinate system $(\hat{\mathbf{x}}, \hat{\mathbf{y}})$, a monochromatic electric field \mathbf{E} may be expressed by

$$\mathbf{E} = \begin{pmatrix} A_x e^{i\varphi_x} \\ A_y e^{i\varphi_y} \end{pmatrix} e^{i(\mathbf{k}\mathbf{r} - \omega t)}, \quad (3.1)$$

where the complex vector preceding the exponential function is known as the Jones vector ($A_x, A_y > 0$). The expression of \mathbf{E} is complex and the physical quantity is obtained by taking its real value.

The SOP is fully characterized by the three parameters A_x , A_y and the relative phase difference $\delta = \varphi_y - \varphi_x$. According to the sign of the respective spatial and

¹We consider here the detector and not the SNOM probe. Indeed, the near field may show highly non-paraxial behavior.

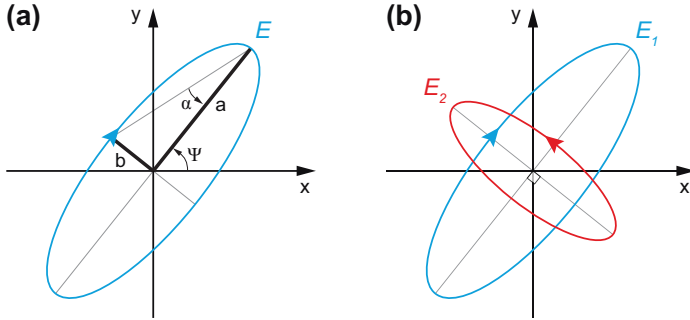


Figure 3.1: (Color online) (a) The elliptical representation of a SOP for monochromatic and coherent light. (b) Two elliptical and orthogonal SOPs.

time dependencies, the sense of rotation of the electric field on the polarization ellipse is left-handed if $0 < \delta < \pi$ and right-handed $-\pi < \delta < 0$. If $\delta = 0$ or $\delta = \pi$, the SOP is linear.

An elliptically right-handed SOP is represented in Fig. 3.1 (a). The inclination angle Ψ (also called *azimuth*) of its major axis with respect to $\hat{\mathbf{x}}$ can be calculated from

$$\tan(2\Psi) = \frac{2A_x A_y}{A_x^2 - A_y^2} \cos \delta. \quad (3.2)$$

An alternative formula is obtained by introducing the angle γ defined by $\tan(\gamma) = A_y/A_x$ ($0 \leq \gamma \leq \pi/2$) from which Eq. 3.2 becomes

$$\tan(2\Psi) = \tan(2\gamma) \cos(\delta). \quad (3.3)$$

This later parameter allows the determination of an important parameter of the ellipse – its *ellipticity* – defined by the ratio a/b of the major and the minor axes. The ellipticity can be calculated through the additional angle α such that $\tan(\alpha) = \pm b/a$ ($-\pi/4 \leq \alpha \leq \pi/4$), and is related to γ and δ by

$$\sin(2\alpha) = \sin(2\gamma) \sin(\delta). \quad (3.4)$$

From a geometrical point of view, a SOP is defined by the azimuth Ψ , the ellipticity α (which contains the handedness) and one of its axes, a or b .

When light passes through an optical element, its SOP can be altered. Within the Jones formalism, the optical element is described by a 2×2 complex matrix J – called the Jones matrix – that, multiplied with the Jones vector, generates the complex field at the output of the optical element.

3.1.2 Orthogonality of two states of polarization

Two coherent monochromatic beams are said to be orthogonal if they do not interfere. As interference is observed with conventional detectors (eyes, photodiodes, etc.) that are not able to follow the instantaneous oscillations of the electric field, the orthogonality is a time averaging concept. It is hence possible for two beams to be orthogonal even if at a given time their instantaneous electric fields are not.

Let us consider two electromagnetic fields

$$\mathbf{E}_1 = \begin{pmatrix} A_{1x} e^{i\varphi_{1x}} \\ A_{1y} e^{i\varphi_{1y}} \end{pmatrix} e^{i(\mathbf{kr} - \omega t)} \quad \text{and} \quad \mathbf{E}_2 = \begin{pmatrix} A_{2x} e^{i\varphi_{2x}} \\ A_{2y} e^{i\varphi_{2y}} \end{pmatrix} e^{i(\mathbf{kr} - \omega t)}. \quad (3.5)$$

The total intensity corresponding to the superposition of these two fields is

$$I = [\mathbf{E}_1 + \mathbf{E}_2] \cdot [\mathbf{E}_1 + \mathbf{E}_2]^*. \quad (3.6)$$

With the expressions of \mathbf{E}_1 and \mathbf{E}_2 , this intensity becomes

$$\begin{aligned} I = & A_{1x}^2 + A_{1y}^2 + A_{2x}^2 + A_{2y}^2 \\ & + 2A_{1x}A_{2x} \cos(\mathbf{kr} + \varphi_{2x} - \varphi_{1x}) + 2A_{1y}A_{2y} \cos(\mathbf{kr} + \varphi_{2y} - \varphi_{1y}). \end{aligned} \quad (3.7)$$

The last two terms represent the interference phenomenon. For orthogonal SOPs, their sum should be zero *at any position* \mathbf{r} , i.e., the two contributions cancel each other. A short mathematical development leads to the orthogonality conditions

$$\begin{cases} A_{1x}A_{2x} = A_{1y}A_{2y}, \\ (\varphi_{2x} - \varphi_{1x}) - (\varphi_{2y} - \varphi_{1y}) = n\pi, \quad n \text{ odd.} \end{cases} \quad (3.8)$$

If a system is able to provide the individual amplitudes and phases, it becomes straightforward to verify their orthogonality with the above equations.

From a geometrical point of view, two SOPs are orthogonal if their azimuth angles differ by $\pi/2$, they have opposite handednesses, and their ellipticities are identical. Figure 3.1 (b) shows two elliptical and orthogonal SOPs.

3.2 Multi-heterodyne principle

In this section, the multi-heterodyne interferometer is presented and the expression for the field intensity *at the detection plane* derived. Two particular detection systems, involving one or two detectors, are described, although only the one-detector solution has been implemented in this work. The contrast between these two configurations leads to a better understanding of the fundamental differences between a polarization-sensitive measurement and a polarization-resolved measurement. The polarization-sensitive technique measures the response of a sample under two differently polarized illuminating beams, but does not resolve the SOPs themselves at the sample surface.

3.2.1 Multi-heterodyne interferometer

The canonical form of the multi-heterodyne interferometer involved in this work is shown in Fig. 3.2. The laser light of frequency ν and arbitrary polarization is separated into two beams with a beam splitter (BS). The two generated beams constitute the *reference* and *object* arms. Each beam is again split into two linear and orthogonal SOPs using polarizing beam splitters (PBSs). The four resulting beams are labeled with indices 1 and 2 for the reference beams, 3 and 4 for the object beams.

The four channels then pass through Acousto-Optics Modulators (AOMs) driven at different frequencies f_1 , f_2 , f_3 and f_4 . Both the reference and object channels are then recombined with PBSs. We finally end up with one reference arm and one object arm consisting of the superposition of two linear and orthogonal SOPs labeled with the frequencies (f_1, f_2) and (f_3, f_4) respectively. This technique is also known as beam labeling.

While passing through the sample under investigation, the object beams may undergo amplitude and phase variations that lead to polarization changes,

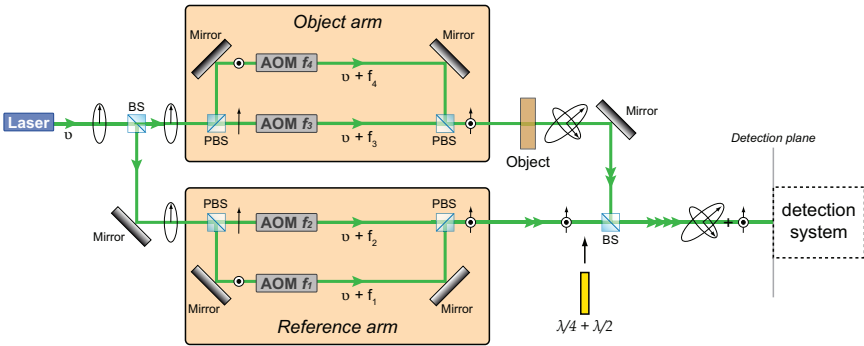


Figure 3.2: (Color online) Typical view of a 4-channel multi-heterodyne interferometer. An additional quarter-wave plate may be introduced in the reference arm to convert the linear state of polarization of the references into circular states.

schematically represented by ellipses. Finally, the reference and object channels are recombined with a BS and sent to the detection system. In the simplest case, the detection system consists of one detector. The capabilities of the single-detector system will be discussed in Sec. 3.3.1. An interesting detection set-up involving two detectors will be considered in Sec. 3.3.2. For reasons that will become clear later, the latter method requires a quarter-wave plate, shown in Fig. 3.2, to convert the linear and orthogonal SOPs of the references into circular and orthogonal SOPs.

3.2.2 Optical field at the detection plane

Let us express the four beams reaching the detection system of Fig. 3.2

$$\begin{aligned} \mathbf{E}_1 &= \begin{pmatrix} A_{1x} e^{i\varphi_{1x}} \\ A_{1y} e^{i\varphi_{1y}} \end{pmatrix} e^{i2\pi(\nu+f_1)t}, & \mathbf{E}_2 &= \begin{pmatrix} A_{2x} e^{i\varphi_{2x}} \\ A_{2y} e^{i\varphi_{2y}} \end{pmatrix} e^{i2\pi(\nu+f_2)t}, \\ \mathbf{E}_3 &= \begin{pmatrix} A_{3x} e^{i\varphi_{3x}} \\ A_{3y} e^{i\varphi_{3y}} \end{pmatrix} e^{i2\pi(\nu+f_3)t}, & \mathbf{E}_4 &= \begin{pmatrix} A_{4x} e^{i\varphi_{4x}} \\ A_{4y} e^{i\varphi_{4y}} \end{pmatrix} e^{i2\pi(\nu+f_4)t}. \end{aligned} \quad (3.9)$$

These relations express the four fields in an arbitrary basis ($\hat{\mathbf{x}}, \hat{\mathbf{y}}$) at the detection plane. We emphasize that the phases appearing in these expressions account for

the optical path differences. In the case of the object channels, they also contain the phase delays generated by the sample. The total intensity at the detector becomes

$$I(t) = |\mathbf{E}(t)|^2 = [\mathbf{E}_1 + \mathbf{E}_2 + \mathbf{E}_3 + \mathbf{E}_4] \cdot [\mathbf{E}_1 + \mathbf{E}_2 + \mathbf{E}_3 + \mathbf{E}_4]^*, \quad (3.10)$$

or in expanded form

$$\begin{aligned} I(t) = & A_{1x}^2 + A_{1y}^2 + A_{2x}^2 + A_{2y}^2 + A_{3x}^2 + A_{3y}^2 + A_{4x}^2 + A_{4y}^2 \\ & + 2A_{1x}A_{2x} \cos(2\pi f_{21}t + \varphi_{21x}) + 2A_{1y}A_{2y} \cos(2\pi f_{21}t + \varphi_{21y}) \\ & + 2A_{1x}A_{3x} \cos(2\pi f_{31}t + \varphi_{31x}) + 2A_{1y}A_{3y} \cos(2\pi f_{31}t + \varphi_{31y}) \\ & + 2A_{1x}A_{4x} \cos(2\pi f_{41}t + \varphi_{41x}) + 2A_{1y}A_{4y} \cos(2\pi f_{41}t + \varphi_{41y}) \quad (3.11) \\ & + 2A_{2x}A_{3x} \cos(2\pi f_{32}t + \varphi_{32x}) + 2A_{2y}A_{3y} \cos(2\pi f_{32}t + \varphi_{32y}) \\ & + 2A_{2x}A_{4x} \cos(2\pi f_{42}t + \varphi_{42x}) + 2A_{2y}A_{4y} \cos(2\pi f_{42}t + \varphi_{42y}) \\ & + 2A_{3x}A_{4x} \cos(2\pi f_{43}t + \varphi_{43x}) + 2A_{3y}A_{4y} \cos(2\pi f_{43}t + \varphi_{43y}) \end{aligned}$$

where $f_{ij} = f_i - f_j$, $\varphi_{ijx} = \varphi_{ix} - \varphi_{jx}$ and $\varphi_{ijy} = \varphi_{iy} - \varphi_{jy}$. The intensity at the detection system is the sum of *dc* and *ac* signals. At a particular beat frequency f_{ij} , the field consists of a superposition of both the $\hat{\mathbf{x}}$ and $\hat{\mathbf{y}}$ contributions. If the detection system involves one detector, these two contributions will be superimposed. With two detectors, they can be separated. In the ideal case, the sum of the heterodyne signals arising from f_{21} is null because of the orthogonality conditions of Eqs. 3.8. In the two subsequent sections, we will present the detection systems involving one and two detectors.

3.3 Detection

Although more powerful, the two-detector technique presents practical difficulties. As it will become clear in this section, it indeed requires either seven additional lock-in amplifier (which we don't have) or a serial process in which six lock-in



Figure 3.3: (Color online) Detection systems involving one detector. The signal from the detector is sent to 5 lock-in amplifiers.

amplifiers alternatively demodulate the signals from the two detectors. For practical reasons, only the single detector system has been implemented. However, the contrast between these two methods highlights the capabilities and limitations of the single-detector system.

3.3.1 Optical detection with one detector

Figure 3.3 shows the detection system involving one detector. The optical signal, carrying the four frequency-labeled beams, is sent to a detector. In this detection scheme, the reference SOPs are linear and orthogonal. Their orientation fixes the orientation of the basis $(\hat{\mathbf{x}}, \hat{\mathbf{y}})$. In this frame of reference, the two reference fields of Eq. 3.9 become

$$\mathbf{E}_1 = \begin{pmatrix} A_1 e^{i\varphi_1} \\ 0 \end{pmatrix} e^{2\pi i(\nu+f_1)t}, \quad \mathbf{E}_2 = \begin{pmatrix} 0 \\ A_2 e^{i\varphi_2} \end{pmatrix} e^{2\pi i(\nu+f_2)t}. \quad (3.12)$$

Equation 3.11 simplifies to

$$\begin{aligned} I(t) = & A_1^2 + A_2^2 + A_{3x}^2 + A_{3y}^2 + A_{4x}^2 + A_{4y}^2 \\ & + 2A_1 A_{3x} \cos(2\pi f_{31}t + \varphi_{31}) + 2A_2 A_{3y} \cos(2\pi f_{32}t + \varphi_{32}) \\ & + 2A_1 A_{4x} \cos(2\pi f_{41}t + \varphi_{41}) + 2A_2 A_{4y} \cos(2\pi f_{42}t + \varphi_{42}) \\ & + 2A_{3x} A_{4x} \cos(2\pi f_{43}t + \varphi_{43x}) + 2A_{3y} A_{4y} \cos(2\pi f_{43}t + \varphi_{43y}). \end{aligned} \quad (3.13)$$

where $\varphi_{i1} = \varphi_{ix} - \varphi_1$ and $\varphi_{i2} = \varphi_{ix} - \varphi_2$ ($i = 3, 4$).

In Fig. 3.3, the detector signal is sent to 5 lock-in amplifiers which are electronically locked to the 5 beat frequencies f_{31} , f_{32} , f_{41} , f_{42} and f_{43} . These

Beat frequencies	Lock-in amplitudes	Lock-in phases
f_{31}	$R_{31} = 2A_{3x}A_1$	$\Phi_{31} = (\varphi_{3x} - \varphi_1) + \Psi_{31}$
f_{32}	$R_{32} = 2A_{3y}A_2$	$\Phi_{32} = (\varphi_{3y} - \varphi_2) + \Psi_{32}$
f_{41}	$R_{41} = 2A_{4x}A_1$	$\Phi_{41} = (\varphi_{4x} - \varphi_1) + \Psi_{41}$
f_{42}	$R_{42} = 2A_{4y}A_2$	$\Phi_{42} = (\varphi_{4y} - \varphi_2) + \Psi_{42}$

Table 3.1: Detected amplitudes R_{ij} and phases Φ_{ij} as a function of the optical amplitudes and phases. The phases Ψ_{ij} accounts for the different electronic delays occurring within the generation of the lock-in references.

difference frequencies are either synthesized from the electronic outputs of the AOM frequency generator, or optically by tapping a small portion of the four optical beams and making them interfere. By comparing the detector signal with these electronic references, the lock-in amplifiers extract both the amplitudes R_{ij} and the phases Φ_{ij} of the heterodyne signals at these frequencies.

A summary of the lock-in–demodulated amplitudes and phases is shown in Tab. 3.1. These relations constitute the heart of the single-detector multi-heterodyne detection. The additional phases Ψ_{ij} are added to account for different electronic delays produced during the generation of the lock-in references. This system of equations is under-determined and does not allow retrieval of the SOPs of the object beams at the detection plane, i. e., $(A_{3x}, A_{3y}, \delta_3 = \varphi_{3y} - \varphi_{3x})$ and $(A_{4x}, A_{4y}, \delta_4 = \varphi_{4y} - \varphi_{4x})$.

It may seem discouraging to realize that the single-detector scheme does not allow retrieval of the SOP. However, it already provides advantages as compared to simple heterodyne-based systems. First, in standard heterodyne interferometry, the user should always ensure a sufficient polarization contrast between the reference and the object beams. Usually, a polarization controller is introduced within the reference channel. Reciprocally, if the sample has a strong polarization effect, intensity modulations will appear due to the alteration of the object SOP with respect to the reference SOP. In a multi-heterodyne system, as the basis is orthogonal, the object signal is always integrally measured: if an object beam does not interfere with a particular reference, the heterodyne signal will be maximal with the other reference. This fact justifies the denomination of

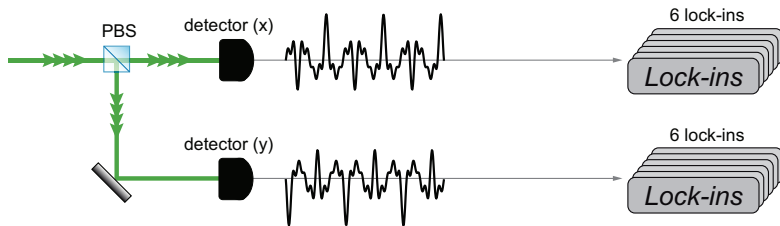


Figure 3.4: (Color online) Detection systems involving two detectors. The signal is separated with a PBS before being sent to the detectors. The detector signals are then each sent to six lock-in amplifiers.

polarization-sensitive for such a system.

The second important and practical advantage as compared to the conventional heterodyne interferometer lies in the *simultaneous* detection of the sample response to two orthogonal SOPs. In a standard heterodyne system, the same capability would imply two successive measurements with a rotation of the object SOP in-between, and thus of the reference SOP too. In many applications, it could perturb the system alignment, which could generate in turn defocusing (for tightly focused beams), loss the spatial coherence (with spatial filters), or more generally changes in experimental conditions. In scanning probe techniques such as SNOM, where the spatial reproducibility could fluctuate, this represents a risk of getting two images whose spatial domains do not overlap. Moreover, damages to the probe would generate measurements which are not comparable.

A third practical advantage occurs when a sample has a particular response to one polarization only. In this case, the second polarization may be used as a comparison field. It could indicate the incidence region in the case of focused illumination (see Chap. 5, 6, 7, 8), serve as a reference for a field enhancement phenomenon (see Chap. 5, 9), or even to selectively excite different modes in waveguides (see Chap. 8).

3.3.2 Optical detection with two detectors

The detection system involving two detectors has already been used in Refs. [35, 36]. A schematic is shown in Fig. 3.4. The optical beam carrying the four het-

erodyne signals is split by a PBS. It is hence the PBS orientation that defines the basis $(\hat{\mathbf{x}}, \hat{\mathbf{y}})$ at the detection plane. The two orthogonally and linearly polarized outputs then reach the X and Y detectors, whose signals are sent to six lock-in amplifiers, locked at each of the six beat frequencies.

For reasons that will be clear later, this detection scheme requires known SOPs for the references, and it is preferable to choose circular left- and right-handed ones. In this case, whatever the orientation of the PBS, the same amount of power will be distributed among the two PBS outputs. Indeed, the incurred risk with linear SOPs is to end up with a low reference power at one detector and therefore to be no longer shot noise limited.

In the same way as in the last section, the intensity of Eq. 3.11 leads to lock-in amplitudes R_{ijx} , R_{ijy} and phases Φ_{ijx} , Φ_{ijy} summarized in Tab. 3.2. At a specific heterodyne frequency f_{ij} , the electronic phases $\Psi_{ijx,y}$ are the same for both the X and Y lock-in amplifiers because they share the same source. We note that even if the optical phase differences from the PBS to the detectors are different, the phase accumulated by φ_{ix} and φ_{jx} (resp. φ_{iy} and φ_{jy}) cancel after subtraction.

The amplitudes of the object fields at the detector may be retrieved using the following relations:

$$\begin{aligned} A_{3x} &= \sqrt{\frac{R_{31x} \cdot R_{32x}}{2R_{21x}}} & \text{and} & & A_{3y} &= \sqrt{\frac{R_{31y} \cdot R_{32y}}{2R_{21y}}}, \\ A_{4x} &= \sqrt{\frac{R_{41x} \cdot R_{42x}}{2R_{21x}}} & \text{and} & & A_{4y} &= \sqrt{\frac{R_{41y} \cdot R_{42y}}{2R_{21y}}}. \end{aligned} \quad (3.14)$$

The relative phases are retrieved by subtracting from the Y phases their respective X values. We end up with the following system of equations:

$$\begin{aligned} \delta_3 &= (\varphi_{3y} - \varphi_{3x}) = (\Phi_{31y} - \Phi_{31x}) + (\varphi_{1y} - \varphi_{1x}) \\ \delta_3 &= (\varphi_{3y} - \varphi_{3x}) = (\Phi_{32y} - \Phi_{32x}) + (\varphi_{2y} - \varphi_{2x}) \\ \delta_4 &= (\varphi_{4y} - \varphi_{4x}) = (\Phi_{41y} - \Phi_{41x}) + (\varphi_{1y} - \varphi_{1x}) \\ \delta_4 &= (\varphi_{4y} - \varphi_{4x}) = (\Phi_{42y} - \Phi_{42x}) + (\varphi_{2y} - \varphi_{2x}). \end{aligned} \quad (3.15)$$

This system of equations holds for any reference SOPs. However, it cannot be solved unless the reference SOPs are known, i.e., $\delta_1 = \varphi_{1y} - \varphi_{1x}$ and $\delta_2 = \varphi_{2y} - \varphi_{2x}$ are known.

Beat frequencies	Lock-in amplitudes X	Lock-in phases X
f_{21}	$R_{21x} = 2A_{2x}A_{1x}$	$\Phi_{21x} = (\varphi_{2x} - \varphi_{1x}) + \Psi_{21}$
f_{31}	$R_{31x} = 2A_{3x}A_{1x}$	$\Phi_{31x} = (\varphi_{3x} - \varphi_{1x}) + \Psi_{31}$
f_{32}	$R_{32x} = 2A_{3x}A_{2x}$	$\Phi_{32x} = (\varphi_{3x} - \varphi_{2x}) + \Psi_{32}$
f_{41}	$R_{41x} = 2A_{4x}A_{1x}$	$\Phi_{41x} = (\varphi_{4x} - \varphi_{1x}) + \Psi_{41}$
f_{42}	$R_{42x} = 2A_{4x}A_{2x}$	$\Phi_{42x} = (\varphi_{4x} - \varphi_{2x}) + \Psi_{42}$
f_{43}	$R_{43x} = 2A_{4x}A_{3x}$	$\Phi_{43x} = (\varphi_{4x} - \varphi_{3x}) + \Psi_{43}$

Beat frequencies	Lock-in amplitudes Y	Lock-in phases Y
f_{21}	$R_{21y} = 2A_{2y}A_{1y}$	$\Phi_{21y} = (\varphi_{2y} - \varphi_{1y}) + \Psi_{21}$
f_{31}	$R_{31y} = 2A_{3y}A_{1y}$	$\Phi_{31y} = (\varphi_{3y} - \varphi_{1y}) + \Psi_{31}$
f_{32}	$R_{32y} = 2A_{3y}A_{2y}$	$\Phi_{32y} = (\varphi_{3y} - \varphi_{2y}) + \Psi_{32}$
f_{41}	$R_{41y} = 2A_{4y}A_{1y}$	$\Phi_{41y} = (\varphi_{4y} - \varphi_{1y}) + \Psi_{41}$
f_{42}	$R_{42y} = 2A_{4y}A_{2y}$	$\Phi_{42y} = (\varphi_{4y} - \varphi_{2y}) + \Psi_{42}$
f_{43}	$R_{43y} = 2A_{4y}A_{3y}$	$\Phi_{43y} = (\varphi_{4y} - \varphi_{3y}) + \Psi_{43}$

Table 3.2: Detected amplitudes and phases R_{ijx} , Φ_{ijx} , and R_{ijy} , Φ_{ijy} , on the X and Y detectors, respectively, as a function of the optical amplitudes and phases. The phases Ψ_{ij} arise from the generation of the electronic references of the lock-in amplifiers.

3.4 Signal to noise ratio, amplitude and phase accuracy

In the case of circular right- and left-handed SOPs, $\delta_1 = \varphi_{1y} - \varphi_{1x} = -\pi/2$ and $\delta_2 = \varphi_{2y} - \varphi_{2x} = \pi/2$ (or vice versa), and Eqs. 3.15 become

$$\begin{aligned}
 \delta_3 &= (\varphi_{3y} - \varphi_{3x}) = (\Phi_{31y} - \Phi_{31x}) - \pi/2 \\
 \delta_3 &= (\varphi_{3y} - \varphi_{3x}) = (\Phi_{32y} - \Phi_{32x}) + \pi/2 \\
 \delta_4 &= (\varphi_{4y} - \varphi_{4x}) = (\Phi_{41y} - \Phi_{41x}) - \pi/2 \\
 \delta_4 &= (\varphi_{4y} - \varphi_{4x}) = (\Phi_{42y} - \Phi_{42x}) + \pi/2.
 \end{aligned} \tag{3.16}$$

The plus and minus signs preceding the factor $\pi/2$ must be inverted in the case where $\delta_1 = \varphi_{1y} - \varphi_{1x} = \pi/2$ and $\delta_2 = \varphi_{2y} - \varphi_{2x} = -\pi/2$.

Compared to the single-detector solution, the heterodyne signals produced by the two references do not disappear. In terms of lock-in amplitudes and phases, the orthogonality conditions of Eqs. 3.8 become

$$R_{21x} = R_{21y} \quad \text{and} \quad \Phi_{21x} - \Phi_{21y} = n\pi, \quad n \text{ odd.} \tag{3.17}$$

These equations offer a straightforward way to check the orthogonality of the reference beams directly from the heterodyne signals.

With Eqs. 3.14 and 3.16, the SOPs of the object fields at the detection plane are measured, i.e., $A_{3x}, A_{3y}, \delta_3 = \varphi_{3y} - \varphi_{3x}$ and $A_{4x}, A_{4y}, \delta_4 = \varphi_{4y} - \varphi_{4x}$. The two-detector system thus provides an elegant way to provide the SOPs of the two object fields at the detection plane by using the heterodyne amplitudes and phases in a one-step process.

3.4 Signal to noise ratio, amplitude and phase accuracy

Expressions of the signal to noise ratio (SNR) as well as the amplitude and phase accuracy will be derived for the single-detector system only. The frequency labeling of the four beams allows us to consider the multi-heterodyne interferometer as six heterodyne interferometers with beat frequencies $f_{21}, f_{31}, f_{41}, f_{32}, f_{42}$ and f_{43} . The considerations concerning the SNR and the amplitude and phase accuracy developed in Chap. 2 are applied to each of the six interferometers independently.

In standard heterodyne interferometry, the reference and object SOPs are usually aligned in order to maximize the interference contrast, and the scalar-based description of Chap. 2 leads to the expressions of the SNR (Eq. 2.15) and

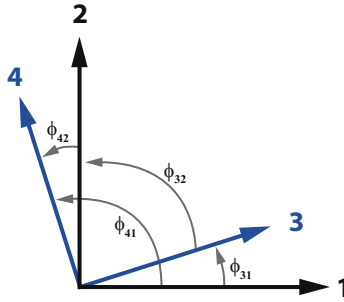


Figure 3.5: (Color online) Representation of the SOP at the detector plane in the particular case where the object channels 3 and 4 remain orthogonal and linear. In the single-detector technique, the references 1 and 2 are orthogonal and linearly polarized.

the amplitude and phase accuracy (Eqs. 2.19 and 2.20). In contrast, the object SOPs may have arbitrary orientations with respect to the reference SOPs within the multi-heterodyne system and a vectorial approach is required.

Applying Eq. 2.12 to the heterodyne signal produced by channels i and j , one obtains the corresponding electrical power

$$P_{AC}^{ij} = 2m^2 S^2 R_0 \cdot [A_{ix}^2 A_{jx}^2 + A_{iy}^2 A_{jy}^2 + 2A_{ix} A_{iy} A_{jx} A_{jy} \cos [(\varphi_{ix} - \varphi_{jx}) - (\varphi_{iy} - \varphi_{jy})]] . \quad (3.18)$$

If the SOPs of i and j are orthogonal, Eqs. 3.8 holds and P_{AC}^{ij} becomes zero. Compared to standard heterodyne interferometry, the presence of the relative phase differences in the cosine function degrades the power of the heterodyne signal, and thus the SNR. Although this equation represents the most general case, it however cannot be used within the single-detector framework because the individual parameters are not *a priori* available.

Let us assume that the SOPs of the object channels are linear at the detector, and that their orthogonality is preserved. This situation is depicted in Fig. 3.5. Because the SOPs of the references are linear, Eqs. 3.18 becomes

$$P_{AC}^{ij} = 2m^2 S^2 R_0 P_i P_j \cos(\phi_{ij})^2, \quad (3.19)$$

where P_i and P_j are the powers of the individual channels i and j . The angle ϕ_{ij} accounts for the relative orientation of the SOPs. As can be seen in Fig. 3.5, these angles are not independent:

$$\phi_{31} = \frac{\pi}{2} - \phi_{32}, \quad \phi_{41} = \frac{\pi}{2} - \phi_{42}, \quad \phi_{31} = \phi_{42}, \quad \phi_{32} = \phi_{41} - 2\phi_{31}. \quad (3.20)$$

Since the shot noise level ultimately depends on the total power reaching the detector, the SNR of Eq. 2.15 becomes, for shot noise limited detection,

$$\text{SNR}_{ij} = \frac{m^2 \eta}{h\nu B} \frac{P_i P_j \cos(\phi_{ij})^2}{P_{tot}}, \quad (3.21)$$

where $P_{tot} = P_1 + P_2 + P_3 + P_4$ is the total power provided by the individual contribution of each of the four channels. If i and j are respectively a reference and an object channel and if $P_i \gg P_j$ ($m=1$), the last equation becomes

$$\text{SNR}_{ij} = \frac{\eta}{h\nu B} P_j \cos(\phi_{ij})^2, \quad (3.22)$$

which is the equivalent of Eq. 2.16.

Eq. 2.14 assessing the minimum reference power P_r^{min} required for shot noise limited detection still holds, but should be independently applied to both references.

Finally, Eqs. 2.19 and 2.20 have to be applied to each SNR_{ij} to evaluate the amplitude and phase resolutions

$$\frac{\delta A_{ij}}{A_{ij}} = \frac{1}{\sqrt{\text{SNR}_{ij}}}, \quad \delta \varphi_{ij} = \frac{1}{\sqrt{\text{SNR}_{ij}}}. \quad (3.23)$$

At the end of Chap. 2, a short example was presented with the aim of showing the order of magnitude of the quantities involved in a typical detection scenario. In the same circumstances, $P_j = 1 \text{ pW}$ ($j = 3, 4$), $B = 25 \text{ Hz}$, $\eta = 85 \%$ and $\lambda = 1520 \text{ nm}$, and for shot noise-limited detection Eqs. 3.22 and 3.23 lead to the following values at different ϕ_{ij} :

ϕ_{ij} [deg]	SNR [dB]	$\delta A/A$	$\delta \varphi$ [deg]	$2\pi/N$
0	54.1	$1.97 \cdot 10^{-3}$	0.11	3204
45	51.1	$2.8 \cdot 10^{-3}$	0.16	2265
60	48.1	$3.9 \cdot 10^{-3}$	0.22	1602
80	38.9	$11 \cdot 10^{-3}$	0.65	556
90	-	-	-	-

Even for relatively high values of ϕ_{ij} , the SNR stays above 30 dB and the phase resolution is smaller than 1 deg ($\sim 2\pi/500$). As long as the use of the two heterodyne signals arising from the same object beam is not required (such as in Chap. 8), one can always choose the stronger signal with the best accuracy.

3.5 Conclusion

The expression of the field at the detection plane has been derived for a multi-heterodyne interferometer, both for the single- and the two-detector detection system. The single-detector scheme leads to polarization-sensitive measurements in the sense that it provides the response of the sample illuminated by two orthogonally polarized illuminating beams. In comparison, the two-detector method allows the retrieval of the SOP of the field at the sample surface, provided that the transfer function of the system from the sample plane to the detection can be measured. Finally, we have derived the expressions for the SNR and the amplitude and phase accuracy in the single-detector system. The major difference with the standard heterodyne technique is the fact that within the multi-heterodyne interferometer, the object SOPs have an arbitrary orientation with respect to the references, leading to an alteration of the SNR, and thus of the amplitude and phase accuracy. However, even in “extreme” conditions (angle of 80 deg between object and reference), a resolution smaller than 1 deg is expected.

This chapter has set the theoretical framework on which the multi-heterodyne scanning near-field optical microscope presented in the next chapter is based. The introduction of a scanning probe system in the object arm will lead to a near-field microscope suitable for polarization-sensitive measurements.

4

Multi-Heterodyne Scanning Near-field Optical Microscope (MH-SNOM)

Since the introduction of pseudo-heterodyne [37] and heterodyne [38] techniques in near-field microscopy, intense efforts have been made to bring interferometric techniques for phase measurement to a mature level. Currently, phase measurements involving the heterodyne technique [7, 8, 17, 39] or other interferometric methods [10, 40, 41] are routinely used. However, measuring the near-field polarization is more delicate and relatively less work has been performed to date [36, 42–45].

In this chapter, we describe the Multi-Heterodyne Scanning Near-Field Optical Microscope (MH-SNOM). The principle of multi-heterodyne detection for polarization measurements has been introduced in chapter 3. The main concept of the MH-SNOM is to combine the multi-heterodyne interferometer with

a scanning near-field optical microscope (SNOM). The goal is to measure the amplitude, the phase and the polarization in the near field, or in the far field. The system has the additional ability of being tunable over the wavelength range of 1460 – 1580 nm. The entire development of this instrument has been realized within the framework of this thesis and represents a significant investment of time and effort.

We will begin with a detailed description of the building blocks of the system. Then we will derive the fundamental expressions for the measured fields. The signal to noise ratios as well as the amplitude and phase accuracies will be assessed through a representative experiment. Finally, we will discuss issues that may arise while tuning the laser wavelength and assess the phase drifts occurring within the interferometer.

4.1 Set-up

In this section, we present the set-up constituting the MH-SNOM. Figure 4.1 shows a schematic view of the system. We conceptually distinguish five building blocks.

The optical interferometer is an implementation for near-field microscopy of the multi-heterodyne interferometer presented in Chap. 3. It is designed to work in the wavelength range of $\lambda = 1460 - 1580$ nm. All optical paths apart from the sample itself are fibered.

The detection system involves the detector, an electronic splitter that cleanly distributes the detector signal among the several post-processing lock-in amplifiers, and the lock-in amplifiers themselves.

The data acquisition section shows how the many signals provided by the lock-in amplifiers are acquired, and how this acquisition is synchronized with the motion of the probe. In particular, we present a description of the software developed for this purpose.

The probe motion is performed with a three-axis piezo stage. Due to the large number of optical signals to be measured, the probe motion is driven by two

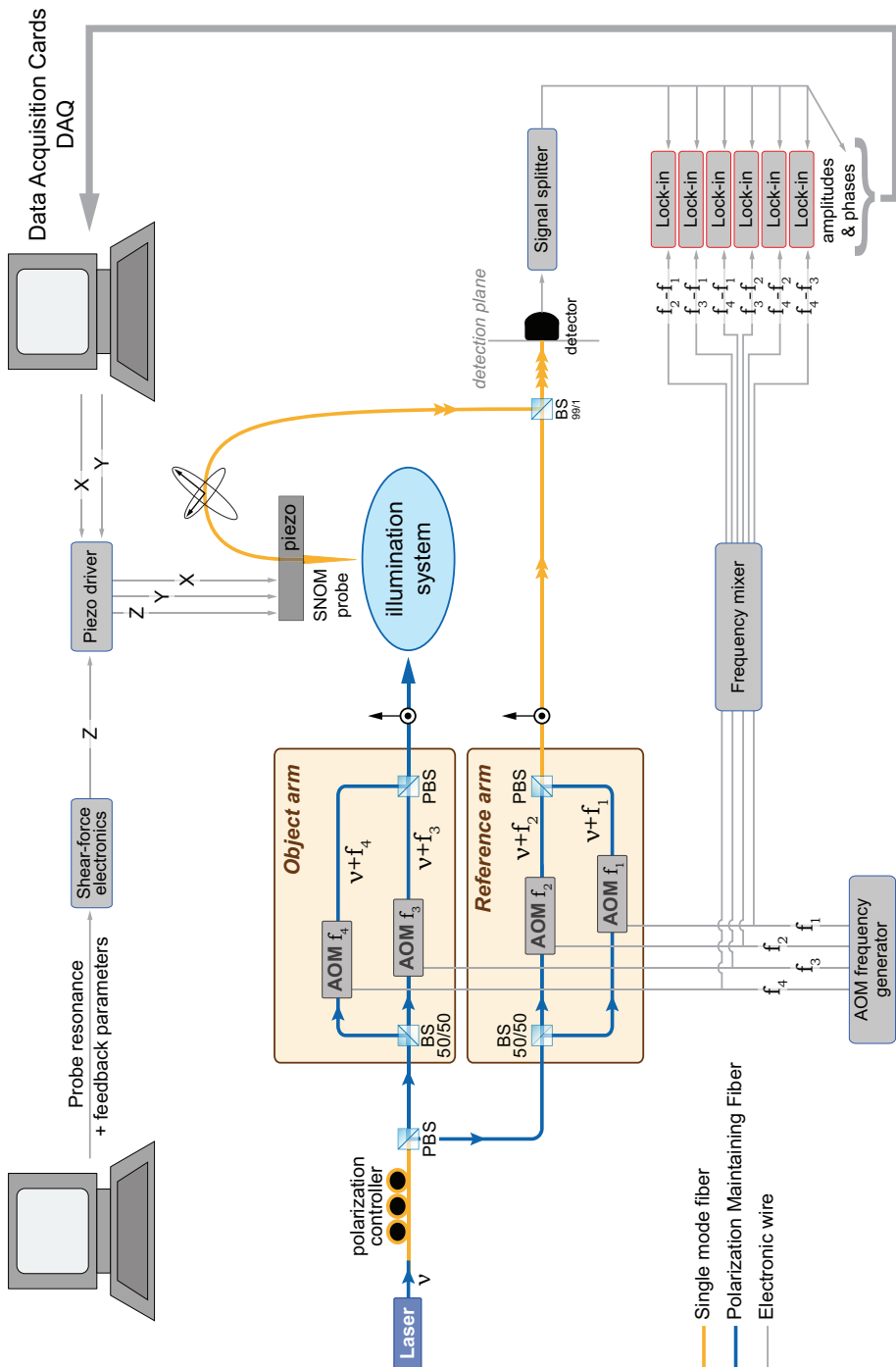


Figure 4.1: (Color online) Overview of the Multi-Heterodyne Scanning Near-Field Optical Microscope (MH-SNOM).

computers. One computer manages the vertical motion of the probe, and the other the horizontal motion synchronized with the data acquisition.

The SNOM head is a purpose-built mechanical construction housing the piezo stage. Its specificities rely on its large dimensions and its ability to accommodate cumbersome and/or heavy experimental configurations.

4.1.1 Optical interferometer

In this section, we describe the optical multi-heterodyne interferometer shown in Fig. 4.1. This set-up is all-fibered. The yellow and blue paths correspond to Single Mode Fibers (SMF) and panda-type Polarization Maintaining Fibers (PMF) respectively. PMFs can be twisted to rotate the polarization of the beams in any arm whenever needed. Back reflections at all connecting points are considerably reduced with FC/APC connectors. The entire optical system lies on a vibration isolated table with passive pneumatic legs, and is enclosed in plexiglas boxes to protect it from air currents. Finally, except for the SNOM head, all optics are isolated with 6 cm thick polyurethane foam pads. This protection slows down thermal energy transfer and considerably attenuates acoustic vibrations.

The tunable laser source is an external cavity diode laser (*Agilent, Model 81682A*). Wavelengths ranging from 1460 nm to 1580 nm can be produced with an accuracy of 10 pm. The laser is mode-hop free over the full wavelength range. The output power can be stabilized at a given value. However, its range depends on the wavelength. Typical output powers are greater than: 1 mW over 1460 – 1580 nm, 2.8 mW over 1480 – 1580 nm, and 5.6 mW over 1520 – 1580 nm. The laser coherence length being about 640 m (in the fiber medium), the effects of limited temporal coherence due to the Optical Path Differences (OPDs) can be reasonably neglected. Finally, the laser output is linearly polarized within a PMF.

The laser light of frequency ν passes through a 3-paddle polarization controller before reaching a Polarizing Beam Splitter (PBS, *OZ Optics*). Doing so allows for control of the power ratio between the object and reference arms by acting on the polarization orientation of the input beam. The two outputs of the PBS constitute the starting point of the object and reference arms. Each of the two

	$\nu + f_2$	$\nu + f_3$	$\nu + f_4$
$\nu + f_1$	20 kHz	50 kHz	90 kHz
$\nu + f_2$		30 kHz	70 kHz
$\nu + f_3$			40 kHz

Table 4.1: Possible combinations of the electronic beat-signals generated in the photodetector by the superposition of the four optical beams at frequencies $\nu + f_1$, $\nu + f_2$, $\nu + f_3$ and $\nu + f_4$.

arms are then equivalently split in two subsequent channels with a 50/50 Beam Splitter (BS, *OZ Optics*).

The four resulting beams pass through AOMs (*IntraAction*, Model *FCM-401E5C*) driven with a quad source frequency generator (*IntraAction*, Model *DFE-401C-18*). All the frequencies are internally phase-locked with the same crystal oscillator. The four AOMs are independently driven at frequencies f_1 , f_2 , f_3 and f_4 , and the four resulting optical frequencies are: $\nu + f_1$, $\nu + f_2$, $\nu + f_3$ and $\nu + f_4$. A discussion on how to fix these frequencies is provided later in Sec. 4.3.1 addressing the difficulties that may occur while changing the laser wavelength. However whatever f_1 is, the three remaining frequencies f_2 , f_3 and f_4 will always be set such that $f_2 = f_1 + 20$ kHz, $f_3 = f_1 + 50$ kHz and $f_4 = f_1 + 90$ kHz. It follows that the beat frequencies $f_i - f_j$ are constant. They are summarized in Tab. 4.1.

These frequencies are chosen to avoid harmonic cross-talk between signals. This is however not true for the 40 kHz signal which represents the first harmonic of the 20 kHz signal. However, as will be mentioned in Sec. 4.2.1, this signal will be disregarded because of its extremely small intensity.

The two reference channels are recombined with a PBS (*OZ Optics*) into a SMF. Their states of polarization (SOPs) are hence linear and orthogonal. In contrast, the object channels are superimposed with a PBS (*OZ Optics*) into a PMF, leading also to linear and orthogonal SOPs. As will be demonstrated in Sec. 4.3.3, the linearity and the orthogonality of the references is well preserved up to the detector. The object beams also reach the illumination system with well linear and orthogonal SOPs. By rotating the output element (connector)

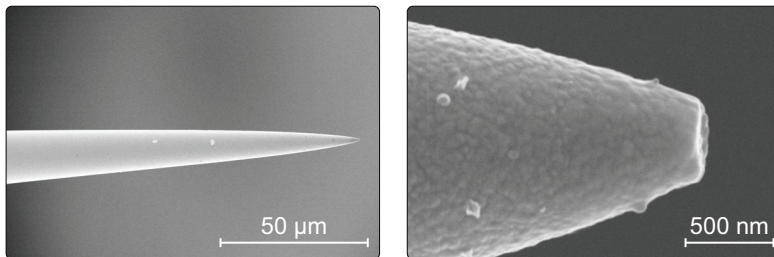


Figure 4.2: (Color online) Scanning Electron Microscope (SEM) images of the coated SNOM probes used in our experiments.

of the object arm, one can set the desired SOPs for a specific experiment, such as TE and TM, for example. We emphasize that the use of single-mode fibers naturally performs the spatial filtering of the light before illuminating the sample. The object arm then enters the illumination system whose configuration depends on the experiment: injection into waveguide structures, transmission through (semi-)transparent elements, frustrated total internal reflection, etc.

The field at the sample surface is finally collected (collection mode) by the SNOM probe (*Lovalite, Model E50-SMF28-AL70-200*). This commercial probe is coated with a 70 nm thick aluminum layer in order to reduce the coupling zone and to reflect spurious scattered light. In the coating process, a 200 nm wide aperture is left opened through the shadowing technique [46]. Scanning electron microscope (SEM) images of the probe acquired at different magnifications are shown in Fig. 4.2. These are the only type of probe used in this work. The light collected by the probe is finally mixed with the reference signals using an asymmetric coupler (*General Photonics*). Since the signal collected by the SNOM probe is very weak, 99% of it is coupled with 1% of the reference signals. The superposition of the four optical signals then reaches the detector.

4.1.2 Detection system

The detection system of the MH-SNOM (Fig. 4.1) includes the detector, the electronic splitter and the lock-in amplifiers.

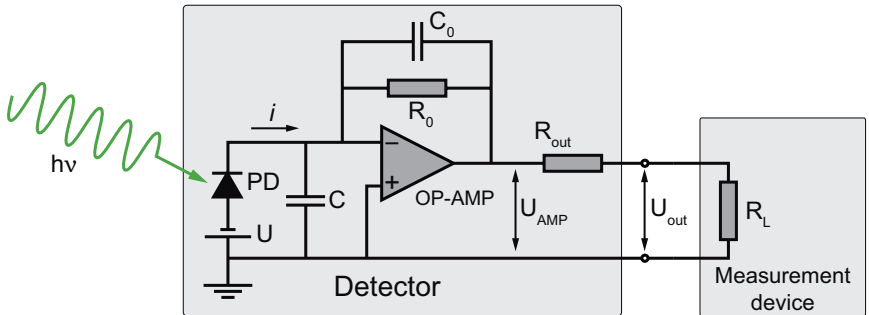


Figure 4.3: (Color online) Detector circuit consisting of an *InGaAs* photodiode (PD) followed by a transimpedance amplifier. The right block represent the measurement device (e.g. a lock-in amplifier, spectrum analyzer, or data acquisition card).

Figure 4.3 shows the electronic circuit of the detector (*Laboptic, Model DG100*). It consists of an *InGaAs* photodiode (*Fermionics, Model FD100-FC*) followed by a transimpedance amplifier circuit, using a high-speed and low current noise operational amplifier (OP-AMP). The photodiode is supplied with a bias voltage $U = -5$ V. The OP-AMP and photodiode capacitances are schematically represented by an overall capacitance C of about 2 pF. A feedback capacitor C_0 is added to optimize phase compensation of the OP-AMP and to ensure stability. Both C and C_0 should be small to limit the detector noise, and to provide a large bandwidth for the detection. The resistor $R_{out} = 50 \Omega$ adapts the output impedance with the 50Ω impedance of both the coaxial cable and the splitter. When the load R_L representing the input impedance of the measuring device (e.g. a lock-in amplifier, spectrum analyzer, or data acquisition card) is large compared to R_{out} , the voltage U_{AMP} is equal to the voltage at the output of the detector.

Eq. 2.5 relates the current i generated by the photodiode with the optical power P_{opt}

$$i = SP_{opt}, \quad (4.1)$$

where S is the spectral response of the photodiode. The manufacturer specifications show S to be 1.04 A/W at $\lambda = 1550$ nm and decreases no more than 5 %

over the wavelength range of the laser. As P_{opt} is small, the current must be amplified. The OP-AMP also controls the voltage at the photodiode boundary and regulates the current through the feedback resistor $R_0 = 1\text{ M}\Omega$. Since the contribution of the OP-AMP noise is smaller than that of the feedback resistor, it can be neglected.

The frequency response of the detector has been measured with a laser diode modulated at frequencies ranging between 10 Hz and 10^7 Hz, and acquired with a spectrum analyzer (*Hewlet Packard, Model 4195A*). The measurement results are shown in Fig. 4.4 (a). The detector pass-band (at -3 dB) is 7.5 MHz. As the heterodyne beat frequencies are smaller than 100 kHz, which is well below the cut-off frequency, the response of the detector may be considered as linear. The output voltage is therefore

$$U_{out} = SR_0P_{opt}. \quad (4.2)$$

The spectral sensitivity being close to 1, this equation shows that R_0 appears as a scaling factor between the detected voltage and the optical power irradiating the photodiode: a voltage of 1 V corresponds to $1\ \mu\text{W}$.

The thermal noise has been measured with a spectrum analyzer (*Stanford Research, Model SR770*) whose input impedance is $R_L = 1\text{ M}\Omega$ and operates between 0 and 100 kHz. The analyzer provides a spectrum U_V in volts. The corresponding power dissipated in the measurement device is

$$P = \frac{U_V^2}{R_L}. \quad (4.3)$$

The spectrum is shown by the blue curve in Fig. 4.4 (b) whose mean value is approximately $P_{TN}=8.21\cdot 10^{-18}$ W.

Accounting for R_0 and R_{out} , the corresponding theoretical thermal noise is retrieved from Eq. 2.4

$$P_{TN} = 4kTB \frac{R_L R_0}{(R_L + R_{out})^2}. \quad (4.4)$$

Since $R_L \gg R_{out}$, this becomes

$$P_{TN} = 4kTB \frac{R_0}{R_L}. \quad (4.5)$$

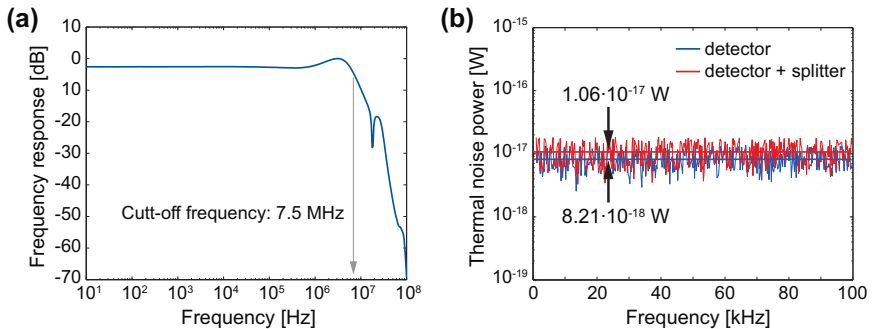


Figure 4.4: (Color online) (a) Measured detector frequency response. The detector pass-band (-3 dB) is 7.5 MHz. (b) Measured electronic noise of the detector (blue), and of the detector plus splitter system (red). The measurements are performed in the dark (analyzer bandwidth $B=250$ Hz).

With $B = 500$ Hz, $R_L = 1$ M Ω and $T = 300$ K, the calculated electric power corresponding to the thermal noise of the photodetector is $P_{TN} = 8.28 \cdot 10^{-18}$ W, which corresponds well to the measured value.

The purpose-built splitter (Fig. 4.1) separates the signal arising from the detector into 12 equivalent outputs that can be sent to the various measuring devices (lock-in amplifiers, data acquisition cards, spectrum analyzer, etc.). Its input impedance is 50 Ω . The splitter is introduced to avoid a serial connection between the detector and the several measurement devices. A serial scheme would indeed involve several BNC T-adapters and a long cable length that could introduce back reflections and noise due to antenna phenomena. In a similar fashion as for the detector, the electric thermal noise of the system composed of the detector *and* the splitter has been measured. It corresponds to the red curve in Fig. 4.4 (b). The mean value is about $1.06 \cdot 10^{-17}$ W: the splitter adds no more than $2 \cdot 10^{-18}$ W to the detector thermal noise. The power spectral density of the thermal noise corresponding to the photodetector followed by the splitter is therefore

$$\sqrt{\frac{\langle U_N^2 \rangle}{B}} = \sqrt{\frac{R_L P_{TN}}{B}} = 146 \text{ nV}/\sqrt{\text{Hz}}. \quad (4.6)$$

Finally, the heterodyne signals are demodulated with six lock-in amplifiers.

The technical datasheets of the two kinds of lock-in amplifiers involved in the system (*Stanford Research, Models SR530 and SR830*) ensure that the electrical noise does not exceed $7 \text{ nV}/\sqrt{\text{Hz}}$, which is well below the detector contribution. Thus, the noise introduced by the lock-in amplifiers can be neglected. The six lock-in amplifiers provide a total of 12 optical signals (6 amplitudes and 6 phases) that must be acquired simultaneously for each pixel of a SNOM scan.

4.1.3 Data acquisition

A relevant task in the setting up of the MH-SNOM has been to find a way to simultaneously acquire the significant number of signals provided by the lock-in amplifiers and other devices (piezo sensors, SNOM electronics, etc.). We indeed didn't find a commercial system corresponding to our needs. Our strategy has been to use an already existing commercial SNOM system for the Z motion of the probe (shear-force feedback), and to develop an independent control system for the in-plane X and Y motion, and data acquisition. The motion of the probe will be analyzed in the next section.

The overall configuration is presented in Fig. 4.5. The system controlling the X and Y motion of the probe, as well as the data acquisition, is driven by computer 1 on the left hand-side. Two 16-bit Data Acquisition Cards (DAQs) (*National Instruments, Model NI PCI-6251*) offer a total of 32 analog inputs (AIs) and 4 analog outputs (AOs). Two of the AOs, AO1 and AO2, are permanently attributed to the X and Y control. The third and fourth analog outputs AO3 and AO4 may be attributed to the scanning modes M2 and M3 as described below.

The AIs have a worst-case accuracy of 2 mV^1 . The maximum sampling frequency is 1.25 Ms/s (mega samples per second) shared between the 16 channels of each card. Indeed, the inner structure of the cards consists of a multiplexer that connects the channels one after the other to a single Analog to Digital Converter (ADC). The elapsed time for a 16 channel reading is therefore $13 \mu\text{s}$. It is

¹With a 16-bit analog to digital converter and working on a range of 20 V (-10 to $+10 \text{ V}$), the resolution is $20/2^{16} \simeq 300 \mu\text{V}$. However, due to other internal phenomena (drifts, noise, etc.), the resolution is limited and leads to an effective accuracy of 2 mV . This resolution represents the worst-case scenario. According to *National Instruments* specialists, the true resolution lies in between.

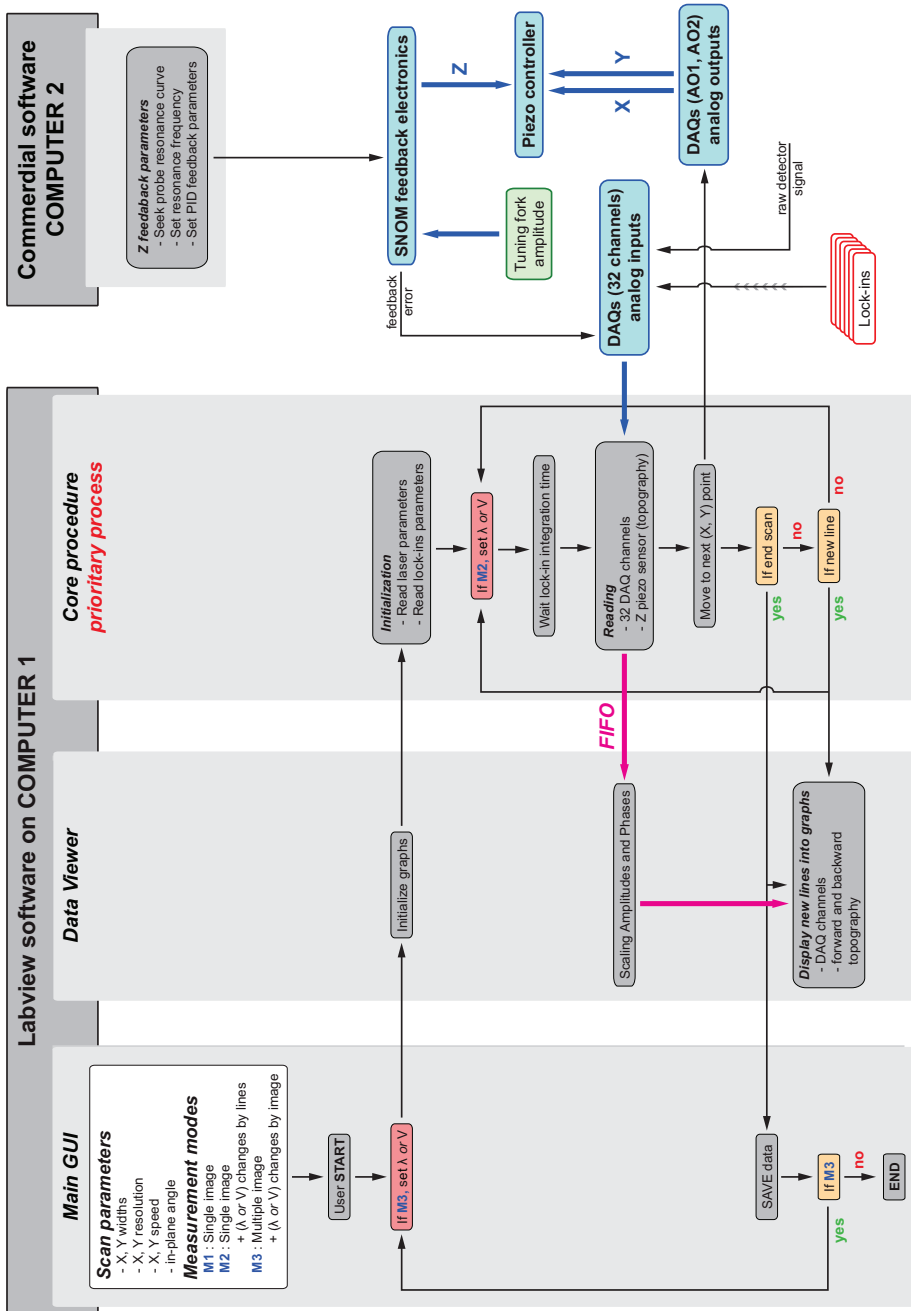


Figure 4.5: (Color online) Flow chart of the piezo control and data acquisition process. The set-up involves two computers: one dedicated to the in-plane X and Y piezo motion as well as the data acquisition, the other using a commercial system controlling the shear-force feedback (Z motion).

therefore reasonable to speak of *simultaneous detection* while observing stationary phenomena.

The X and Y motion as well as the synchronized data acquisition is performed via purpose-built software. The software has been developed in Labview (*National Instruments*). It is indeed a high level language that offers flexibility for adapting the program to the purposes of a specific experiment. The compatibility with the DAQs also makes the data collection easier. The flow chart showing the general working principle of the software is shown in Fig. 4.5. The program consists of three procedures working in parallel: the main GUI (Graphical User Interface), the data viewer and the core procedure.

The main GUI is the main window with which the user interacts. The scan parameters such as the X and Y widths, the X and Y resolutions (pixels), the X and Y speeds, the in-plane scanning angle, etc. are set in the main GUI. The user may also choose between three kind of scanning modes that will be frequently used in this work. The mode M1 corresponds to the traditional X-Y scan. The mode M2 allows for a change in the laser wavelength λ or the voltage V at AO3 (or AO4) after each line. By setting one scanning width to zero (either X or Y), the MH-SNOM can raster scan the same line but changes λ or V in between. In M3, the probe acquires several images at different λ or V .

When the user starts a new measurement, the data viewer form is initialized and displayed within the main GUI. The data viewer consists of a series of graphs that display the data provided by the core procedure. The AIs which correspond to lock-in amplitudes are scaled according to the lock-in amplifier sensitivities. It allows a quantitative comparison between heterodyne signal amplitudes. Phases are also scaled between -180 deg and $+180$ deg. The data arrive within this procedure through a FIFO (First In First Out) queue. Data are displayed line-by-line.

The core procedure is a state machine that has priority among the other procedures, i.e., it first runs and if the computer has extra resources, the main GUI and the data viewer execute their tasks. After an initialization state where the lock-in amplifier and laser parameters are read through the GPIB interface, the core procedure moves the probe and collects the data. At each point (pixel), the probe dwells for a certain time before the acquisition is performed. Lock-

in amplifiers indeed have filters characterized by a Time Constant (TC) that requires a certain wait time in order to pass their transitory regime. According to the lock-in specifications, it is necessary to wait five times the TC to reach 99% of the “true” value. Typically, most of the scans are run with a TC of 3 ms, which implies a 15 ms wait time before the lock-in acquisition. So after this wait time, the core procedure acquires the DAQ channels: lock-in signals, raw data from the detector, topography from the Z piezo sensor, shear-force feedback error signal from the SNOM electronics, or additionally required information.

Then the core procedure moves to the next X-Y point by sending voltage ramps to the piezo X and Y channels through AO1 and AO2. These ramps generate a smooth motion of the probe while accounting for speed in the X and Y direction. At the end of each line, the core procedure orders the viewer procedure to display the new line data. At the end of the scan, all the data are automatically saved.

4.1.4 Probe motion

The element that provides the three-dimensional motion of the probe is the XYZ piezo stage (*Physik Instrumente, Model P-517.3CL*). Its travel ranges are $L_x = L_y = 100 \mu\text{m}$ and $L_z = 20 \mu\text{m}$ with a repeatability of $\pm 5 \text{ nm}$ and $\pm 1 \text{ nm}$ in the X-Y and Z directions, respectively. The stage is supplied with an amplifier module (*Physik Instrumente, Model E-503*) that converts the three independent X, Y, Z command voltages (-2 to $+12 \text{ V}$) into driving voltages (-20 to $+120 \text{ V}$). Three independent channel sensors (*Physik Instrumente, E-509.C3A*) allow closed-loop operation, i.e., the X, Y, Z command voltages are interpreted as absolute positions ($1 \text{ V} = 10 \mu\text{m}$ for the X, Y actuators, and $1 \text{ V} = 2 \mu\text{m}$ for the Z actuator). With respect to Fig. 4.5, the X, Y piezo tubes are driven by the DAQs analog outputs AO1 and AO2 of computer 1 whereas the Z axis depends on the commercial electronics driven by computer 2.

AO1 and AO2 have an accuracy of 2 mV. The same remark as for the AIs holds (see previous section): this accuracy represents the worst-case manufacturer estimation. According to the amplification factors of the piezo system, this accuracy leads to an accuracy of 20 nm for the X and Y motion. However, from

our experience, topography measurements always showed a much better accuracy.

The commercial system that drives the Z motion of the probe (*APE Research*) finds the resonance frequency of the sensor (tuning fork + probe). A pre-amplifier provides the electrical amplitude of the tuning fork oscillations. A fraction of the resonance amplitude (typically 90 %) constitutes the set-point for the closed-loop PID (Proportional Integral Derivative) feedback.

As the tip approaches the surface, the resonance amplitude drops due to the interaction with inter-atomic forces. The interaction range is 1 to 100 nm, depending on the type of probe and the particular implementation [46]. The system will therefore act on the piezo Z axis in order to maintain the tuning fork oscillation at the set-point. The PID parameters are set individually and according the quality factor of the sensor resonance. Most of the time, only the integral parameter is necessary. The commercial system also drives the DC X, Y, and Z motors as shown in Fig. 4.1 and Fig. 4.6 (a) (see next section).

4.1.5 SNOM head

The piezo stage is the key element for the nanometric motion of the probe. However, due to its limited travel range in the vertical direction ($L_z = 20 \mu\text{m}$), additional mechanisms are required for the coarse approach of the probe to the sample surface. Furthermore, many experimental configurations involve cumbersome and heavy apparatus. These considerations led us to manufacture a custom-designed SNOM head housing the piezo stage.

A 45° side view of the SNOM head is shown in Figs. 4.6 (a) and (d). The SNOM sensor (probe + tuning fork) is fixed on a yellow circuit board (PCB) connected to the shear-force pre-amplifier. The PCB is screwed on a manual translation stage, itself attached to piezo stage (in blue on the picture). The piezo stage is fixed on the motorized stage allowing an in-plane X-Y motion using DC motors. Finally, the motorized stage is hanged on an aluminum structure consisting of a 2 cm thick triangular top plate (Fig. 4.6 (b)) with three upper pillars leaning on three solid lower pillars (in red on the picture). The lower pillars possess at their top extremities aluminum rings that prevent the entire upper structure from falling on the table (for clarity, they are shown on the two

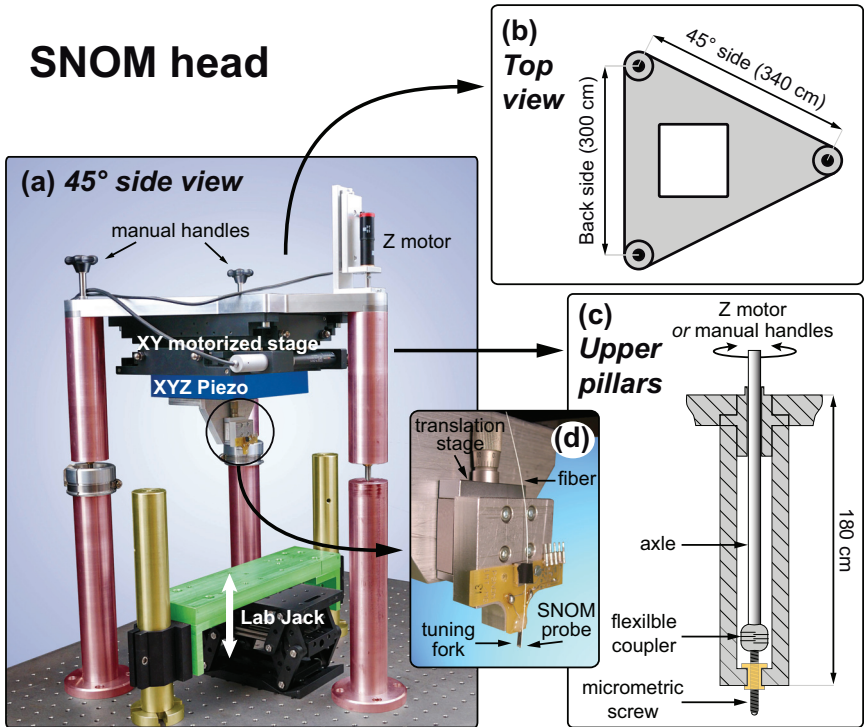


Figure 4.6: (Color online) Picture of the SNOM head with schematic view from the top and from the inner structure of the three upper pillars.

backside pillars only).

As seen in Fig. 4.6 (c), the three upper pillars are hollow with micrometric ball-tipped screws at their base. As in many SNOM designs, the screws rest on the lower pillars on three points: a hole, a groove and a flat [1]. The screws are connected to the head top with steel axle and through flexible couplers. The axle rotations may be induced either by the DC Z motor or by the manual handles. The Z motor is computer driven and leads to a mainly vertical motion of the probe.

In Fig. 4.6 (a), the green plate is dedicated to holding the sample and the

optical set-up required for light injection. This plate is raised with a lab jack (*Thorlabs, Model L490/M*) and slides within the yellow pillars. It is therefore the whole experiment that is raised into proximity to the SNOM probe. In this system, the sample is kept at a fixed position while being raster scanned by the probe.

The probe approach to the sample is performed as follows. The experiment is raised under the probe. Then, the coarse approach is realized by means of the two manual handles and/or the manual translation stage holding the sensor. The fine approach is finally performed by an iterative process cycling between the Z motor and the vertical motion of the piezo stage. The large distance separating the three pillars allows alignment of the XY plane of the piezo stage to less than 0.5 deg with respect to the sample surface by acting on the micrometric screws.

This SNOM head presents several advantages. First, as the lab jack can lift up to 34kg, optical experiments involving heavy apparatus can be performed. Secondly, the large distance between the pillars open significant windows that allow to bring several cumbersome devices (CCD-cameras, binoculars,...) close to the sample. Finally, this structure has shown to be mechanically very stable.

4.2 Measuring amplitudes, phases in polarization-sensitive mode

In the previous section, we have described in detail the different elements constituting the MH-SNOM. In this section, we will derive the fundamental relations measured by the system. We will also assess its amplitude and phase accuracy through a representative experiment corresponding well to the experiments to be performed. Finally, we will introduce a short section dedicated to the spatial Fourier analysis. This tool will indeed be extensively used within the later experimental works.

4.2.1 Field at the detector

The general form of the field intensity at the detector plane is expressed in Eq. 3.13. From the measured lock-in amplitudes R_{ij} and phases Φ_{ij} shown in

Tab. 3.1 and demodulated at $f_{31} = 50$ kHz, $f_{32} = 30$ kHz, $f_{41} = 90$ kHz and $f_{42} = 70$ kHz, one can compute the *measured* scalar complex fields of the MH-SNOM

$$\begin{aligned}
 \hat{E}_{31} = R_{31}e^{i\Phi_{31}} &= \left[2A_1e^{-i(\varphi_1+\Psi_{31})} \right] \cdot A_{3x}e^{i\varphi_{3x}} \\
 \hat{E}_{32} = R_{32}e^{i\Phi_{32}} &= \left[2A_2e^{-i(\varphi_2+\Psi_{32})} \right] \cdot A_{3y}e^{i\varphi_{3y}} \\
 \hat{E}_{41} = R_{41}e^{i\Phi_{41}} &= \left[2A_1e^{-i(\varphi_1+\Psi_{41})} \right] \cdot A_{4x}e^{i\varphi_{4x}} \\
 \hat{E}_{42} = R_{42}e^{i\Phi_{42}} &= \left[2A_2e^{-i(\varphi_2+\Psi_{42})} \right] \cdot A_{4y}e^{i\varphi_{4y}}.
 \end{aligned} \tag{4.7}$$

Since the reference amplitudes and phases are constant (Ψ_{ij} as well), so are the quantities in the brackets. The four complex fields are therefore independently proportional to the object fields. These four measured quantities constitute the fundamental relations provided by the system.

The amplitudes of the four signals are provided by $|\hat{E}_{ij}| = R_{ij}$ and the phases by $\arg(\hat{E}_{ij}) = \Phi_{ij}$. As will be shown on several occasions in this work, much useful information can be extracted from these relations as long as any quantitative comparison is required. In principle, a quantitative comparison implies the knowledge of both the reference amplitudes and phases (and the electronic phases Ψ_{ij}), and the object amplitudes before the illumination system (see Fig. 4.1). In practice, while knowing these amplitudes is relatively simple through independent intensity measurements, the assessment of the optical and electronic phases requires a calibration procedure.

For quantitative *intensity* comparison, we first measure the reference intensities $I_1 = A_1^2$ and $I_2 = A_2^2$, and the intensity ratio $r_{43}^0 = I_4^0/I_3^0$, where I_3^0 and I_4^0 are the intensities of the object beams before the illumination system. From Eqs. 4.7 and accounting for the fact that the object beams may have different intensities while illuminating the sample, the intensities $I_3 = A_{3x}^2 + A_{3y}^2$ and $I_4 = A_{4x}^2 + A_{4y}^2$ at the sample surface are retrieved from

$$I_3 = r_{43}^0 \left[\frac{R_{31}^2}{4I_1} + \frac{R_{32}^2}{4I_2} \right] \quad \text{and} \quad I_4 = \left[\frac{R_{41}^2}{4I_1} + \frac{R_{42}^2}{4I_2} \right] \tag{4.8}$$

If $I_1 \simeq I_2$ and $I_3^0 \simeq I_4^0$, a good approximation to the above equations is

$$I_3 = \frac{R_{31}^2 + R_{32}^2}{2\bar{I}} \quad \text{and} \quad I_4 = \frac{R_{41}^2 + R_{42}^2}{2\bar{I}}, \tag{4.9}$$

where \bar{I} represents the mean value of the total power reaching the detector. Because the heterodyne signals are very small and periodic in time, the mean value over an entire scan of the detected power indeed corresponds to $\bar{I} = A_1^2 + A_2^2$. Eqs. 4.9 are convenient because \bar{I} is acquired in parallel with the heterodyne signals. The variations of I_1 , I_2 , I_3^0 and I_4^0 while tuning the wavelength will be addressed in Sec. 4.3.1.

In addition to the four lock-in amplifiers providing the above signals, two additional lock-in amplifiers are locked at the beat frequencies $f_{21} = 20$ kHz and $f_{43} = 40$ kHz, i.e., the interference between the two references and the two signals respectively. They provide the following signals

$$\begin{aligned}\hat{E}_{21} &= R_{21}e^{i\Phi_{21}} = 2A_1A_2e^{-i(\varphi_2 - \varphi_1 + \Psi_{21})} \\ \hat{E}_{43} &= R_{43}e^{i\Phi_{43}} = 2A_3A_4e^{-i(\varphi_4 - \varphi_3 + \Psi_{43})}.\end{aligned}\tag{4.10}$$

In principle, due to the orthogonality of the references, $\hat{E}_{21} \simeq 0$. In practice, there is always a small amount of cross-talk between the references. R_{21} is therefore a good indicator of the orthogonality between the references (see Sec. 4.3.3) whereas Φ_{21} shows whether the phase drifts in the system are relevant or not (see Sec. 4.4). As the transmission through a SNOM probe is extremely weak (typically 10^{-6} for coated probes), the heterodyne signal at frequency f_{43} is disregarded in the following work. It remains available however for future investigation.

4.2.2 Amplitude and phase accuracy

In this section we assess the signal to noise ratio (SNR) as well as the amplitude and phase accuracy of the heterodyne signals. This is performed through a representative experiment that corresponds well to the experiments to be performed. A SNOM probe is directly illuminated with the object channels at normal incidence ($\lambda = 1520$ nm). The light is shaped with a receptacle-style collimator (*OZ Optics*) made of an aspheric lens ($f = 20$ mm) and whose beam diameter is about $500 \mu\text{m}$.

The optical power of the references are respectively $P_1 = 0.617 \mu\text{W}$ and $P_2 = 0.625 \mu\text{W}$. As these powers exceed $P_r^{min} = 0.05 \mu\text{W}$ (Eq. 2.14 with $R_0 = 1 \text{ M}\Omega$, $S = 1 \text{ A/W}$, $T = 300 \text{ K}$), the detection is shot noise limited. The object powers

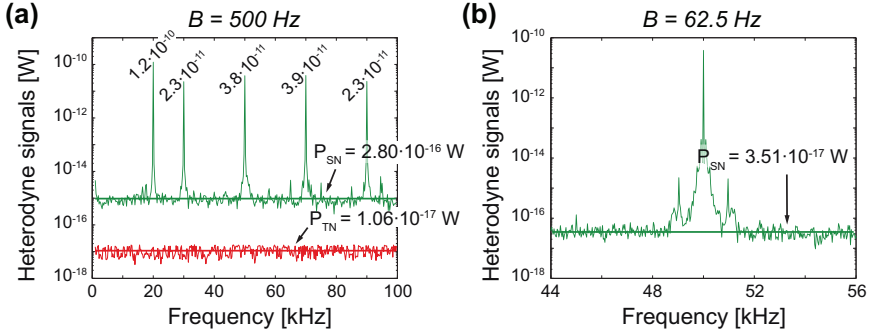


Figure 4.7: (Color online) (a) Measured heterodyne spectrum over 100 kHz ($B = 500 \text{ Hz}$). (b) Measured spectrum around the heterodyne frequency 50 kHz ($B = 62.5 \text{ Hz}$). The shot noise level is about $3.51 \cdot 10^{-17} \text{ W}$, which corresponds to a shot noise level of $2.80 \cdot 10^{-16} \text{ W}$ in a bandwidth $B = 500 \text{ Hz}$.

are $P_3 = 5.1 \text{ pW}$ and $P_4 = 5.2 \text{ pW}$. They have been measured independently by modulating the laser output at 17 kHz and detecting the intensity with a lock-in amplifier (*Stanford Research, Model SR830*).

The detector signal is sent to a spectrum analyzer (*Stanford Research, Model SR770*). A typical spectrum acquired with a bandwidth $B = 500 \text{ Hz}$ is displayed in Fig. 4.7 (a). In addition the thermal noise of the detector followed by the splitter is reported. The powers corresponding to five peaks at the beat frequencies of 20, 30, 50, 70 and 90 kHz are respectively $1.2 \cdot 10^{-10}$, $2.3 \cdot 10^{-11}$, $3.8 \cdot 10^{-11}$, $3.9 \cdot 10^{-11}$ and $2.3 \cdot 10^{-11} \text{ W}$. The noise level is difficult to assess because of the presence of some bumps at the base of the peaks. An additional measurement have been done with a narrower bandwidth ($B = 62.5 \text{ Hz}$) around the peak at 50 kHz. This spectrum is shown in Fig. 4.7 (b). The measured shot noise level is $3.51 \cdot 10^{-17} \text{ W}$. The equivalent shot noise for a bandwidth of 500 Hz becomes $P_{SN} = 2.80 \cdot 10^{-16} \text{ W}$. The corresponding measured SNR_{ij} as well as the amplitude and phase accuracies (Eqs. 3.23) are reported in Tab. 4.2.

At the detector output, the electrical noise corresponding to the shot noise generated by an optical power P_{tot} is evaluated using Eq. 2.7. Dissipated in the

Beat frequencies [kHz]	P_{AC} [W]	SNR [dB]	$\delta A/A$	$\delta\varphi$ [deg]
20	$1.2 \cdot 10^{-10}$	56.4	$1.5 \cdot 10^{-3}$	0.086
30	$2.3 \cdot 10^{-11}$	49.1	$3.5 \cdot 10^{-3}$	0.20
50	$3.8 \cdot 10^{-11}$	51.3	$2.7 \cdot 10^{-3}$	0.16
70	$3.9 \cdot 10^{-11}$	51.4	$2.7 \cdot 10^{-3}$	0.15
90	$2.3 \cdot 10^{-11}$	49.2	$3.5 \cdot 10^{-3}$	0.20

Table 4.2: Measured ac powers, SNR, amplitude and phase accuracies corresponding to each heterodyne signal.

Beat frequencies [kHz]	P_{AC} [W]	SNR [dB]	$\delta A/A$	$\delta\varphi$ [deg]
20	$1.2 \cdot 10^{-10}$	57.9	$1.3 \cdot 10^{-3}$	0.073
30	$2.3 \cdot 10^{-11}$	50.6	$2.9 \cdot 10^{-3}$	0.17
50	$3.9 \cdot 10^{-11}$	52.9	$2.3 \cdot 10^{-3}$	0.13
70	$4.0 \cdot 10^{-11}$	53.0	$2.2 \cdot 10^{-3}$	0.13
90	$2.4 \cdot 10^{-11}$	50.8	$2.9 \cdot 10^{-3}$	0.16

Table 4.3: Calculated ac powers, SNR, amplitude and phase accuracies corresponding to each heterodyne signal.

resistor of the measuring device (see Fig. 4.3), the shot noise becomes

$$P_{SN} = 2eBS P_{tot} \frac{R_0^2 R_L}{(R_L + R_{out})^2}, \quad (4.11)$$

With $P_{tot} \simeq P_1 + P_2 = 1.24 \mu\text{W}$, $B = 500 \text{ Hz}$, $R_L = 1 \text{ M}\Omega$ and $R_{out} = 50 \Omega$, we find $P_{SN} = 1.99 \cdot 10^{-16} \text{ W}$, which agrees quite well with the measured level.

In the same circumstances, the ac electrical powers corresponding to the heterodyne signals (Eq. 3.19) become

$$P_{AC}^{ij} = 2m^2 S^2 P_i P_j \cos(\phi_{ij})^2 \frac{R_0^2 R_L}{(R_L + R_{out})^2}. \quad (4.12)$$

The assessment of the ac powers requires the knowledge of the angles ϕ_{ij} . We assume that the SOPs of the object channels remains linear up to the detector, and that the angle relations 3.20 holds. Then, we find the best angles that fit Eqs. 4.12 with the measured heterodyne powers. We found that with $\phi_{31} \simeq 37.5 \text{ deg}$ and

$\phi_{41} \simeq 128$ deg, the discrepancy between the measured and calculated heterodyne signal is less than 2%. And the difference between these two angles is 90.5 deg, which correspond to nearly orthogonal object SOPs. With the calculated shot noise power, the theoretical SNR_{*ij*} (Eq. 3.21) as well as the amplitude and phase accuracies (Eqs. 3.23) can be calculated. In Tab. 4.3 are summarized the results. Comparing Tab. 4.2 with Tab. 4.3, we find that the theoretical calculations show better SNRs and accuracies. This is due to the measured shot noise which is about 1.5 times greater than the calculated one.

Finally, let us emphasize that the detector is followed by the lock-in amplifiers and the DAQs. The accuracy of the measurements is therefore limited by their accuracies. As seen in Sec. 4.1.3, the analog inputs of the DAQs have a resolution of 2 mV (worst-case scenario). On the other hand, the lock-in accuracy depends on the output channel: amplitude or phase.

The most limiting models (*Stanford Research, Model SR530*) have an amplitude resolution of 12 bits over the 0 – 10 V provided at the output. The *output resolution* is therefore $10/2^{12} = 2.4$ mV and is integrally resolved by the DAQs. However, the maximum output voltage of 10 V corresponds to the full scale sensitivity ζ of the lock-in amplifiers. The resolution of the *measured signal* hence becomes $\delta A = \zeta/2^{12}$. The sensitivity being always smaller than 1 V, the resolution is therefore limited by the DAQ acquisition (indeed, $1\text{ V}/2^{12} = 2.4 \cdot 10^{-4}$ V). To achieve maximum accuracy, the amplitude should be as large a fraction of full scale sensitivity ζ as possible. If we assume that the measured signal has an amplitude $A = k \cdot \zeta$ ($0 \leq k \leq 1$), the amplitude accuracy $\delta A/A$ becomes $k/2^{12}$. Form the lock-in specification, the better phase resolution that can be achieved is 2.5 mV, or $\delta\varphi = 0.05$ deg.

4.2.3 Complex Fourier analysis

The signals captured by the probe while scanning the sample lead to spatially dependent signals. These signals may be either real (topography, detector signal) or complex (amplitudes and associated phases of the optical heterodyne signals). In a number of situations, Fourier analysis helps in finding a particular periodicities or propagating modes. In this work, the Fourier analysis will mainly be

performed on the optical complex fields of Eqs. 4.7 and on the topography. As we are dealing with finite number of pixels, *discrete Fourier transforms* must be considered.

In principle, 2D Fourier transforms may be performed on the 2D data provided by the scans. However, high accuracy 2D maps involve long duration scans that may lead to phase drifts (see Se. 4.4). Non-negligible artifacts in the complex fields may therefore be generated. The clever strategy is to account for the experimental geometry and to reduce 2D scans to 1D high accuracy acquisition lines.

Suppose that the probe acquired N points (pixels) over a distance L : the first and last points corresponds to $x = 0$ and $x = L$ respectively. The discrete signal A may be expressed as

$$A_j = A(x_j), \quad x_j = j dx, \quad dx = \frac{L}{N-1}, \quad j = 0, 1, \dots, N-1 \quad (4.13)$$

where dx is the sampling interval. The discrete Fourier transform H_j of A is hence evaluated on the discrete frequencies ν_j such that [47]

$$\nu_j = \frac{j}{N dx}, \quad j = -\frac{N}{2}, \dots, \frac{N}{2} - 1 \quad (4.14)$$

The minimum value $\nu_{-N/2}$ corresponds exactly to the lower Nyquist critical frequency $f_c = 1/2dx$. The resolution $d\nu$ and dk in the Fourier and k-space ($k = 2\pi\nu$) are thus respectively given by

$$d\nu = \frac{1}{L} \quad \text{and} \quad dk = \frac{2\pi}{L} \quad (4.15)$$

As the X and Y maximum travel ranges of the piezo stages are $100 \mu\text{m}$ (see Sec. 4.1.4), the spatial and k-space resolutions (4.15) become $d\nu = 10^4 \text{m}^{-1}$ and $dk = 6.28 \cdot 10^4 \text{m}^{-1}$. One can note that using the diagonal of the piezo stage could increase the scanning distance by a factor of $\sqrt{2}$, also refining the resolution. However, this alternative complicates considerably the experimental arrangement, and therefore has not been implemented.

If a spatial frequency is identified as an optical propagating mode, the resolution of its effective index n_{eff} becomes

$$dn_{eff} = \lambda d\nu = \frac{\lambda}{2\pi} dk \quad (4.16)$$

where λ is the wavelength. The theoretical effective index resolution is hence $dn_{eff} \simeq 0.015$ (0.0146 at $\lambda = 1460$ nm or 0.0158 at $\lambda = 1580$ nm).

In practice, the number of sampling points N should be taken large enough to avoid *aliasing* effects. Indeed, if the Nyquist frequency f_c is too small with respect to the signal bandwidth, frequencies higher than f_c will appear as spurious frequencies in the measured spectrum [47].

In optics, when an interferometric technique provides both the amplitude $A(x)$ and the phase $\Phi(x)$, the complex optical field $A(x) \cdot \exp(i\Phi(x))$ can be computed and the Fourier analysis applied. In near-field microscopy, such a technique has already proven to be powerful (see [9, 48–50] and references therein).

4.3 Tunability

The wavelength range of the laser source (see Sec. 4.1.1) lies between 1460 nm and 1580 nm. The fibers constituting the multi-heterodyne interferometer are fortunately single mode over this range. However, due to wavelength-dependent phenomena in the system, comparing measurements realized at different wavelengths requires caution. In the next sections, we will address the difficulties that may arise because of the wavelength dependence of the channel powers, and because of parasitic heterodyne frequencies. Finally we will show that the reference polarizations fortunately remain linear and orthogonal over the whole wavelength range.

4.3.1 Power fluctuations due to wavelength tuning

While tuning the wavelength, the powers of the four individual channels constituting the multi-heterodyne interferometer (see. Fig. 4.1) fluctuate. These variations arise as a combined effect of the detector response, the AOM transmission characteristics and the fibered optical components.

The detector has a spectral sensitivity S (see Eq. 2.5) which explicitly varies according to the frequency of light ν , and implicitly through the quantum efficiency η that depends on the optical properties of the material constituting the photodiode. The manufacturer specifications show that the spectral sensitivity S

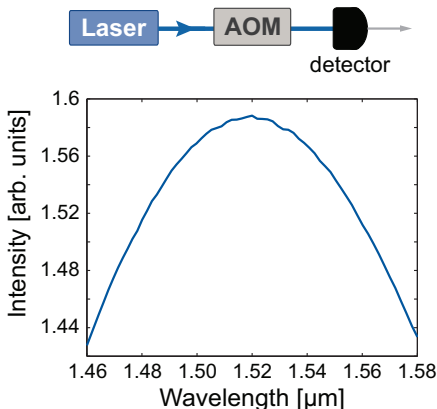


Figure 4.8: (Color online) Wavelength dependance of the output power of an AOM. The AOM is optimized for $\lambda = 1520$ nm with a driving frequency of $f = 40.79$ MHz.

of the overall *InGaAs* photodiode varies no more than 5% over the wavelength range of interest, and so varies the detected signal.

The AOMs also have a wavelength-dependent response. In a simple view, AOMs consist of a transparent crystal (Chalcogenide in this case) in which a propagative acoustic wave of frequency f_0 is created. This wave induces periodic variations of the index of refraction that acts as a grating. As the optical wave propagates through the crystal, the Doppler effect shifts the optical frequency, and the optical output frequencies become $\nu + mf_0$, where ν is the input light frequency and $m = \dots, -1, 0, 1, \dots$ are the indices of the grating orders [33].

The AOMs shown in Fig. 4.1 operate as positive frequency shifters by capturing the first ($m = 1$) diffracted order. These devices being fibered, the output PMFs are aligned with the first diffracted order. This alignment is manufactured for a nominal AOM frequency of $f_0 = 40.00$ MHz at $\lambda_0 = 1550$ nm. While changing the wavelength, the angles of the orders slightly change, leading to a decrease of the output power. In principle, this effect can be compensated by modifying the AOM driving frequency according to the rule

$$\lambda_0 f_0 = \lambda_1 f_1, \quad (4.17)$$

where λ_1 and f_1 are the new optical wavelength and AOM driving frequency.

Figure 4.8 shows the transmitted intensity of an AOM optimized for $\lambda = 1520$ nm, i.e., with Eq. 4.17 the driving frequency becomes $f = 40.79$ MHz ($\lambda_0 = 1550$ nm, $f_0 = 40.00$ MHz). The intensity fluctuations do not exceed 10% over the whole wavelength range. The AOM frequency correction will therefore not be applied unless absolutely necessary. It follows that the best compromise is to set f_1 at 40.79 MHz, which corresponds to the optimal frequency for the central wavelength of the laser wavelength range, i.e., $\lambda = 1520$ nm. The three remaining AOM frequencies are set according to Tab. 4.1: $f_2 = 40.81$ MHz, $f_3 = 40.84$ MHz and $f_4 = 40.88$ MHz.

Finally, the passive optical components themselves also introduce spectral inhomogeneities. Starting from the laser, the power is distributed within the four arms of the multi-heterodyne interferometer by means of PBSs and BSs. These fibered optical components are designed for the nominal wavelength of 1550 ± 40 nm. When departing from these wavelengths, their behaviors (splitting ratios, polarization extinction ratios) are expected to be slightly altered. The laser wavelength range being 1460-1580 nm, shorter wavelengths are expected to exhibit stronger variations.

The overall wavelength dependence of the channel powers – including the detector and AOM responses – have been measured. Figure 4.9 (a) presents the relative intensity ratio ($I_{1,2}/(I_1 + I_2)$) of the references at the level of the detection plane of Fig. 4.1. The observed fluctuations do not exceed 10% for both channels, leading to a maximal intensity ratio of $I_1/I_2 = 1.5$. As $I_{1,2} = A_{1,2}^2$, the corresponding amplitude ratio is approximately 1.2.

Figure 4.9 (b) shows the equivalent relative intensity ratio ($I_{3,4}/(I_3 + I_4)$) of the object channels at the entrance of the illumination system of Fig. 4.1. Compared to the reference case, these curves show less fluctuations but the discrepancy with respect to the ideal value of 0.5 increases at lower wavelengths. At most, the discrepancy reaches 10% for both channels (at $\lambda = 1460$ nm), leading to an amplitude ratio of 1.2.

With respect to the heterodyne signals of Eqs. 4.7, the worst case occurs if one particular reference is 1.2 times greater than the other one, and interferes with

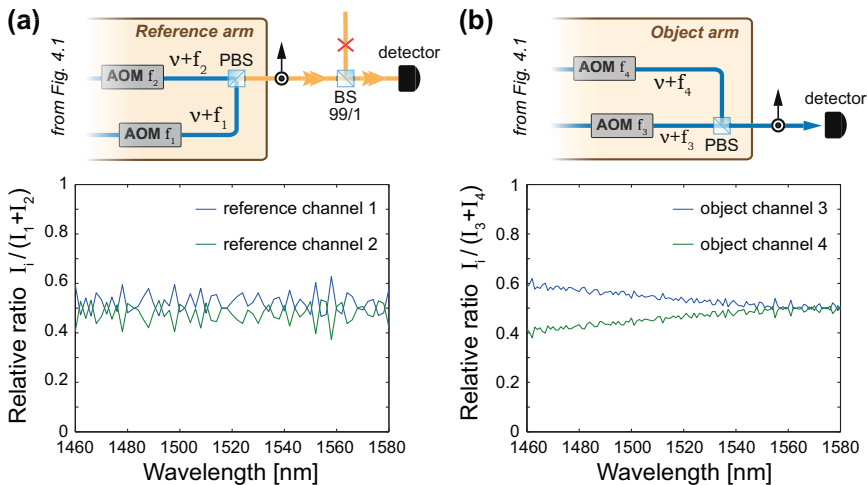


Figure 4.9: (Color online) In (a) is displayed the relative intensity ratios of the individual references at the detection plane as a function of the wavelength. (b) shows the relative intensity ratios of the object channels at the entrance of the illumination system (see. Fig. 4.1).

an object beams 1.2 times greater than the other. In such a case, the heterodyne signal will be 1.5 times too strong with respect to the weaker combination. This result is quite satisfactory as long as fine comparison between heterodyne signals are not required. For fine comparison, the heterodyne signals should be evaluated with Eqs. 4.8.

4.3.2 Spurious heterodyne frequencies

Another challenge while tuning the wavelength arises from the AOM frequency generator. In principle (as mentioned by the manufacturer), the setting of the AOMs should be performed by maximizing their output power. A knob on the generator allows adjustment of the driving electrical power of each AOM. The user should find the knob position that maximizes the AOM output power. However, with respect to the electrical spectrum of the detected intensity, this position may not be optimal. In Fig. 4.10 are displayed two spectra acquired with a

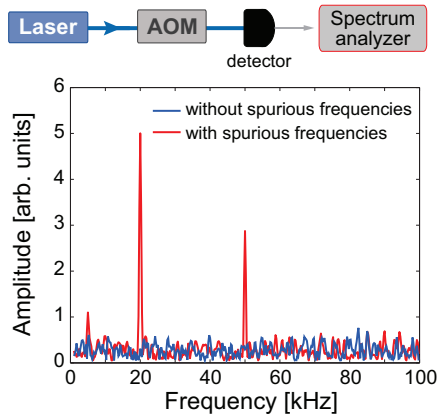


Figure 4.10: (Color online) A variation as small as 0.4% of the AOM output intensity leads to spurious frequency peaks (red) in the detector spectrum with respect to the optimal spectrum (blue).

FFT spectrum analyzer (*Stanford Research, Model SR770*). The red curve has the highest intensity while showing spurious frequency components. With an intensity decrease of about 0.4%, the blue curve reveals a spectrum without additional frequencies.

Interestingly, the two major peaks are at 20 kHz and 50 kHz, which correspond to $f_2 - f_1$ and $f_3 - f_1$. Because all of the other AOMs are disconnected, we attribute this effect to an internal coupling in the frequency generator. Even for the peak-free AOM spectrum, this effect arises again while changing the wavelength. These spurious components matching the heterodyne beat frequencies will result in time varying amplitude modulations and phase distortions. The FFT technique presented in Sec. 4.2.3 may eventually discriminate between wanted and unwanted signals. For fine measurements, it is therefore important to look at the output spectrum of each AOM independently.

4.3.3 Orthogonality of the reference and object channels

The system is designed to generate two references with linear and orthogonal SOPs. Because they evolve in SMFs after their recombination up to the detector

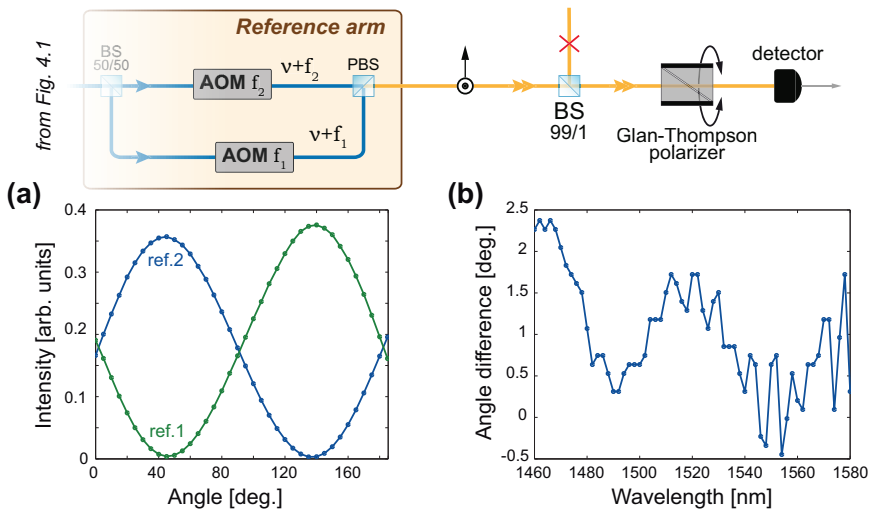


Figure 4.11: (Color online) Linearity and orthogonality of the reference SOPs. A Glan-Thompson polarizer is introduced in front of the detector of the MH-SNOM interferometer (see Fig. 4.1). The object channels are switched *off*. In (a), the detected signal for reference 1 (respectively reference 2) while rotating the polarizer ($\lambda = 1460$ nm). In (b), the angle difference between a maximum of reference 1 and its corresponding minimum for reference 2.

(see Fig. 4.1), it is important to verify that their linearity and their orthogonality are well preserved over the whole wavelength range.

The orthogonality of the reference beams has been verified by introducing a Glan-Thompson polarizer just before the detector of Fig. 4.1. This situation is depicted at the top shown in Fig. 4.11. The polarizer is mounted on a motorized rotation stage (*Standa, Model 8MR151*). The object channels are switched off. We successively measured the intensity produced by reference 1 and 2 at different positions of the polarizer, and at different wavelengths. Figure 4.11 (a) shows a typical result obtain at $\lambda = 1460$ nm. This figure shows out-of-phase sinusoidal profiles whose minima are close to zero. The ratio between the minimum and the maximum for each channel is less than 1.5% over the whole wavelength range. The angular difference between a maximum of reference 1 and the corresponding

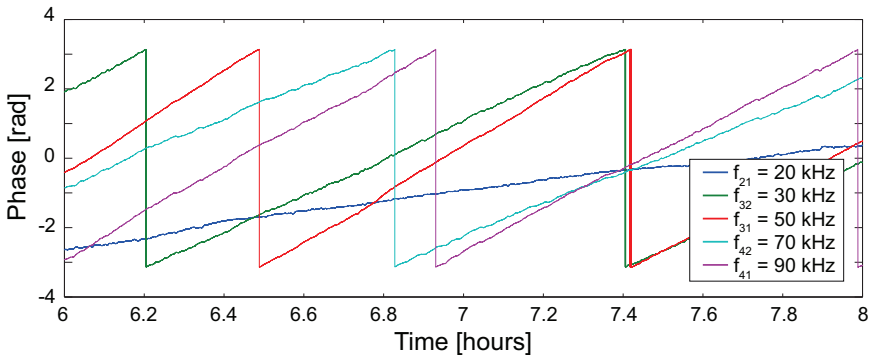


Figure 4.12: (Color online) Assessment of the phase drifts in the multi-heterodyne interferometer. The measurements start 6 hours after initialization of the system. No sample or probes are involved: the illumination fiber is directly connected to the final coupler in Fig. 4.1.

minimum of reference 2 is presented in Fig. 4.11 (b) for different wavelengths. As can be seen, the angular differences do not exceed 2.5 deg. From these observations, the two references can be considered to be linear and orthogonal over the whole wavelength range.

On the other hand, the object channels travel in PMFs since their generation and up to the illumination system (see Fig. 4.1). Their orthogonality as well as their linearity are thus extremely well preserved.

4.4 Phase drifts

While for simple intensity measurements phase drifts are not relevant, they play a crucial role in phase measurements. In order to assess them, we bypass the sample and the probe in Fig. 4.1 and directly connect the illumination fiber to the final coupler. The phases corresponding to the heterodyne signals at $f_{21} = 20$ kHz, $f_{32} = 30$ kHz, $f_{31} = 50$ kHz, $f_{42} = 70$ kHz and $f_{41} = 90$ kHz are acquired over more than 8 hours. Just after initialization, the multi-heterodyne interferometer starts to heat up and the phase drifts are significant. We display in Fig. 4.12 the typical phase measurements after 6 hours and for a time duration

of 2 hours. Among the different curves, the phase of the 50 kHz signal has the fastest evolution. The typical phase drift is approximately 2π radians per hour.

The phase drifts are almost linear. From our experience, it is usually the case after the system has heated up and within the time period corresponding to a scan (max 1 hour). Moreover, they can be assessed before and after the scan with a static acquisition, and the 2D maps can be corrected accordingly. For 1D high resolution lines, they can be neglected (see Sec. 4.2.3).

Such drifts originate first from optical path differences which are difficult to equalize, especially between the reference and object arms (the latter indeed involves the length of the SNOM probe). Secondly, the use of PMFs may cause some issues whenever linear SOPs are not extremely well aligned with the principal (slow and fast) axes. Among the future work that could be pursued on the MH-SNOM, the limitations imposed by phase drifts are probably among the most important.

4.5 Conclusion

In this chapter, a detailed description of the multi-heterodyne scanning near-field optical microscope has been presented. This system allows amplitude, phase polarization-sensitive measurements of optical near and far fields. All of the building blocks constituting the set-up have been presented in detail. The general form of the detected fields has been derived. Through a representative experiment, the signal to noise ratios between the different channels have been found to be around 50 dB, with detected optical powers as low as 5 pW, leading to a phase accuracy of about 0.18 deg. The better phase resolution resolvable by the whole system has been assessed to be 0.05 deg. In practice, this accuracy is however limited by optical and mechanical stability. The issues that may arise while changing the optical wavelength have been discussed. In particular, we have shown that an amplitude discrepancy of no more than 1.5 (worst case) with respect to an ideal measurement is expected between the different heterodyne channels over the whole wavelength range (1460 – 1580 nm). Finally, the maximum phase drifts occurring within the multi-heterodyne interferometer have been found to be approximately 2π radians per hour.

In the next chapters, we will report on the use of the multi-heterodyne scanning near-field optical microscope for the measurements of surface electromagnetic waves. Except the last chapter of this work (Chap. 9) which deals with surface plasmon polaritons, sample involving Bloch surface waves generated in a dielectric multilayer will be presented.

5

Bloch Surface Waves at a planar interface

Surface Electromagnetic Waves (SEWs) are non-radiative electromagnetic waves confined at the interface between two media [51]. Their characteristics are determined by the optical properties of the constituent materials. The most popular SEWs are certainly the Surface Plasmon Polaritons (SPPs). SPPs appear at metallic/dielectric interfaces and correspond to a coupling between photons and plasmons (collective excitation of free electrons in a solid) [52–54]. Another kind of SEWs are the Surface Phonon Polaritons which are formed by a strong coupling of infrared light and optical phonons in polar crystals [9, 55, 56]. SEWs may also be sustained in special conditions at the interface between anisotropic transparent materials [57]. These waves are known as Dyakonov surface waves. Besides homogeneous materials, artificial materials such as Photonic Crystals (PhC) can also sustain SEWs [58–60]. In such materials, SEWs might exist at PhC-air interfaces [57] or at PhC-PhC interfaces [61].

The existence of SEWs in a PhC structure being related to its photonic band structure, such surface optical modes are also called Bloch Surface Waves (BSWs). Their dispersion relations lie within or on the edge of the forbidden bands [62]. In the literature, BSWs are also referred to as Tamm states, surface optical modes or surface photons. In the following work, they will be referred to as BSWs.

Certainly the simplest PhC structure, the dielectric multilayer, may sustain SEWs when properly designed [63, 64]. The first far-field observation of BSWs within a dielectric multilayer was reported in the late 1970's [65, 66]. Although BSWs share common features with SPPs – mainly a strong field confinement close to the interface with the outer medium [67] – BSWs also differ in the sense that they propagate in dielectric materials, and therefore, they are not subject to strong absorptions as SPPs in metals. The low dispersion of the refractive index in dielectric materials also allows a larger spectral tunability. Unlike SPPs which have an exponential amplitude decay on both sides of the interface, BSWs in dielectric multilayers have an exponentially decaying *envelope* into the structure [68]. In general, modes that are located close to the center of the bandgap are shown to be more localized, leading to significantly higher surface electromagnetic fields than modes located near the band edge [69]. Moreover, a careful design of the multilayer allows the generation of two BSWs at the same wavelength and with different penetration depths into the outer medium [70]. These features – with the advantages of choosing the materials, the dimensions and the number of layers – makes BSW-based sensing applications promising [71–74].

5.1 Amorphous silicon nitride multilayer

The planar multilayer that will be described here is fundamental for the rest of this work. Indeed, different polymeric structures will be deposited on the top interface: a subwavelength grating in Chap. 6 and different ultra-thin ridges in Chaps. 7 and 8. The multilayer fabrication was performed by Emiliano Descrovi and Fabrizio Giorgis at the Materials and Microsystems Laboratory χ Lab (Politecnico di Torino, Italy), and the calculations by Emiliano Descrovi.

The structure is presented in Fig. 5.1. The multilayer is composed of hydrogenated amorphous silicon nitride grown by Plasma Enhanced Chemical Vapor

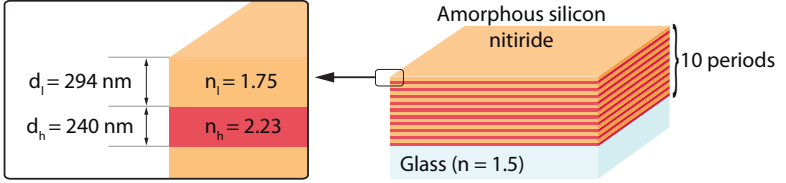


Figure 5.1: (Color online) Schematic view of the amorphous silicon nitride multilayer used in this work.

Deposition (PECVD) on a $500\ \mu\text{m}$ thick glass substrate (*Corning*, $n_p = 1.5$). The composition of the layers is controlled by varying the fraction of ammonia in the $\text{SiH}_4 + \text{NH}_3$ plasma. The multilayer consists of 10 periods of alternating high index ($n_h = 2.23$ at $\lambda = 1530$ nm) and low index ($n_l = 1.75$ at $\lambda = 1530$ nm) layers whose thicknesses are $d_l = 294$ nm and $d_h = 240$ nm respectively. The top layer has a low index. This structure was designed to support only TE-polarized BSWs. Fabrication details may be found in [50]. The choice of the polarization is somehow arbitrary since structures sustaining TM-polarized BSWs can also be realized. However, the band diagrams for TM polarization show additional features such as Brewster points that complicate slightly the design [75].

The band diagram associated with an infinite stack of layers is presented in Fig. 5.2. The abscissa axis refers to the propagation constant β of light guided within the structure (parallel to the multilayer interfaces). The white regions indicate forbidden bands, while the dashed lines represent the dispersion relations $\omega = \beta c$, $\omega_p = \beta c/n_p$, $\omega_l = \beta c/n_l$, $\omega_h = \beta c/n_h$ of the free photons propagating in vacuum, in the substrate, in the low and high refractive index layers, respectively. If we consider a *truncated*, semi-infinite multilayer, the BSW dispersion curve can be calculated using Maxwell's equations. In the past, several computational methods have been proposed (see e.g. [75] and references therein). With the help of a well-known matrix method [76], we found that the proposed multilayer sustains a BSW in the first forbidden band, slightly beyond the vacuum light line and at the multilayer-air interface. The dispersion relation corresponds to the BSW curve in Fig. 5.2. As the BSW curve lies above the high and low index light lines, the field in both layers are propagating. The portion of the BSW dispersion which is localized above to the substrate line corresponds to the states that can

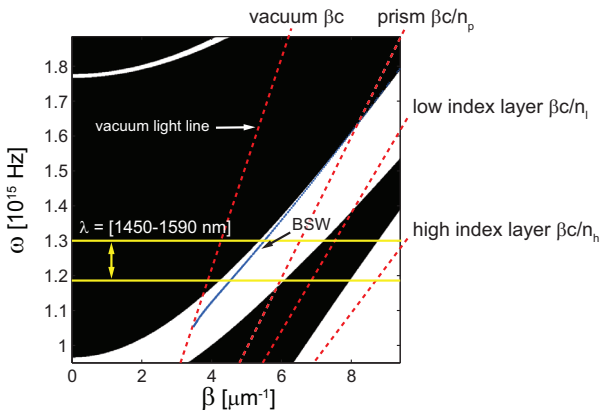


Figure 5.2: (Color online) Calculated band diagram (TE polarization) of a multilayer consisting of an infinite sequence of high ($n_h = 2.23$) and low ($n_l = 1.75$) refractive index layers whose thickness are $d_h = 240$ nm and $d_l = 294$ nm respectively. The white regions indicate the forbidden bands. In addition, the BSW dispersion curve associated with the truncated silicon nitride multilayer is also shown.

be excited with a prism, for example.

The light lines of the high and low index layers are displayed for historical reasons. In their fundamental work, Yeh *et al.* have indeed analyzed surface modes located between these two lines [77], resulting in fields with propagating behavior in the higher index medium while being evanescent in the lower index medium.

5.2 Far-field characterization

The far-field characterization method described here has been implemented by Lorenzo Dominici and Francesco Michelotti at the Dipartimento di Energetica (SAPIENZA, Università di Roma and CSIM, Italy). The dispersion curves which will be measured with this technique will be necessary for the consistency of the discussion. We will refer to this method in the current chapter as well as in Chap. 6, 7 and 8.

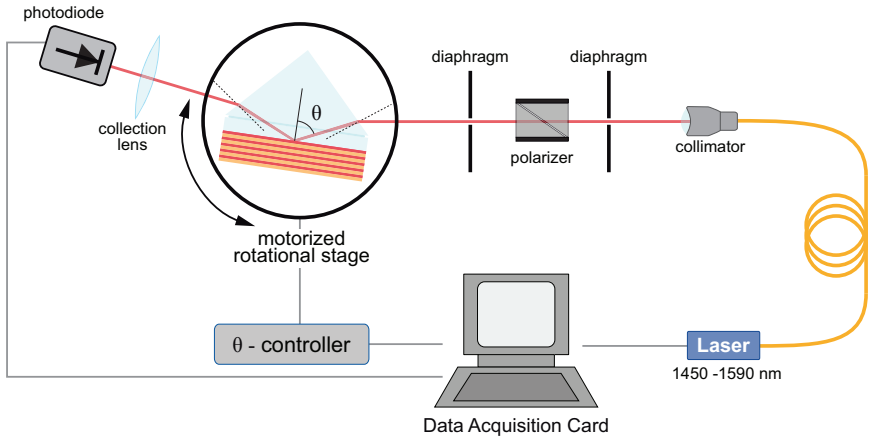


Figure 5.3: (Color online) Sketch of the ellipsometric setup in the Kretschmann-Raether configuration used for the far-field characterization of BSWs coupled to the silicon nitride multilayer.

5.2.1 Far-field characterization technique

A schematic of the setup is shown in Fig. 5.3. A collimated and TE-polarized beam is expanded from a fibered tunable diode laser source (*Nettest, Model Tunics-Plus*) and used to illuminate the sample through the input facet of a 45 deg BK7 glass prism ($n_p = 1.50$). The angular divergence of the illuminating beam is estimated to be $\delta = 0.038$ deg. The sample is contacted to the prism facet by means of a proper index matching liquid. Angular reflectance profiles at fixed wavelengths are obtained by means of a single channel detection scheme, in which the sample is rotated with respect to the incident beam. The parameter θ is the angle between the normal to the multilayer planar interfaces and the direction of the incident beam at the prism/multilayer interface. A low numerical aperture lens collects and focuses the reflected light onto the photodiode. As the angular orientation of the sample varies, the collection lens and the photodiode are rotated accordingly.

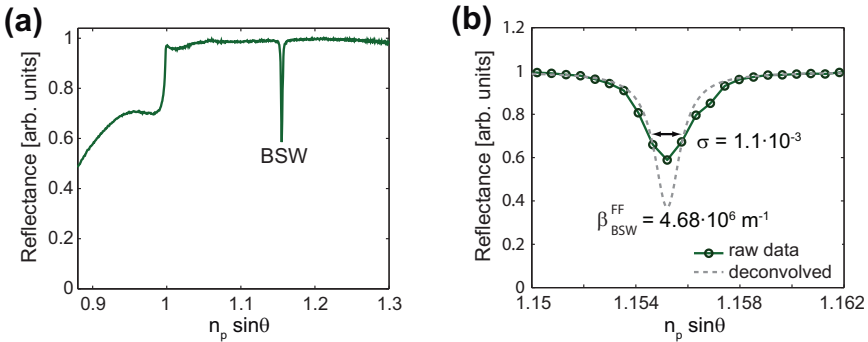


Figure 5.4: (Color online) (a) Experimental far-field angular reflectance in the Kretschmann configuration. (b) Reflectance anomaly associated with the BSW coupling (raw and deconvolved data).

5.2.2 Propagation constant and attenuation length

In the Kretschmann configuration, the propagation constant β of the guided modes propagating in the structure can be calculated through $\beta = n_p 2\pi \sin \theta / \lambda$, where the incidence angle θ of the incident light is considered at the multi-layer/glass interface. According to the band diagram shown in Fig. 5.2, we expect to couple BSWs in the first forbidden band at incidence angles slightly larger than the critical angle.

The full BSW dispersion curve in the wavelength range 1450-1590 nm may be found in [78]. Fig. 5.4 shows the angular reflectance profile measured at a fixed wavelength $\lambda_{BSW} = 1550$ nm. The angular position of the cusp in Fig. 5.4 (a) lies on the vacuum light frequency $\omega = \beta c$ shown in Fig. 5.2, while the sharp dip represents a reflectance anomaly indicating BSW coupling. The dip centered at the angle θ_{BSW} corresponding to $n_p \sin \theta_{BSW} = 1.1553$, leads to the far-field estimation of the propagation constant $\beta_{BSW}^{FF} = n_p \sin \theta_{BSW} \cdot 2\pi / \lambda_{BSW} = 4.683 \mu\text{m}^{-1}$. No reflectance dip is observed for a TM-polarized illuminating beam.

As described by Ulrich in [79], the bandwidth of reflectance anomalies can be used to calculate the decay length of prism-coupled waveguide modes. Nevertheless, a significant broadening of the measured reflectance dips occurs due to the angular divergence of the illuminating beam. In fact, for given coupling

strength conditions, the measured reflectance anomalies result from a convolution of the waveguide transfer function with the angular spectrum of the incident beam. In the far-field characterization method, a gaussian beam whose measured angular divergence is about $\delta \simeq 0.038$ deg is used. The corresponding waist becomes $w_0 = \lambda/\pi\delta = 744 \mu\text{m}$. In order to remove the influence of the finite size of the illuminating beam, a one-dimensional deconvolution of the measured reflectance anomaly by the beam angular spectrum is performed. The result has a Lorentzian profile, as shown by the dashed curve of Fig. 5.4 (b). The full bandwidth of the deconvolved profile is $\sigma = 1.1 \cdot 10^{-3}$ and approximates the BSW losses for a plane-wave excitation. The far-field estimation of the BSW decay length is $L_{BSW}^{FF} = (\pi\sigma/\lambda_{BSW})^{-1} = 448.5 \mu\text{m}$. The decay of the mode along the propagation direction results from absorption in the material, surface scattering and leakage into the prism. Nevertheless, due to the low absorption of silicon nitride in the near-infrared (NIR) range and to the low roughness of the multilayer surface [80], the BSW is mainly attenuated by light leakage into the prism. Such a backward coupling can be suppressed with a local coupling region such as an excitation close to the edge of the prism or with a local grating.

Once the BSW decay length is known, an estimation of the coupling strength can be performed. We consider the ratio $L_{BSW}^{FF}/w_0 = 0.634$ as a coupling parameter, demonstrating that the far-field measurements are conducted under coupling conditions close to the optimum [79]. This allows a rather large fraction of the incident power to be transferred to the BSW and to be guided with low losses.

5.3 Near-field experiment

We use the Multi-Heterodyne Scanning Near-Field Optical Microscope (MH-SNOM) described in Chap. 4 to investigate the optical response of the multilayer. As shown in Fig. 5.5, the sample is illuminated in the Kretschmann configuration. A 45 deg BK7 prism holds the sample and an appropriate index matching fluid is used. The illumination is provided by either a focuser or a collimator (*OZ Optics*). They are mounted on a goniometric stage placed on a 3-axis translation stage. The focuser (or collimator) output is rotated in order to generate TE and TM-polarized illumination with the object channels 3 and 4 of Fig. 4.1

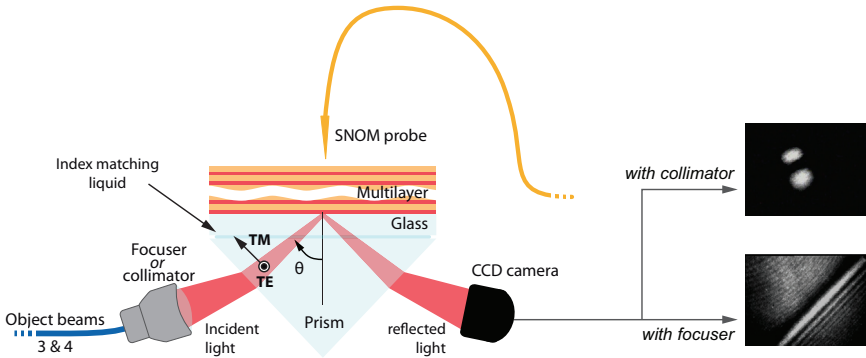


Figure 5.5: (Color online) The sample is illuminated in the Kretschmann configuration with a focused or collimated beam. At right, two images showing the absorption line observed with the CCD camera when the BSW coupling occurs.

(Chap. 4), respectively. The optical response of the multilayer under TE (resp. TM) illumination is therefore expected at heterodyne frequencies $f_{31} = 50$ kHz and $f_{32} = 30$ kHz (resp. $f_{41} = 90$ kHz and $f_{42} = 70$ kHz).

The reflected light is detected by an infrared-sensitive CCD camera arranged in a standard single wavelength M-line configuration (see e.g. [81]). For well defined angle θ_{BSW} and wavelength λ_{BSW} , the TE-polarized light couples to a BSW: an absorption line is then observed in the far field on the CCD camera. Typical absorption lines are shown in Fig. 5.5 for focused and collimated illuminations.

5.4 Bloch surface waves near-field distribution

We focus the combined TM and TE polarized beam on the multilayer surface through the coupling prism. The beam wavelength and incidence angle are $\lambda_{BSW} = 1550$ nm and $\theta = \theta_{BSW}$, respectively. Because the multilayer is designed to couple only TE-polarized light to the BSW in the 1450 – 1590 nm spectral range, the near-field distributions associated with the two orthogonal polarizations are expected to be different at the multilayer surface; the TM-

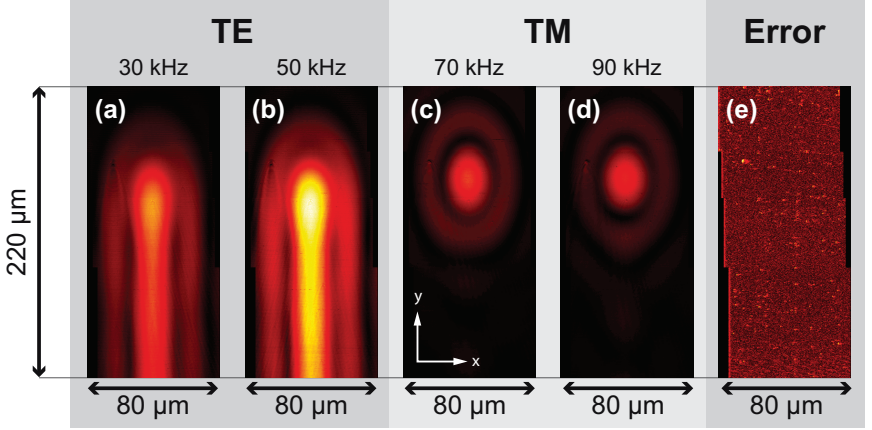


Figure 5.6: (Color online) Amplitudes of the optical near-field collected by the MH-SNOM at the multilayer surface: (a-b) TE-polarization (object channel 3) projected onto the two references 1 and 2 of Fig. 4.1 (heterodyne beat frequencies at 30 and 50 kHz), (c-d) TM-polarization (object channel 4) projected onto the same references (heterodyne beat frequencies at 70 and 90 kHz). Illumination wavelength $\lambda = 1550$ nm, incidence angle $\theta = \theta_{BSW}$. (e) Shear-force error signal map.

polarized light being evanescent through Total Internal Reflection (TIR). The simultaneously obtained four amplitudes of Eqs. 4.7 are displayed in Figs. 5.6 (a-d). Figures 5.6 (a-b) shows the TE response of the multilayer, whereas Figs. 5.6 (c-d) shows its TM response¹. A normalization is performed with respect to the amplitude maximum.

The tip-sample distance is controlled by means of a shear-force feedback system working in constant-height mode. The SNOM tip is kept in close proximity to the sample surface during the scanning process. The shear-force error map shown in Fig. 5.6 (e) reveals the presence of topographic defects. Because the allowed X and Y lateral displacement of the piezo scanner is only $100 \times 100 \mu\text{m}$, larger areas are obtained through series of spatially overlapping maps stitched

¹The intensity patterns corresponding to Eqs. 4.9 are shown in Ref. [50] instead of the four amplitudes.

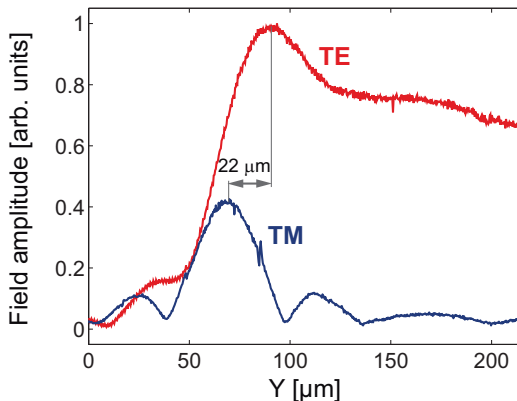


Figure 5.7: (Color online) Cross sectional normalized amplitude distribution of the TE and TM polarized near fields on the multilayer surface measured along the line $x = 0$.

together using the error signal. Coarse positioning of the probe is achieved using the motorized stage (see Sec. 4.1.5). Here, four scans are joined together.

The near-field maps of Fig. 5.6 provide direct evidence of BSW coupling. The TM-polarized field appears as an elongated Airy pattern. In the focal plane of the incident focused beam, the optical field has an Airy-like distribution due to the diffraction at the focuser entrance pupil. The observed elongation is due to the combined effect of refraction at the prism input facet and the geometrical projection of the focused incident beam onto the multilayer surface. The horizontal spot size gives an indication of the beam waist within the prism: $w_0 \simeq 11.4 \mu\text{m}$. In contrast, the TE-polarized field appears as a comet-like pattern. We identify a radiation coupling region, where an elongated Airy-like distribution showing a strong, asymmetric deformation in the y direction is observed. Far from the coupling region, a low divergence “comet tail” reveals BSW propagation.

A more detailed analysis of the near-field distribution can be performed by considering the cross-sectional field distributions. Because the time duration of each individual scan in Fig. 5.6 takes at least 90 minutes, the relative orientation of the object beam with respect to the references slightly changes: the ratio between the TE amplitudes at 30 kHz and 50 kHz changes by 3%. It is therefore

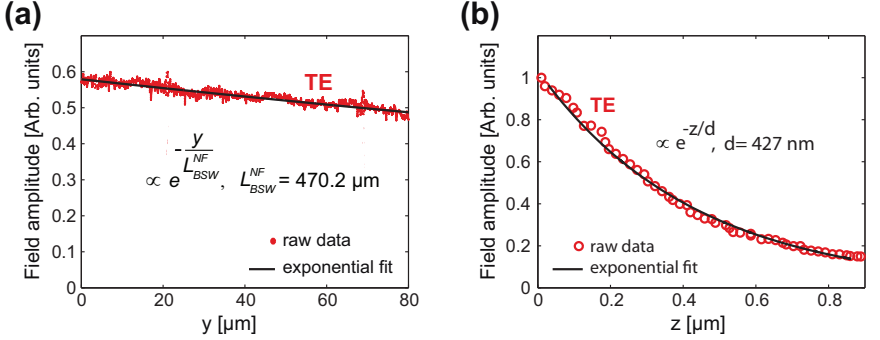


Figure 5.8: (Color online) (a) Amplitude profile of the BSW along the propagation direction. The best exponential fit returns a decay length $L = 470.2 \mu\text{m}$. (b) Amplitude profile of BSW as a function of distance from the multilayer surface. The best exponential fit returns a decay distance $d = 427 \text{ nm}$.

more appropriate for quantitative measurements to work on the TE amplitude given by the square root of Eq. 4.9 (as done in [50]). Figure 5.7 shows the normalized amplitudes of both the TE and TM fields along the line $x = 0$ (the propagation axis of the BSW).

The shift of the TE-polarized amplitude maximum in the forward direction with respect to the TM-polarized maximum highlights the resonant coupling of the BSW. In the case of a purely gaussian incident beam, such a shift monotonically increases as the coupling strength diminishes. In particular, for a coupling parameter $L_{BSW}^{FF}/w_0 = 448.5/11.4 \simeq 40$, Ulrich [79] predicts a positive shift of the intensity maximum $y_M^{theory} \simeq 1.7 \cdot w_0 = 19 \mu\text{m}$ which is rather close to the experimentally observed $y_M^{exp} = 22 \mu\text{m}$.

One effect due to weak coupling is the tiny near-field enhancement associated with the prism-coupled surface modes [82]. We observe a BSW amplitude maximum ~ 2.5 times as large as compared to the TM-polarized TIR field. In the next section we will show that the BSW near-field intensity can be greatly enhanced by means of a collimated beam increasing the coupling strength.

Far from the region of incidence, the traveling BSW is slowly attenuated

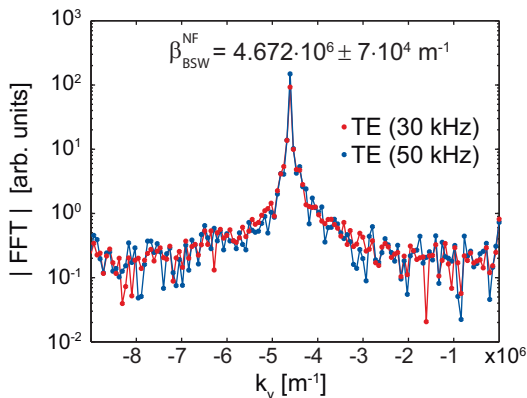


Figure 5.9: (Color online) One-dimensional Fourier Transformation (absolute value) of the two complex fields corresponding to the TE polarization. The fields are acquired in the comet tail region and along the propagating direction.

mainly because of back-coupling into the prism. In this case, the field distribution in the propagation direction can be described with decreasing exponential functions. In order to estimate the BSW decay length, we perform a one-dimensional scan in the y direction centered on the BSW ($x = 0$). Only the comet tail region is observed. As shown in Fig. 5.8 (a), the BSW amplitude gradually decreases in the propagation direction. Due to the low absorption of silicon nitride in the NIR region, the losses are essentially due to back-coupling of light into the prism. Furthermore, in Fig. 5.8 (b), the SNOM probe is kept at constant x and y position while the probe approaches the multilayer surface: the surface mode is only weakly scattered by the film roughness and remains tightly confined to the sample surface. Best-fit curves of the measured near-field amplitude profiles shown in Fig. 5.8 indicate an attenuation length of $L_{BSW}^{NF} = 470.2 \mu\text{m}$ in the propagation direction and a decay distance of $d = 427 \text{ nm}$ normal to the multilayer surface. The slightly larger value of L_{BSW}^{NF} with respect to L_{BSW}^{FF} may be due to the presence of some residual direct illumination in the scanned region.

We will now find the propagation constant of the BSW by applying the Fourier analysis developed in Sec. 4.2.3. A high resolution scan (4096 points) is acquired

over $90 \mu\text{m}$ along the comet tail. The resolution in the Fourier space becomes (Eq. 4.15) $dk_y \simeq 7 \cdot 10^4 \text{ m}^{-1}$.

In Fig. 5.9 are displayed the absolute values of the Fourier spectra corresponding to both TE signals (at 30 kHz and 50 kHz). Both spectra match well. The large amplitudes and the frequency positions of the main peaks indicate that, far from the coupling region, the TE-polarized near-field is essentially harmonic, with propagation constant $\beta_{BSW}^{NF} = 4.672 \pm 0.07 \mu\text{m}^{-1}$. The rather large width of the peak is a spurious effect due to improper truncation of the signal in the real space that leads to a non-integer number of wave periods into the Fourier analysis. The difference between β_{BSW}^{NF} and β_{BSW}^{FF} evaluated in the far-field falls within the bounds of the experimental error dk_y .

Finally, it is straightforward to verify that with the propagation constant $\beta_{BSW}^{NF} = 4.672 \pm 0.07 \mu\text{m}^{-1}$ and the decay distance $d = 427 \text{ nm}$, the magnitude of the wavevector in air can be retrieved

$$|\mathbf{k}| = \sqrt{\beta_{BSW}^{NF\ 2} - \left(\frac{1}{d}\right)^2} = 4.04 \cdot 10^6 \text{ m}^{-1}, \quad (5.1)$$

which represents a discrepancy of less than 0.2% with respect to the theoretical value of $k = 2\pi/\lambda = 4.05 \cdot 10^6 \text{ m}^{-1}$ ($\lambda = 1550 \text{ nm}$).

5.5 Field enhancement

It is well known that the amplitude of the electromagnetic field is strongly dependent on the vertical confinement of the BSW on the multilayer surface. It has been shown that an increase of such a confinement can be obtained by a proper tailoring of the last multilayer layer, thus resulting in an electromagnetic field enhancement factor of several orders of magnitude [69, 83].

In a given layered structure, the coupling strength determines the power density distribution of coupled modes as well as the maximum intensity value within the guiding medium or at the structure boundaries. In the previous section, the BSW has been weakly excited by means of a focused incident beam (waist $w_0 = 11.4 \mu\text{m}$) in such a way that a slowly decaying guided mode was observed

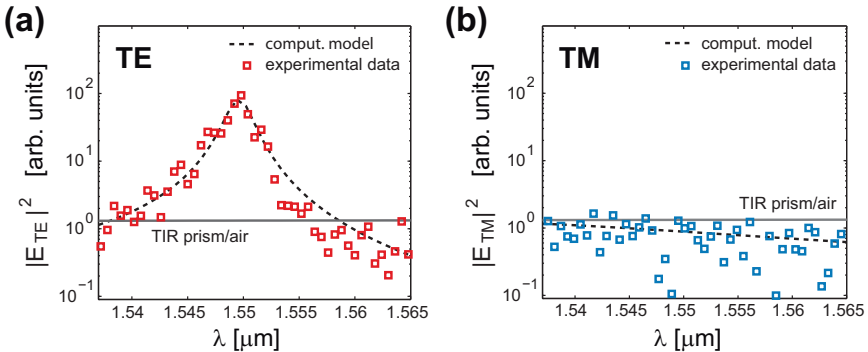


Figure 5.10: (Color online) Near-field intensity spectrum of (a) a TE and (b) a TM-polarized evanescent field on the multilayer surface. The polarization-dependent field-enhancement effect is associated with the excitation of a TE-polarized BSW. For comparison purposes, the near-field spectrum of a simple glass/air interface illuminated under TIR conditions at a fixed angle is also shown (gray line in both figures).

far from the directly illuminated coupling region. Nevertheless, the near-field enhancement associated with the BSW was rather small.

To appreciate more directly the field enhancement, we excite a BSW at $\theta = \theta_{BSW}$ using a collimated beam (divergence $\delta = 4 \text{ mrad}$, waist $w_0 = \lambda/\pi\delta = 120 \mu\text{m}$ at $\lambda = 1550 \text{ nm}$). In this configuration, the coupling parameter at $\lambda = 1550 \text{ nm}$ diminishes to $L_{BSW}^{NF}/w_0 = 470.2/120 \simeq 3.9$ and a strong increase in the near-field intensity is expected. We place the SNOM probe in proximity to the surface and keep it at a fixed position on the sample while tuning the wavelength. During the wavelength sweep, the TE and TM near-field intensities spectrum are measured (Eq. 4.9). The incidence angle is set in such a way that a near-field intensity maximum is obtained at $\lambda = 1550 \text{ nm}$. The measured results are reported in Fig. 5.10.

The absolute TE and TM near-field intensities can be directly compared. We observe that the near-field spectrum for the TE polarization shows a peak at approximately $\lambda = 1550 \text{ nm}$, where the detected intensity is almost two orders of magnitude larger than that of the corresponding TM polarization. In addition to

the experimental measurements, we rigorously calculate the near-field intensity spectrum generated by a one-dimensional gaussian beam of waist $w_0 = \lambda/\pi\delta$ and for wavelengths lying between 1535 and 1565 nm. In our computational model (C-method), we consider a BSW excitation whose angle corresponds to an efficient coupling at $\lambda = 1550$ nm. We consider a Kretschmann geometry in which a set of plane waves belonging to the angular spectrum of the incident gaussian beam illuminates the multilayer structure. Finally, the calculated electric fields for each angular spectrum component are coherently summed. These results are superimposed on the experimental data in Fig. 5.10. We note that the calculated spectra are normalized by an arbitrary factor obtained by best fitting to the experimental data. We only consider the TE case in the fit process: the calculated near-field TM-polarized spectrum is normalized by the same factor.

The near-field spectrum for TE polarization shows a fairly well-defined resonant Lorentzian shape, whose width and height match the measured profile. At the multilayer surface, the maximum intensity peak at $\lambda = 1550$ nm is more than 10^2 times the intensity predicted for a simple glass/air interface. This measurement directly demonstrates the effect of near-field enhancement on the surface of properly designed photonic structures. It is interesting to note that, outside the BSW resonance region, the near-field intensity is smaller than in the case of a glass/air interface. This is due to the presence of the photonic structure, which is a dielectric multilayer mirror and more strongly attenuates the (evanescent) light tunneling to the surface of the device. A similar effect also applies to the TM-polarized field.

These measurements represent an unprecedented direct quantification of the field enhancement associated with BSWs, without using any supplemental model based on far-field observation [84].

5.6 Multilayer covered with a thin dielectric layer

This section represents the connection to the next three chapters. Indeed, we will deal with ultra-thin (height about 100 nm) dielectric structures deposited on the top interface of the multilayer. The first step towards dielectric structures is to understand what happens if the bare multilayer is covered with a planar and

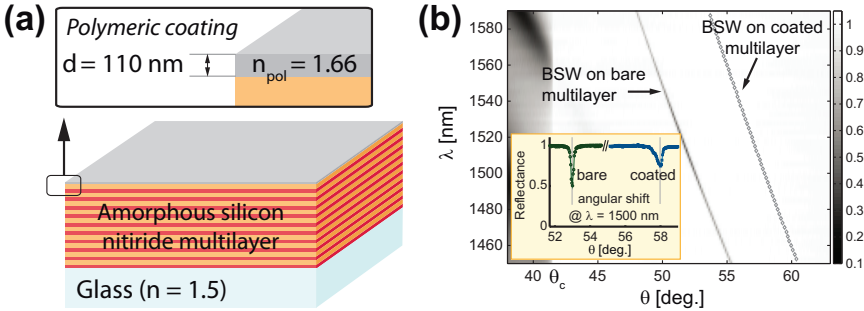


Figure 5.11: (Color online) (a) Schematic view of the silicon nitride multilayer covered with a 110 nm thick polymeric layer. (b) Measured dispersion curve of the bare multilayer (left) on which is added the position of the reflectance dips of the coated multilayer (right).

uniform ultra-thin polymeric layer.

The multilayer used up to now (see Sec. 5.1) is covered with a 110 nm thick spin coated polymeric layer (positive photoresist, *Clariant GmbH, AZ5214E*). The structure is schematically shown in Fig. 5.11 (a). In Fig. 5.11 (b) is shown the far-field dispersion curve of the bare multilayer (left) as obtained by the far-field characterization method described in Sec. 5.2.1. In addition are displayed the position of the reflectance dips of the coated multilayer measured with the same method.

As the BSW propagation constant is obtained through $\beta = n_p 2\pi/\lambda \cdot \sin \theta$ (n_p being the refractive index of the prism), adding a thin dielectric coating results in a shift of the propagation constant to higher values. Interestingly, such a thin coating results in two spectrally and angularly well separated BSW modes. Together with the remarkable narrowness of the dips (inset), it will constitute the basic mechanism for BSW waveguides that will be studied in Chap. 8.

Finally, the far-field dispersion curves allow to define an effective index n_{eff} for the BSWs such that

$$\beta = n_{eff} 2\pi/\lambda \quad \text{where} \quad n_{eff} = n_p \cdot \sin \theta. \quad (5.2)$$

The effective index concept will be particularly useful when dielectric struc-

tures will be deposited on the multilayer.

5.7 Conclusion

A near-field analysis of BSWs coupled in a silicon nitride multilayer has been presented. This work provides an important insight into several interesting aspects of BSW coupling and propagation characteristics.

A BSW can be weakly coupled into a dielectric multilayer with a moderately focused TE-polarized beam in the Kretschmann configuration. Similarly to surface plasmons on metallic films [85], the near-field spatial distribution of the mode shows an Airy-like coupling region due to the distortion of the direct beam illumination in the BSW forward direction. The Fourier analysis based on the measured mode amplitude showed that, far from the region of incidence, only the k -component matching the propagation constant β of the BSW mode survives. The BSW decay constant estimated by the near-field measurements is $L_{BSW}^{NF} = 470 \mu\text{m}$. The attenuation is mainly due to radiative leakage through the prism rather than material absorption. Thus, it can be drastically reduced by propagating the BSW on a free guiding structure without a prism.

If BSWs are more strongly coupled, an evident field enhancement is observed in the near field. By using a collimated beam, we have generated a near-field 100 times stronger than the evanescent field at the glass/air interface. These results make surface waves coupled into dielectric multilayers an interesting alternative to surface plasmons in sensing applications.

The main results of this chapter have been published in [50].

6

Bloch surface waves within a multilayer covered by a shallow dielectric grating

In this chapter, we consider Bloch Surface Waves (BSWs) within a dielectric structure constituted by a silicon nitride multilayer covered with a subwavelength dielectric grating. There is a growing interest in investigating the interaction of surface waves with periodic structures. Typically, gratings on multilayers are used for mode coupling [86]. Nevertheless, it has been recently suggested that shallow, periodic corrugations realized on top of a multilayer can be used in biosensing applications [72]. For well defined grating geometries, the corrugation opens a bandgap in the dispersion relation of the surface mode [87]. Such a bandgap can be used for enhancing the amplitude of the surface wave [88], for increasing the density of electromagnetic modes [89], or for guiding [90].

In this framework, a near-field microscopy analysis provides important insight

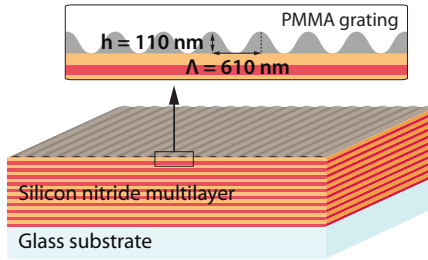


Figure 6.1: (Color online) Schematic view of the polymeric grating (PMMA) deposited on the top interface of the silicon nitride multilayer. The grating height and period are $h = 110 \text{ nm}$ and $\Lambda = 610 \text{ nm}$.

into the spatial distribution of the complex optical field close to a structured interface. In the following, we provide a direct visualization of the surface wave propagation as affected by the presence of the grating.

6.1 Experiment

The base structure is the silicon nitride multilayer described in Sec. 5.1. A 110 nm thick azobenzene side-chain copolymer film (DR1-PMMA, $n_p = 1.67$) spin coated on the air-multilayer interface is holographically illuminated to produce a shallow grating whose period and peak-to-peak amplitude are $\Lambda = 610 \text{ nm}$ and $h = 110 \text{ nm}$, respectively. Fabrication details of the polymeric grating may be found in [78]. A schematic of the sample is shown in Fig. 6.1.

We use the Multi-Heterodyne Scanning Near-field Optical Microscope (MH-SNOM) described in Chap. 4 to investigate the optical response of the structure. The sample illumination is shown in Fig. 6.2 (a). BSWs are coupled in the Kretschmann configuration by means of a BK7-glass prism. The incident light is shaped with either a collimator or a focuser (*OZ Optics*) mounted on a goniometer. The focuser (or collimator) output is rotated in order to generate TE and TM-polarized illumination with the object channels 3 and 4 of Fig. 4.1 (Chap. 4), respectively. Only TE-polarized light couples to the BSWs. The goniometric stage is placed on a 3-axis translation stage. The beam diameter of the

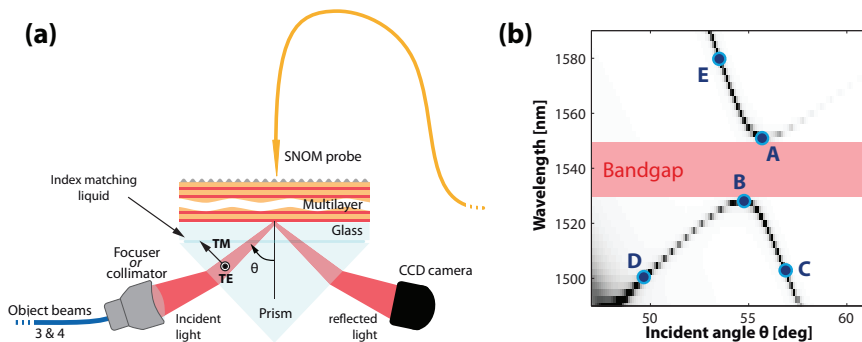


Figure 6.2: (Color online) (a) The sample is illuminated in the Kretschmann configuration with a focused or collimated beam. (b) Far-field measured dispersion curves of the silicon nitride multilayer covered with a shallow PMMA grating. The grating opens a bandgap.

collimator is about $500 \mu\text{m}$. The focuser has a divergence of 4 deg and produces a spot size of about $20 \mu\text{m}$ at the surface of the sample. The grating grooves are placed perpendicular to the plane of incidence. We use an infrared-sensitive charge coupled device (CCD) camera to collect the reflected light and check BSW coupling in a classical M-line configuration [81].

Calculations performed with the well known C-method [76] show that the grating opens a bandgap in the BSW dispersion curve, as shown in Fig. 6.2 (b). The dispersion curve has been measured in the far field [78] with the setup described in Sec. 5.2.1. The black lines identify low-reflectance regions and are associated with BSW coupling. In the following, we focus on five significant points marked by circles on the BSW dispersion curve. We consider the near-field distribution at the band edges (point A at $\lambda_A = 1547 \text{ nm}$, $\theta_A = 55.3 \text{ deg}$ and point B at $\lambda_B = 1524 \text{ nm}$, $\theta_B = 54.5 \text{ deg}$) and outside the bandgap (point C at $\lambda_C = 1502 \text{ nm}$, $\theta_C = 56.9 \text{ deg}$, D at $\lambda_D = 1500 \text{ nm}$, $\theta_D = 49.6 \text{ deg}$ and E at $\lambda_E = 1580 \text{ nm}$, $\theta_E = 53.5 \text{ deg}$).

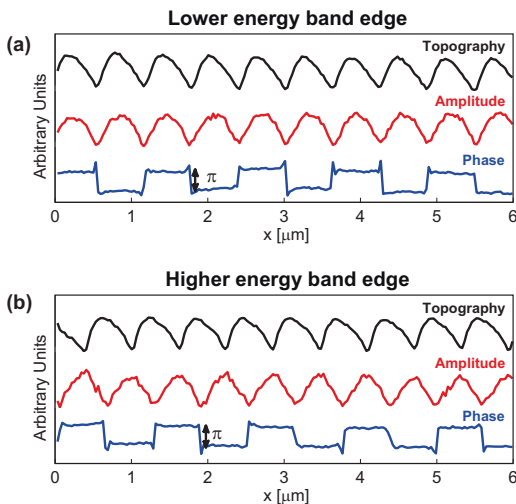


Figure 6.3: (Color online) Cross-sectional profiles of topography, amplitude, and phase at (a) the low-frequency (point A in Fig. 6.2 (b)) and (b) high-frequency (point B) band edges. The amplitude and phase are produced by TE-polarized illumination beam.

6.2 Field at the band edges

In order to maximize the BSW coupling strength, a collimated beam of about $500\ \mu\text{m}$ is used for illumination. Once BSW coupling is obtained, linear scans of $6\ \mu\text{m}$ on the corrugated multilayer surface are performed. Points A and B are considered first. In Fig. 6.3, we show the measurements at the low-frequency (A) and high-frequency (B) band edges, respectively. Although the sinusoidal topographic profile of the grating appears deformed because of the convolution with the SNOM tip [91], these peaks and grooves are well defined.

The measured near fields show an amplitude distribution having the same periodicity as the grating. Similarly to planar Bragg reflectors, the high-energy and low-energy fields have intensity maxima localized into the low- ϵ regions (air band) and high- ϵ regions (dielectric band) respectively [87]. In both cases, the phase shows a squared profile with a π -shift occurring at amplitude minima. This

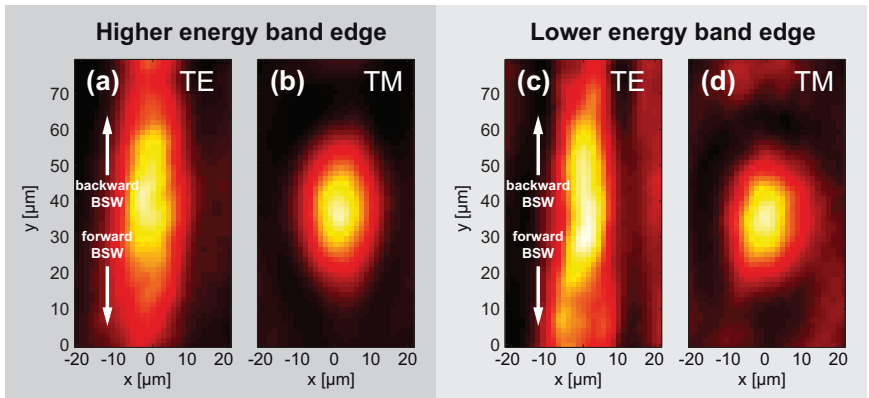


Figure 6.4: (Color online) Normalized intensity distribution of the near-field obtained at the band edges. (a) TE and (b) TM-polarized incident beam at point B, (c) TE and (d) TM-polarized at point A. The illumination beam provides a spot of size $20\ \mu\text{m}$.

is a typical effect of interference between two counterpropagating waves having equal amplitudes, i.e., the modes at the band edges are standing waves.

The two counterpropagating BSWs that are simultaneously coupled at band edges can be imaged directly by using a weakly focused illumination beam of about $20\ \mu\text{m}$. We illuminate at (λ_A, θ_A) and (λ_B, θ_B) corresponding to the points A and B in Fig. 6.2 (b) and detect both TE- and TM-polarized beams. Near-field measurements are performed over a scan region of $90 \times 90\ \mu\text{m}^2$, with a linear sampling interval of $\Delta x = 1.4\ \mu\text{m}$. Since the measured field is modulated with the grating period $\Lambda = 0.610\ \mu\text{m}$, we expect an aliasing effect. After proper Fourier filtering, we obtain the near-field intensity maps presented in Fig. 6.4. The TE-polarized near-field distributions show a strongly elongated distribution parallel to the illumination direction as compared to the TM-polarized field. This difference indicates BSW coupling. Nevertheless, while in the case of BSW coupling on flat multilayers the field is distributed in an asymmetric, comet-like pattern (see Fig. 5.6), in the case of BSW coupling at the band edges of a shallow grating, the distribution appears rather symmetric. This effect is due to the excitation of both forward and backward propagating BSWs, traveling away from

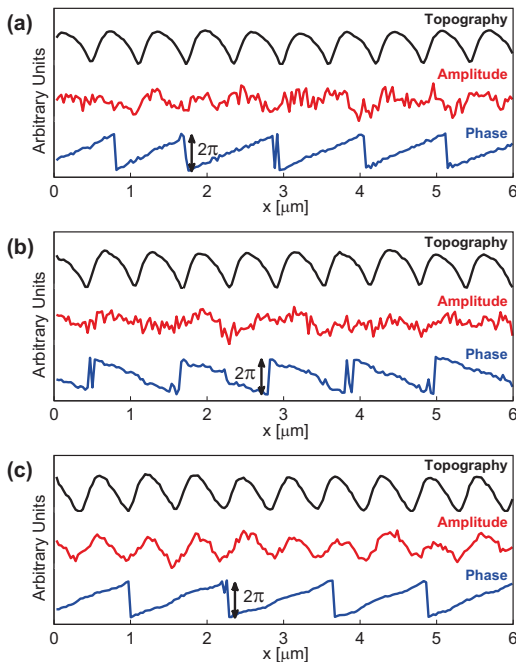


Figure 6.5: (Color online) Cross-sectional profiles of topography, amplitude, and phase at optical frequencies and incident angles corresponding to (a) point C, (b) point D, and (c) point E. As shown in Fig. 6.2 (b), the amplitude and phase are associated with an optical near-field produced by a TE-polarized illumination beam.

the central coupling region in opposite directions.

6.3 Field outside the band edges

Outside the bandgap region, we focus our attention on the points C-E of Fig. 6.2 (b). The results are shown in Fig. 6.5. In addition to the opening of a bandgap, the grating produces a branch folding of the BSW dispersion curve [78] that is particularly evident at wavelengths shorter than $\lambda = 1524$ nm (point B). The near-field amplitudes associated with points C and D show a constant spatial

distribution with very slight modulations almost comparable with the noise level of the whole detection process.

The phase distributions exhibit the typical saw-tooth profile associated with propagating waves with a well-defined propagation constant. The periodicity of the phases is almost the same, but the BSWs travel in opposite directions. In particular, the BSW at point C is characterized by a theoretically calculated positive propagation constant $\beta_C = 2\pi n_{BK7}/\lambda \cdot \sin(\theta_C)$, while the BSW at point D has a negative $\beta_D = 2\pi n_{BK7}/\lambda \cdot \sin(\theta_D) - 2\pi/\Lambda$, being coupled through the -1 order of the grating. Within this framework, BSWs lying on the right branch of the dispersion curve at frequencies higher than the bandgap are coupled to the 0 order of the grating, while BSWs on the left branch are efficiently coupled via the -1 order. At the band edges, the two branches merge and the counterpropagating waves are coupled simultaneously, resulting in the interference pattern shown in Fig. 6.3.

At frequencies lower than the bandgap, calculations show that only one branch of the dispersion curve is clearly visible. The BSW coupling efficiency via the -1 order of the grating is very small. At point E, we again detect a saw-tooth phase profile indicating a positive propagation constant. A slight modulation of the near-field amplitude is also found, as expected from rigorous calculations.

6.4 Conclusion

In this chapter, we have presented a near-field analysis of TE-polarized surface waves coupled into a periodically corrugated multilayer. We have demonstrated that a standing BSW defined by two counterpropagating modes having almost identical amplitudes is generated at the band edges of the grating. The field is mostly localized in the grating grooves and peaks at the high- and low-frequency photonic band edges, respectively. Away from the bandgap, the two counterpropagating BSWs can be selectively coupled via either the 0 or the -1 diffraction order of the grating. We also show that the SNOM technique can be usefully exploited to accurately characterize the optical response of subwavelength, shallow gratings when illuminated by surface waves.

The major content of this work has been published in [92].

7

Refraction of Bloch surface waves

Bloch Surface Waves (BSWs) are optical surface modes that may appear within the photonic bandgap of a truncated, periodic dielectric multilayer (see Chap. 5 and Refs. [59, 65, 75]). For a carefully designed multilayer, such BSWs manifest certain similarities with Surface Plasmon Polaritons (SPPs). Mainly, the optical field is highly confined close to the interface with the outer medium [68]. As SPPs, this characteristic leads to BSW sensing applications [72–74]. The surface confinement suggests that it may be useful to describe the propagation of BSWs with simple 2D laws. Such downscaling of a 3D model to a 2D one is not only of fundamental interest, but could facilitate the development of new and useful devices based on these structures.

SPP propagation through different kinds of interfaces was already extensively studied. Griesing *et al.* studied the propagation through dielectric micropisms deposited on a metal layer [93]. Zhang *et al.* looked at propagation through

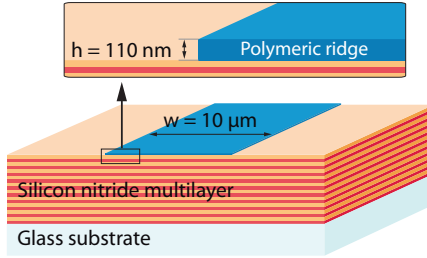


Figure 7.1: (Color online) Schematic view of the polymeric ridge deposited on the top interface of the silicon nitride multilayer (110 nm height, 10 μm width).

convex and concave lens-type dielectric structures laying on a metal layer [94]. Kitazawa *et al.* observed SPPs sustained at the interface between these Al and Au layers [95]. These experiments confirm that the transmission of the SPP through such interfaces manifests a refractive-type behavior governed by Snell’s law.

BSWs possess specific properties that differentiate them from SPPs. Sustained by a dielectric structure, they do not suffer from the losses due to metals also. The mode of a BSW extends into the multilayer more than the evanescent tail of the SPPs in the metallic layer(s). In this chapter, we report here on the use of the Multi-Heterodyne Scanning Near-Field Optical Microscope (MH-SNOM) to perform polarization- and phase-sensitive mapping of the propagating BSWs modes. The experimental results show that despite the differences between SPPs and BSWs, Snell’s law still accurately describes the propagation of BSWs through thin dielectric structures.

7.1 Experiment

The base structure is the silicon nitride multilayer described in Sec. 5.1. Polymeric ridges are then deposited on the top surface. The polymer (*Clariant GmbH, AZ5214E*) is used as a positive photoresist ($n_{pol} = 1.66$) for photolithography. Because of its viscosity (24.0 cSt at 25 °C), the minimal thickness reachable after photolithography is 1 μm . In order to reduce it even more, it has been diluted in

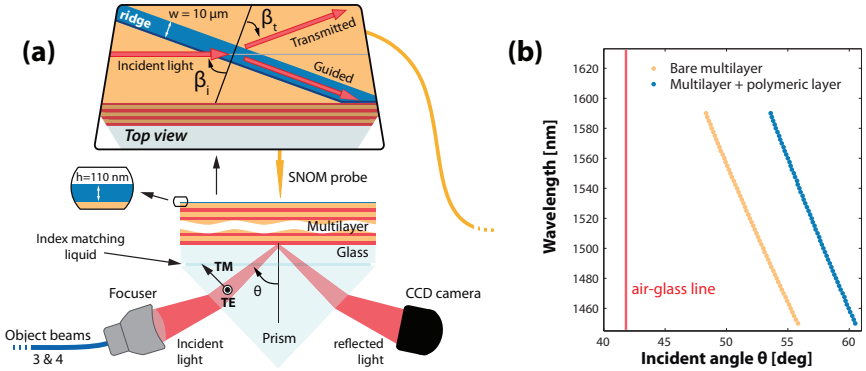


Figure 7.2: (Color online) (a) The sample is illuminated in the Kretschmann configuration with a focused beam. (b) Far-field measured dispersion curves of the bare multilayer (left) and the multilayer with an additional 110 nm polymer layer deposited on top (right).

a solvent (n-butyl acetate). The n-butyl acetate increases the dilution without interacting with the photosensitive molecules of the resist. A 1 to 6 volume ratio (photoresist to solvent) leads to a $\sim 110 \text{ nm}$ thick final layer at a spinning speed of 8000 rpm. This layer still shows a good adhesion to the silicon nitrite. In the present work, the waveguide width and height are $w = 10 \mu\text{m}$ and $h = 110 \text{ nm}$ respectively. A schematic drawing of the structures is shown in Fig. 7.1.

We use the MH-SNOM described in Chap. 4 to investigate the optical response of the structure. In Fig. 7.2 (a), the object channels are shaped with a focuser (*OZ Optics*) whose divergence of 4 deg creates a spot size of about $20 \mu\text{m}$ at the surface of the sample. The focuser is rotated so as to generate TE and TM-polarized fields with the channels 4 and 3 of Fig. 4.1 (Chap. 4), respectively. The BSWs are excited in the Kretschmann configuration with a BK7 prism ($n_p = 1.50$). The optical matching between the sample and the prism is ensured by an index matching liquid. The focuser is mounted on a goniometer which allows to change the coupling angle θ . The goniometric stage is placed on a 3-axis translation stage. An infrared-sensitive charge coupled device camera is mounted in a classical M-line configuration in order to catch the reflected light [81]. When a fraction of the TE-polarized incident light is coupled to the BSW, an absorption line is seen.

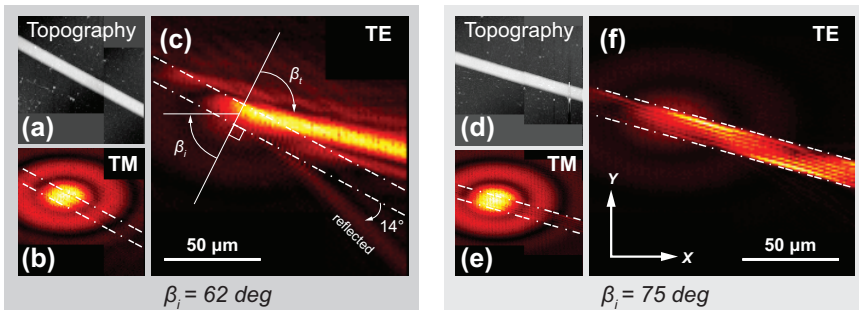


Figure 7.3: (Color online) The simultaneously obtained (a) topography, (b) TM and (c) TE-polarized near fields. The dashed lines correspond to the edges of the ridge. In the plane of the sample, the incident light arrives from the left and makes an angle β_i of 62 deg with respect to the ridge normal. The TE-light goes out of the polymeric ridge at a transmitted angle of β_t of 76 deg. In (d-f) are presented equivalent measurements for $\beta_i = 75$ deg. This angle exceeds the critical angle and the TE-polarized field is trapped in the ridge ($\lambda = 1555$ nm).

Typical absorption lines have been presented in Fig. 5.5.

Figure 7.2 (b) resumes the measured dispersion relations obtained in Fig. 5.11. The left curve corresponds to the dispersion curve of the bare multilayer. When covered with a 110 nm thick polymeric film, the right curve is shifted to higher wavelengths (right curve). These dispersion diagrams have been discussed in Sec. 5.6. In addition is represented the vertical air-glass line.

7.2 Refraction of Bloch surface waves: intensity measurements

Figures 7.3 (a-c) respectively show the topography, the TM and TE-polarized near fields as simultaneously obtained from the MH-SNOM ($\theta = 57.2$ deg, $\lambda = 1555$ nm). According to the dispersion curves in Fig. 7.2 (b) and the divergence of the illuminating beam, the BSW can only be excited in the polymer coated multilayer. The incident light arrives from the left and its projection onto the sample surface makes an angle β_i of 65 deg with respect to the normal to the

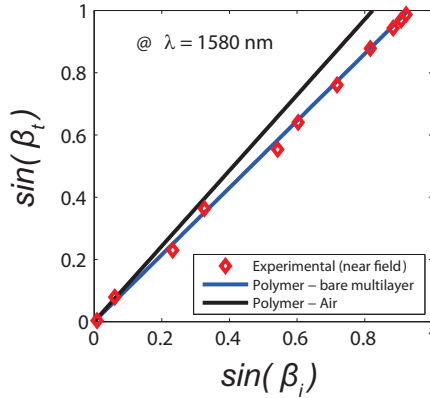


Figure 7.4: (Color online) Measured $\sin(\beta_t)$ for several values of $\sin(\beta_i)$ (red diamonds). In blue and black are the calculated refraction angles that should occur at a polymer-bare multilayer and polymer-air interface, respectively ($\lambda = 1580$ nm).

ridge. The dashed lines mark the edges of the ridge as obtained from the topography. The Airy pattern of the TM beam delimitates the incidence region. The TE-polarized light excites a BSW in the polymeric ridge and then leaks out at $\beta_t = 76$ deg, i.e., 14 deg with respect to the ridge. One can also find an equivalent angular contribution at 14 deg at the bottom of the ridge. It corresponds to that part of the BSW which is reflected at the upper interface and transmitted at the lower interface. In addition, by increasing β_i , we reach the critical angle β_{TIR} above which the BSW is trapped and guided in the ridge through total internal reflection (TIR). This situation is reached in the measurements of Figs. 7.3 (d-f) where $\beta_i = 75$ deg. The TE-polarized light is guided and its pattern suggests beatings between symmetric and asymmetric higher order modes [96]. Interestingly, a careful attention to the TM map reveals that few light is also guided. This behavior, as well as a detail modal analysis, will be addressed in Chap. 8

A series of measurements is then performed at different β_i ($\beta_i < \beta_{TIR}$, $\lambda = 1580$ nm). The red diamonds in Fig. 7.3 are the experimental values: $\sin \beta_t$ is plotted as a function of $\sin \beta_i$. The phase matching condition expressing the

BSW coupling from the polymer coated multilayer to the bare multilayer is

$$n_{BSW}^b \cdot \sin \beta_t = n_{BSW}^c \cdot \sin \beta_i \quad (7.1)$$

where n_{BSW}^b and n_{BSW}^c are the BSW effective indices in the bare and coated multilayer, respectively. They can be deduced from the far-field measurements through $n_{BSW}^b = n_p \sin \theta_b$ and $n_{BSW}^c = n_p \sin \theta_c$, where θ_r and θ_b are the coupling incident angles in the bare and coated multilayer, respectively (see Eq. 5.2). Using the values $\theta_b = 48.8$ deg and $\theta_c = 54.0$ deg obtained at $\lambda = 1580$ nm from Fig. 7.2 (b), the Eq. 7.1 gives the solid line (blue on-line) plotted in Fig. 7.2, along with the equivalent for coupling from the polymer coated multilayer to air (in black). The linear fitting of the experimental data provides a slope of 1.068 ($R^2 \simeq 0.99$), which corresponds to a discrepancy of less than 0.8% with respect to the slope of 1.076 given by Eq. 7.1.

As the width of the ridge is more than seven times the effective wavelength, in a simple model, we can assume that the $10 \mu\text{m}$ wide ridge behaves as a semi-infinite layer [97]. The observed phenomenon is hence a refraction of BSWs at an interface between two effective media: a bare dielectric multilayer and the polymer coated multilayer. The refractive behavior is well described by Snell's law.

7.3 Refraction of Bloch surface waves: phase measurements

The observed refractive behavior may be imaged in 2D by looking at the wavefronts on the surface of the sample. We set the incident angle θ to 53.6 deg and the wavelength to 1492 nm, and record the amplitude and phase maps. Under these conditions, the TE-polarized light is coupled to the BSW in the bare multilayer (see Fig. 7.2 (b)). Figure 7.5 (a) shows the effect of a ridge turned by $\beta_i = 58.5$ deg with respect to the propagative BSW. After a deflection to the left within the ridge, the BSW goes out of the structure parallel to the initial BSW. As the MH-SNOM is phase sensitive, the phase has been captured in small areas of $5 \times 10 \mu\text{m}$ before, within, and after the ridge: Figs. 7.5 (b-d) respectively. Consistent with the vertical propagation of the BSW before and after the ridge,

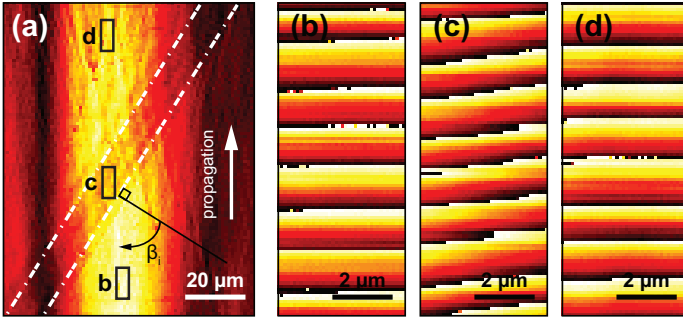


Figure 7.5: (Color online) (a) Transmission of the TE-polarized BSW through the ridge (dashed lines). The BSW propagates towards the top of the figure. (b), (c) and (d) show the phase profile wavefronts corresponding to the black rectangles labeled b, c and d in (a) ($\lambda = 1492 \text{ nm}$).

the wavefronts are flat in (b) and (d). In (c), the wavefronts are tilted by approximately 6 ± 2.8 deg with respect to the horizontal. Using Snell's law 7.1, the expected angle is 4.9 deg (with $\theta_b = 53.4$ deg and $\theta_c = 58.3$ deg from Fig. 7.2 (b)), which agrees reasonably well with the measured value. These results indicate that the in-plane orientation of the wavevectors across the interfaces satisfies the phase matching condition. As in classical textbooks, the latter assertion leads to Snell's law.

7.4 From near to far field

Because the probe collects the near field, there may be an unseen radiative component accompanying this phenomenon, i.e., some diffracted light corresponding to a transmission from the BSW in the coated multilayer to the air. In order to clarify this point, we turned off the shear-force feedback and made a series of scans at different heights above the sample surface. The angular misalignment between the multilayer surface and the x - y scanning plane is less than 0.5 deg. Figures 7.6 (a-e) corresponds to the measurements taken, respectively, at 300 nm, 567 nm, 833 nm, 1100 nm and 1366 nm above the surface of the ridge. In these maps, the BSW propagates from the bottom to the top. As can be seen, no other

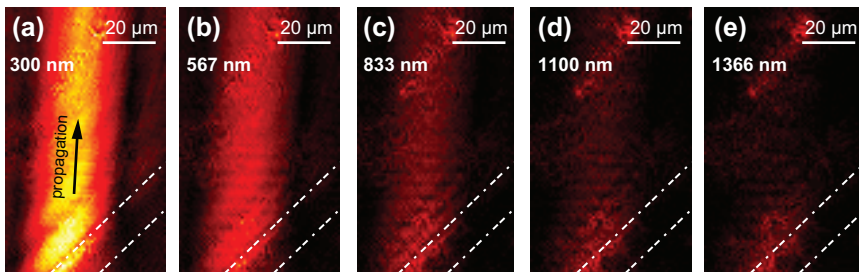


Figure 7.6: (Color online) TE-polarized amplitudes at different heights above the sample surface: (a) 300 nm, (b) 567 nm, (c) 833 nm, (d) 1100 nm and (e) 1366 nm. The dashed lines are the edges of the ridge.

relevant angular contribution appears. At 1366 nm, almost all of the signal intensity vanishes. The signal that is seen close to the ridge (dashed lines) corresponds to light scattered at the edge of the ridge. The scattering that occurs at the top of the figures is due to sample inhomogeneities. We therefore conclude that no significant radiative component exists due to the polymer-air interface.

7.5 Conclusion

In conclusion, we applied the MH-SNOM to perform a polarization and phase-resolved characterization of the BSW propagative modes in a multilayer dielectric structure. These results demonstrate that the only mechanism responsible for the transmission of a BSW through a thin dielectric relief is an energy transfer from the BSW mode of the bare multilayer to the BSW mode of the coated multilayer. At the interface, the deflection of the propagation direction is well described by the 2D Snell's law. A familiar law can therefore be used for the conception of thin optical dielectric structures involving BSWs.

The major content of this work has been published in [98].

8

Ultra-thin ridge waveguides for Bloch surface waves

In the last decade, a large number of issues related to the guiding of electromagnetic surface waves on a subwavelength scale have been addressed. Plasmonics, the branch of optics which manipulates Surface Plasmon Polaritons (SPPs), certainly remains the field that has attracted most of the attention [99]. Plasmonic waveguides involving different geometries have been proposed mainly for gaining strong (lateral) field confinement while maintaining low propagation losses. High-density packing of integrated photonic circuits principally motivates this research field [100]. In addition to guiding mechanisms based on ultra-thin metallic membranes [101], nanoparticle chains [102, 103], nanowires on dielectric substrates [104], dielectric nano-cylinders on metallic films [105], or V-grooves in metal surfaces [106], the most popular plasmonic waveguide configurations are constituted of Metal-Insulator-Metal (MIM) [107, 108] or Insulator-Metal-Insulator (IMI) [109] structures. Among the latter, we recall the so-called

Dielectric-Loaded Surface Plasmon Polariton Waveguides (DLSPWs) [110], in which a dielectric stripe is deposited onto a flat metallic film. For DLSPWs, the dielectric cladding should be thick enough to confine SPPs within the ridge, and therefore lowering the propagation losses and the sensitivity upon external perturbations. This latter feature makes the DLSPW not particularly well suited for sensing applications despite the millimeter range of propagation that can be reached. Indeed, biochemical sensing is better achieved in waveguiding arrangements where the field is confined in low refractive index materials such as water or air (e.g. slot waveguides [111]).

In the first part of this chapter, we demonstrate that an organic stripe of nanometric thickness can guide Bloch Surface Waves (BSWs) in a multilayer, while preserving the confinement of the field at the top interface. We use an ultra-thin polymeric ridge (thickness $< \lambda/10$) deposited on a silicon nitride multilayer sustaining TE-polarized BSWs in the near infrared. In the case where biosensing issues are of concern, the polymer might be replaced by any biochemically functional material suitable for molecular recognition. At the cost of a lateral confinement in the range of a few micrometers, guidance is experimentally demonstrated for ridge thicknesses down to approximately 110 nm with the actual low losses mainly associated with the leakage through the substrate. Rigorous computational analysis based on the Finite Element Method (FEM) suggests that even thinner organic ridges might be employed, while still preserving the BSW guidance.

In the second part of this chapter, we provide a detailed analysis of the modes propagating in such a BSW waveguide. We first demonstrate that the waveguide sustains three modes and that we are able, by tuning the wavelength and choosing the incident polarization, to selectively excite these modes. Then, the polarization characteristics of these modes are investigated.

Unlike near-field phase measurements which are routinely performed nowadays [7–10], polarization measurements in the near field still remain a challenging task [112, 113]. Although experiments involving the polarization contrast mechanism have been performed for a long time [13, 14], measuring the state of polarization itself implies knowledge of the electric vector field of light, i.e., two orthogonal amplitude components and the relative phase difference between them [114].

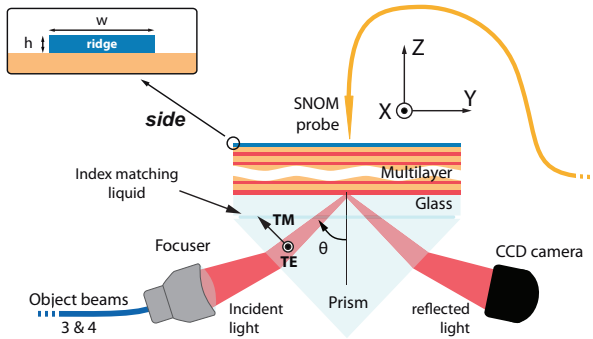


Figure 8.1: (Color online) The sample is illuminated in the Kretschmann configuration with a focused beam. The sample consists of a silicon nitride multilayer with an ultra-thin polymeric ridge deposited on top.

Recently, the amplitude components of the field have been measured [43, 45]. Measurements involving both the amplitude and phase of two orthogonal field components have also been carried out [115, 116]. In a beautiful experiment, Burrese *et al.* [44] integrally resolved the state of polarization of light within a 2D photonic crystal. However, all these techniques rely on a serial experimental process with control of the polarization in between each measurement.

Exploiting the capability of our Multi-Heterodyne Scanning Near-field Optical Microscope (MH-SNOM) to simultaneously measure the amplitude and phase of two arbitrary orthogonal components of paraxial (near) fields, we develop a technique for retrieving the field at the sample surface. The method relies on *a priori* information about the field distribution and on a simple numerical treatment of the experimental data. We apply the technique to the previously mentioned BSW waveguide using a simple energy consideration first tested on the calculated fields. We thus deduce the transverse and longitudinal components of the three modes. Finally, we measure the individual dispersion relations of each of the surface modes.

8.1 Experiment

The base structure is the silicon nitride multilayer described in Sec. 5.1. Polymeric ridges are then deposited on the top interface using the method discussed in Sec. 7.1 (Fig. 8.1, side view). In the first part of this chapter, the waveguiding potential of the ultra-thin ridge is presented with a polymeric ridge whose width and height are about $w = 3.5 \mu\text{m}$ and $h = 110 \text{ nm}$, respectively. Then, a detailed analysis of the guided modes is performed with a $4.5 \mu\text{m}$ wide and 140 nm thick ridge.

We use the Multi-Heterodyne Scanning Near-Field Optical Microscope (MH-SNOM) described in Chap. 4 to investigate the optical response of the structure. In Fig. 8.1, the object channels are shaped with a focuser (*OZ Optics*) whose divergence of 4 deg creates a spot size of approximately $20 \mu\text{m}$ at the surface of the sample. The focuser is rotated so as to generate TE and TM-polarized fields with the channels 4 and 3 of Fig. 4.1 (Chap. 4), respectively. The BSWs are excited in the Kretschmann configuration with a BK7 prism ($n_p = 1.50$). The optical matching between the sample and the prism is ensured by an index matching liquid. The focuser is mounted on a goniometer, which allows adjustment of the coupling angle θ . The goniometric stage is placed on a 3-axis translation stage. An infrared-sensitive charge coupled device (CCD) camera is mounted in a classical M-line configuration in order to observe the reflected light [81]. When a fraction of the TE-polarized incident light is coupled to the BSW, an absorption line is seen. Typical absorption line images are presented in Fig. 5.5.

8.2 Numerical method

In this section, we present the numerical method that is used in the following to calculate the spatial distribution of the modes sustained by the BSW waveguides. The simulations are performed with a commercial finite-element package (COM-SOL Multiphysics v.3.5a). The calculation domain is enclosed in a Perfectly Matched Layer (PML) to avoid reflections at the boundaries. A convergence analysis is conducted to ensure that the mode effective indices vary by less than 1%. It corresponds to a square computational domain with edges longer than

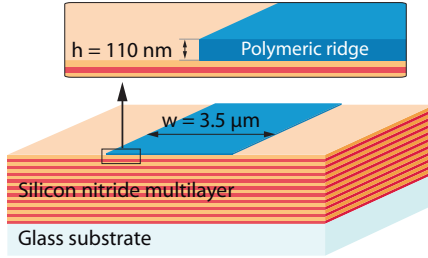


Figure 8.2: (Color online) Schematic view of the polymeric ridge deposited on the top interface of the silicon nitride multilayer (110 nm height, $3.5 \mu\text{m}$ width).

10λ , both in the x and z directions (see Fig. 8.1 for orientation). The thickness of the PML is chosen to be equal to $1.5 \cdot \lambda$. The effective index of the BSW sustained by the bare multilayer is extracted from Fig. 5.11 (Chap. 5) using the formula $\beta = n_{eff}2\pi/\lambda$ and used as an initial guess for rapid convergence. The simulations presented in this work were performed by Daniele Brunazzo at the Nanophotonics and Metrology Laboratory (Ecole Polytechnique Fédérale de Lausanne, Switzerland).

8.3 Guiding Bloch Surface Waves

8.3.1 Near-field demonstration

In Sec. 5.6 (Chap. 5), we have demonstrated that adding an ultra-thin polymeric coating (110 nm thick) to the silicon nitride multilayer shifts the dispersion curve of the BSW to higher propagation constants (at constant wavelength). In addition, we have shown that both dispersion relations are spectrally and angularly well separated. Such a separation, together with the remarkable narrowness of the BSW reflectance dips, provides the basic mechanism for obtaining good confinement of a BSW in the polymeric ridge.

Figure 8.2 shows the geometrical dimensions of the structure. It consists of a polymeric ridge (110 nm height and $3.5 \mu\text{m}$ width) deposited on the silicon nitride multilayer. The structure is approximately excited according to the BSW

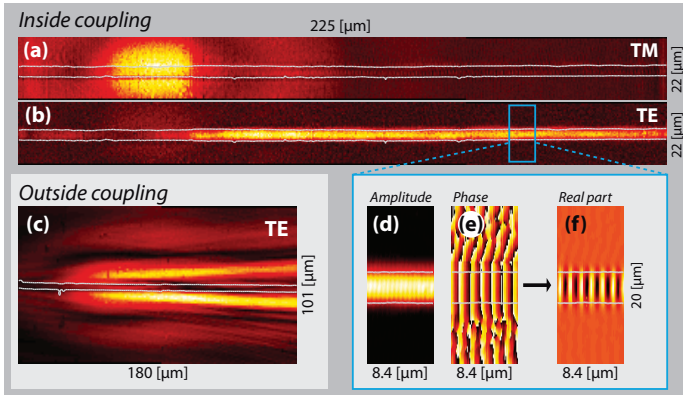


Figure 8.3: (Color online) (a-b) Near-field amplitude distributions for TM and TE-polarized illumination at $\lambda_{BSW} = 1580$ nm. (c) BSW amplitude distribution outside the polymeric ridge under TE-polarized illumination at $\lambda_{BSW} = 1470$ nm. The angle of incidence θ of the incident beam is kept fixed. Zoom: (d) amplitude, (e) phase and (f) real-part field distributions of the guided BSW far away from the incident region. The boundaries of the ridge as measured by the MH-SNOM shear-force are indicated by the grey lines.

far-field dispersion curve of the coated multilayer (see Fig. 5.11, Chap. 5). In Figs. 8.3 (a-b) are shown the TM and TE-polarized field amplitudes measured with the MH-SNOM at $\theta \simeq 54$ deg and $\lambda = 1580$ nm. These maps are obtained using Eqs. 4.9, Chap. 4. Specifically, Fig. 8.3 (a) shows the field amplitude distribution on the multilayer surface for TM-polarized illumination. The evanescent field mainly corresponds to the projection of an Airy-like pattern, as already seen in Chaps. 5, 6 and 7. More interestingly in Fig. 8.3 (b), the TE-polarized illumination generates a BSW guided along the ridge, showing a transverse distribution with a well defined central lobe and a very slow amplitude decrease in the propagation direction.

If the illumination wavelength is changed to $\lambda_{BSW} = 1470$ nm, while keeping the same incident angle, the field distribution shown in Fig. 8.3 (c) is measured for TE-polarized illumination. The BSW is excited only outside of the ridge. The typical comet-like pattern observed in the bare multilayer (see Sec. 5.4, Chap. 5) is

shadowed by the presence of the ridge. This effect is expected from the dispersion curves (Fig. 5.11) showing that BSWs cannot be coupled into the ridge at this wavelength and incidence angle.

A high-resolution scan of $8.4 \times 20 \mu\text{m}$ provides a detailed view of the spatial distribution of the guided BSW complex field. Figures 8.3 (d-f) show the measured amplitude, phase and the resulting real part of the field far away from the region of direct illumination. The wavefronts are flat and well confined within the ridge boundaries, as expected for the fundamental mode in a rectangular waveguide [117]. After performing a Fourier analysis (see Sec. 4.2.3, Chap. 4) on a line scan of $100 \mu\text{m}$ length, we find that the spatial modulation frequency of this fundamental mode is $f \simeq 0.736 \pm 0.01 \mu\text{m}^{-1}$, which is slightly smaller than the estimation from the measured dispersion curve in Fig. 5.11, i.e., $n_p \sin(\theta_{BSW})/\lambda = 0.768 \mu\text{m}^{-1}$. Substantial deviations of the guided BSW dispersion from the BSW dispersion curve on the flat, coated multilayer are expected, especially if higher order modes are considered or if the ridge width is appreciably reduced [97].

8.3.2 Fundamental mode analysis

Using the simulation tool presented in Sec. 8.2, calculations on the overall structure, including the semi-infinite glass substrate, the truncated multilayer and the polymeric ridge, are performed. Since the BSWs excited in the Kretschmann configuration are coupled back to the substrate and leak out into the prism, they cannot, in principle, be considered as pure modes of the structure. However, owing to the fact that the coupling is weak, they can be treated as leaky modes with real and imaginary parts of the effective index.

Results showing the dependence of the real part of the complex effective index n_{eff} of the guided BSW with respect to the waveguide geometrical parameters are presented in Fig. 8.4 (a). For relatively large ridge widths ($> 2 \mu\text{m}$), a weak dependence of n_{eff} on the ridge width is observed, as in low index contrast waveguides. On the other hand, the strong increase of n_{eff} as the ridge thickness increases indicates that the mode is increasingly confined within the polymeric region, until ultimately a conventional rectangular waveguide mode is obtained.

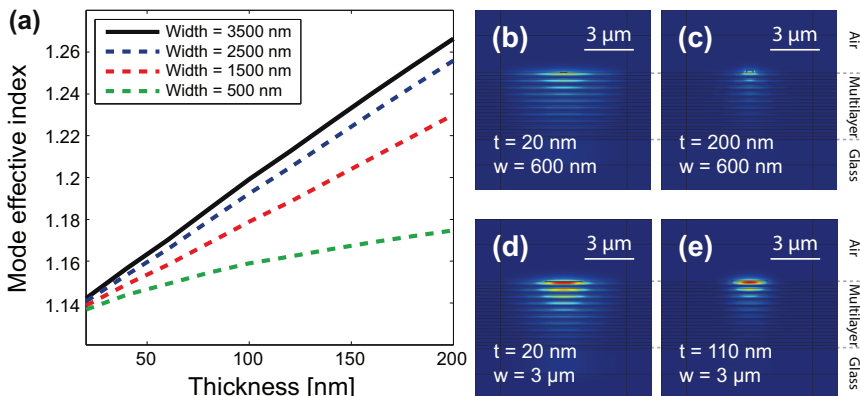


Figure 8.4: (Color online) (a) Effective refractive index of the fundamental guided BSW mode for different geometrical parameters (width w and thickness t) of the rectangular ridge; (b-e) guided BSW field distributions showing different degrees of confinement.

Figures 8.4 (b-e) show the transverse spatial distribution of the field within the structure for different thicknesses (t) and widths (w). For tiny ridges in Fig. 8.4 (b) ($w = 600$ nm, $t = 20$ nm), the lateral confinement is rather weak. Similarly to DLSPPWs, improvements in the lateral confinement are obtained while increasing the ridge thickness, as for the $w = 600$ nm, $t = 200$ nm ridge in Fig. 8.4 (c) where the field appears almost completely confined in the polymer. Wider ridges (on the micron scale) allow a strong binding of the guided BSW on the surface even for very small thicknesses (see the case of a $w = 3$ μm, $t = 20$ nm ridge in Fig. 8.4 (d)). The advantage of this configuration is that it provides a micrometric lateral confinement while essentially preserving the typical surface mode features required for sensing applications. Figure 8.4 (e) shows a $w = 3$ μm and $t = 110$ nm ridge whose dimensions are close to the experimentally investigated structure.

The ultra-thin dielectric ridge has thus been shown to efficiently guide BSWs at the surface of a multilayer. Although the preceding experimental work was carried out with the fundamental mode of the structure, BSW waveguides may also be multimodal. In the next section, we investigate the propagation and po-

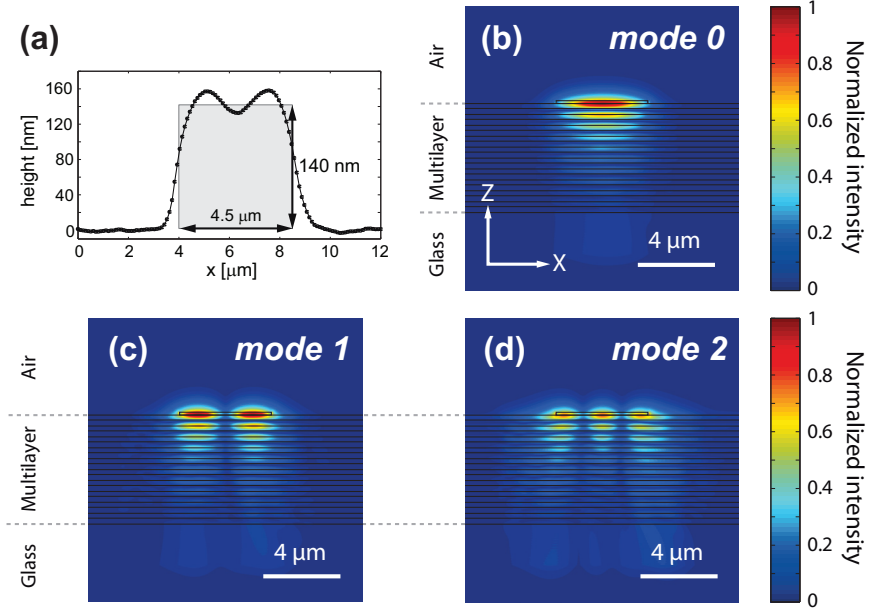


Figure 8.5: (Color online) (a) Topographic cross-section of the ridge measured with the shear-force feedback sensor (dotted line). The grey rectangle represents the approximated structure in the calculations (height $h = 140$ nm and width $w = 4.5 \mu\text{m}$). Calculated transverse intensity distributions of the (b) fundamental, (c) first and (d) second order modes ($\lambda = 1520$ nm).

larization properties of the surface modes sustained by a specific BSW waveguide.

8.4 Detailed analysis of waveguide modes

8.4.1 Sample and calculations

The structure characterized in this section consists of a polymeric ridge deposited on the silicon nitride multilayer, as described in Sec. 8.1. The dotted line in Fig. 8.5 (a) shows a topographical cross-section of the ridge measured with the

shear-force feedback sensor. The profile presents two bumps whose heights are about 155 nm with a groove at 130 nm in the center region. The mean width of the ridge is approximately $4.5 \mu\text{m}$.

For the calculations, we approximate the waveguide profile by a ridge whose width and height are $w = 4.5 \mu\text{m}$ and $h = 140 \text{ nm}$, respectively, as indicated by the grey rectangle in Fig. 8.5 (a). The refractive index used in the calculations is $n_{\text{pol}} = 1.625$. The calculations performed with the numerical tool discussed in Sec. 8.2 show that the structure sustains three modes confined at the outer interface of the guide (i.e. surface modes) and laterally confined by the polymeric ridge. Their transverse intensity distributions are displayed in Figs. 8.5 (b-d). The polarizations of the modes are parallel to the multilayer interfaces (plane (x, y) in Fig. 8.1) with a dominant transverse component in the x direction. The fundamental, first and second order modes are referred as *mode 0*, *mode 1* and *mode 2*, respectively. The modes 0 and 2 are symmetric, and the mode 1 is antisymmetric. In (b), the mode 0 presents one lobe laterally well confined into the ridge. In (c), the mode 1 shows two lobes that are still confined in the ridge, but whose lateral evanescent tails penetrate slightly further into the air surrounding the guide. Finally in (d), the mode 2 has three lobes with a greater penetration into the outer medium (air).

A detailed description involving the vectorial components of the calculated modes is provided in Sec. 8.4.3.3 in comparison with experimental measurements.

8.4.2 Selective excitation of the modes

First, we set the angle of incidence to $\theta = 56 \text{ deg}$ at $\lambda = 1538 \text{ nm}$. Figures 8.6 (a) and (b) respectively show the intensity distributions corresponding to TE and TM illumination, as simultaneously obtained with the MH-SNOM (Eqs. 4.9 of Chap. 4). The Airy patterns seen in both maps indicate the region of incidence, i.e., the zone where the focused incident light impinges on the sample. Both patterns demonstrate guidance within the polymeric ridge over more than $350 \mu\text{m}$, although weaker for the TM case. Up to $y \simeq 200 \mu\text{m}$, the TE distribution looks like the fundamental transverse mode of a classical dielectric ridge waveguide. The presence of a topographical defect (inset) at $y \simeq 200 \mu\text{m}$ considerably affects

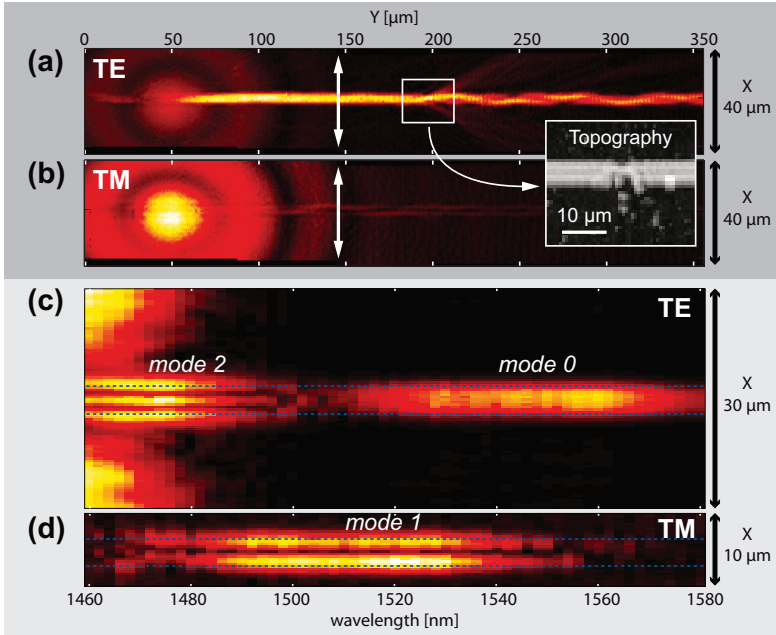


Figure 8.6: (Color online) (a) and (b), near-field intensities over the waveguide under TE and TM-polarized illuminations ($\lambda = 1538$ nm). The Airy patterns at left indicates the region where the incident light impinges on the sample surface. The inset shows the topographical defect responsible for the change in the propagating optical mode. (c) and (d) present (x, λ) plots for TE and TM-polarized illuminations, respectively. The x -axis follows the white arrows displayed in (a) and (b).

the spatial distribution of the field propagating beyond this point, although it is still guided. This behavior experimentally demonstrates the multimodal structure of the waveguide. Due to the defect, the energy which was mainly attributed to the fundamental mode is redistributed among the available modes. The pattern is asymmetric and suggests a beating between symmetric and antisymmetric modes [96]. This remark also holds true for the TM distribution.

Due to their dispersion, at a fixed angle of incidence θ , the transverse modes

are expected to be excited at different wavelengths. In order to demonstrate this effect and to characterize the modes, we set the SNOM tip in a fixed y position – the white arrows shown in Figs. 8.6 (a) and (b) – and scan a line across the waveguide along the x direction. The y position is chosen so as to lie outside the coupling region and to monitor the unperturbed surface modes of the structure. We then perform x scans while sweeping the wavelength in the interval between 1460 nm and 1580 nm.

The measurements are shown in Figs. 8.6 (c) and (d) for TE and TM polarizations, respectively. The scanning length is $30\ \mu\text{m}$ (only $10\ \mu\text{m}$ are displayed on the TM map). The ridge edges are marked with the dashed lines. Starting at longer wavelengths (1515 – 1580 nm), the TE map shows a one-lobe elongated spot centered on the ridge. Then the TM map reveals a two-lobe elongated spot at intermediate wavelengths (1480 – 1540 nm). Finally at shorter wavelengths (1460 – 1490 nm), the TE pattern presents a three-lobe spot inside the ridge. Since the scanning zone is about $100\ \mu\text{m}$ away from the incident region, these three spots are identified as mode 0 (one lobe), mode 1 (two lobes) and mode 2 (three lobes).

The intensity pattern of the mode 2 is surrounded by light corresponding to the BSW in the bare multilayer (BSW_{bare}), as demonstrated in Chap.5. The dispersion curve of the BSW_{bare} therefore partially overlaps the dispersion curve of the mode 2. No higher order modes are hence allowed within the waveguide, which is consistent with the calculations. Fortunately, from the incident region and up to the scanning zone, the BSW_{bare} propagates slightly away from the waveguide, making possible independent measurements on the mode 2. Also, the lateral mode spatial extent increases with the mode order: $3.8\ \mu\text{m}$, $4.7\ \mu\text{m}$ and $6.1\ \mu\text{m}$ (FWHM) for the modes 0, 1 and 2, respectively.

Due to its antisymmetry, it is expected that TE-polarized light cannot excite the mode 1. However, it may seem surprising that TM-polarized light couples to this mode, accounting for its in-plane polarization. A rigorous analysis of the coupling mechanism should in principle involve an overlap integral. We have performed additional calculations (not shown here) using a rigorous coupled-wave analysis (RCWA). It is indeed seen that only a TM-polarized plane wave excites the mode 1.

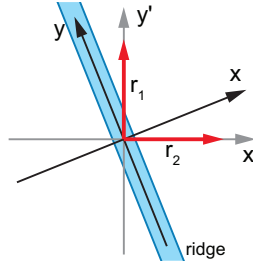


Figure 8.7: (Color online) At the detector plane, the reference frame (\hat{x}', \hat{y}') is fixed by the two linearly polarized references r_1 and r_2 of the multi-heterodyne interferometer. At the sample surface, the reference frame (\hat{x}, \hat{y}) is set according to the BSW waveguide.

By choosing the wavelength and the excitation polarization, we can therefore selectively excite the three modes sustained by the structure. In the next section, we show how the MH-SNOM can be fruitfully used to retrieve the vectorial components of each of the modes.

8.4.3 Vectorial components

8.4.3.1 Method

Figure 4.1 of Chap. 4 shows an overview of the MH-SNOM. In the current experiment, the object channels 3 and 4 correspond to the TM and TE-polarized illuminating beams. When collected by the SNOM probe, these fields are mixed with the orthogonal and linear reference channels 1 and 2. The fundamental issue in measuring the state of polarization with the MH-SNOM arises because of the unknown relative orientation between the reference beam and object beam polarizations. In our experiment, we must distinguish two distinct frames of reference. At the detector plane, the reference frame (\hat{x}', \hat{y}') is fixed by the two linearly polarized references of the multi-heterodyne interferometer. At the sample surface, the reference frame (\hat{x}, \hat{y}) is set according to the BSW waveguide. This situation is conceptually depicted in Fig. 8.7. The function that relates the expression of the electromagnetic field in these two bases is hereafter referred to

as the Polarization Transfer Matrix (PTM).

The existence of such a PTM has already been demonstrated for a dielectric probe, and for a paraxial (perpendicular to the probe axis) and linear input state of polarization (SOP) [35]. The paraxial condition is of importance. Indeed, if a field possesses a component along the probe axis, this components will be coupled to both orthogonally polarized propagating modes of the single-mode fiber [36]. In our experiment, the calculations show the electric field \mathbf{E} of the modes 0, 1 and 2 to be paraxial: \mathbf{E} is parallel to the multilayer interfaces and dominantly transverse (E_x). However, \mathbf{E} possesses a small longitudinal component E_y in the propagation direction y . The goal is hence to find E_x and E_y .

The calculations performed in Sec.8.4.1 show the electric field \mathbf{E} of the modes 0, 1 and 2 to be parallel to the multilayer interfaces and dominantly transverse (E_x). However, \mathbf{E} possesses a small longitudinal component E_y in the propagation direction y (see Fig. 8.1 for axis orientation). With respect to the probe axis, the electromagnetic fields of the modes are therefore paraxial. The motivation of this section is to find E_x and E_y .

As we are interested in the vectorial structure of the field, we compute the measured complex TE and TM vector fields, \mathbf{E}_{det}^{TE} and \mathbf{E}_{det}^{TM} , in $(\hat{\mathbf{x}}', \hat{\mathbf{y}}')$. With the experimental amplitudes and phases of Eqs. 4.7, these fields become

$$\begin{aligned} \mathbf{E}_{det}^{TE}(x, y) &= \begin{pmatrix} R_1^{TE}(x, y) \cdot e^{i \cdot \Phi_1^{TE}(x, y)} \\ R_2^{TE}(x, y) \cdot e^{i \cdot \Phi_2^{TE}(x, y)} \end{pmatrix} \\ \mathbf{E}_{det}^{TM}(x, y) &= \begin{pmatrix} R_1^{TM}(x, y) \cdot e^{i \cdot \Phi_1^{TM}(x, y)} \\ R_2^{TM}(x, y) \cdot e^{i \cdot \Phi_2^{TM}(x, y)} \end{pmatrix}. \end{aligned} \tag{8.1}$$

$R_{1,2}^{TE, TM}$ and $\Phi_{1,2}^{TE, TM}$ denote the amplitudes and phases measured by the lock-in amplifiers. The (x, y) dependence states that the fields are measured over the entire scanned map, i.e. at each position of the probe. The difficulty in linking the field at the detector plane to that at the sample surface arises because we don't know *a priori* the relative orientation at the detection plane of the TE field (resp. TM) with respect to the basis defined by the reference signals. Moreover, due to some birefringence that may occur within the probe [35] and in the optical path from the probe to the detector, the initial SOPs of the modes 0, 1 and 2 may reach the detector slightly altered.

Fundamentally, as there should be a PTM and as the TE field (resp. TM) is projected onto two orthogonal references – each signal being detected in amplitude and phase – all the information about the response of the sample is recorded. Since any SOP can be reached with a proper combination of a quarter-wave and a half-wave plate, \mathbf{J}_4 and \mathbf{J}_2 respectively, the field at the sample surface $\mathbf{E}_{sample}^{TE, TM}$ may be expressed as

$$\mathbf{E}_{sample}^{TE, TM}(x, y) = \mathbf{M} \cdot \mathbf{E}_{det}^{TE, TM}(x, y), \quad (8.2)$$

where $\mathbf{M} = \mathbf{R}(-\alpha_1)\mathbf{J}_4\mathbf{R}(\alpha_1) \cdot \mathbf{R}(-\alpha_2)\mathbf{J}_2\mathbf{R}(\alpha_2)$ is the PTM, and \mathbf{R} is the coordinate transform matrix [33]. The PTM is therefore modeled as an equivalent birefringent Jones matrix. The above equation represents the inverse problem of finding the field at the sample surface from the field at the detector. The physical propagation would indeed be represented by $\mathbf{E}_{det}^{TE, TM} = \mathbf{M}^{-1} \cdot \mathbf{E}_{sample}^{TE, TM}$. The issue is now to numerically find the angles α_1 and α_2 that lead to a separation of E_x and E_y .

To do so, an additional criterion is required. For any given values of (α_1, α_2) , the rule should indicate the degree to which $\mathbf{E}_{sample}^{TE, TM}(x, y)$ calculated with Eq. 8.2 matches the expected maps. Since the calculations show E_y to be small compared to E_x (ratio $\sim 1:5$), the criterion is to find the best pair (α_1, α_2) that minimize the intensity of one component of $\mathbf{E}_{sample}^{TE, TM}(x, y)$ while maximizing the other. We therefore seek for the best matrix \mathbf{M} that, applied point-by-point to $\mathbf{E}_{det}^{TE, TM}$, minimizes the intensity of one component over the entire map (integrated intensity over the entire map). This method has been first tested with the calculated fields. Starting from a projection of the field on two random and linear basis elements, E_x and E_y have been successfully retrieved.

The equivalent hardware procedure to the previous method consists of introducing a polarization controller after the probe. Consequently, E_x and E_y could be physically aligned with the reference beams $r1$ and $r2$, and therefore measured. However, the experimenter also needs *a priori* knowledge of the expected field for assessing the accuracy of the polarization controller alignment for each measurement. The experimental procedure therefore involves an alternation of measurements and polarization controller transformations. Since SNOM imaging is a scanning process, the collection of the individual SNOM images would be extremely time consuming.

8.4.3.2 Phase correction

The above method is correct provided that no phase drifts occur within the multi-heterodyne interferometer. In the presence of drifts, the relations 8.1 must be corrected. Typical phase drifts have been presented in Fig. 4.12, Chap. 4. As can be seen in this figure, the phase evolution is different from channel to channel. We can therefore conceptually see the phase drifts as being the sum of a global and differential delay.

A good understanding of the problem requires a return to the MH-SNOM fundamental phase relations of Tab. 3.1. With the notations used in this chapter, they are written as

$$\begin{aligned}
 \Phi_1^{TM} &= \varphi_{x'}^{TM} - \varphi_1 - \Psi_{31} \\
 \Phi_2^{TM} &= \varphi_{y'}^{TM} - \varphi_2 - \Psi_{32} \\
 \Phi_1^{TE} &= \varphi_{x'}^{TE} - \varphi_1 - \Psi_{41} \\
 \Phi_2^{TE} &= \varphi_{y'}^{TE} - \varphi_2 - \Psi_{42}.
 \end{aligned}
 \tag{8.3}$$

Let us introduce the additional lock-in phase measured between both reference beams

$$\Phi_{21} = \varphi_2 - \varphi_1 - \Psi_{21}.
 \tag{8.4}$$

We emphasize that the Ψ_{ij} , which represent the unknown phases arising from the generation of the lock-in electronic reference signals, are constant in time. Subtracting Φ_{21} from Φ_1^{TM} and Φ_1^{TE} , we obtain the following system of equations:

$$\begin{aligned}
 \Phi_1^{TM} - \Phi_{21} &= \varphi_{x'}^{TM} - \varphi_2 - \Psi_{31} + \Psi_{21} \\
 \Phi_2^{TM} &= \varphi_{y'}^{TM} - \varphi_2 - \Psi_{32} \\
 \Phi_1^{TE} - \Phi_{21} &= \varphi_{x'}^{TE} - \varphi_2 - \Psi_{41} + \Psi_{21} \\
 \Phi_2^{TE} &= \varphi_{y'}^{TE} - \varphi_2 - \Psi_{42}.
 \end{aligned}
 \tag{8.5}$$

Whereas the differential phase delay is compensated by subtracting Φ_{21} from Φ_1^{TM} and Φ_1^{TE} , the global phase delay affecting φ_2 is corrected by the FFT technique described in Sec. 4.2.3, Chap. 4. We indeed scan a high-resolution line along the propagation direction and find the spatial frequency of the propagating mode. The elapsed time for a single-line scan is short and the phases drifts

can be neglected. Phase maps corresponding to long duration scans can then be corrected accordingly.

Instead of the complex fields of Eqs. 8.1, the numerical method described above is therefore performed on the phase-corrected complex fields

$$\begin{aligned} \mathbf{E}_{det}^{TE}(x, y) &= \begin{pmatrix} R_1^{TE}(x, y) \cdot e^{i \cdot (\Phi_1^{TE}(x, y) - \Phi_{21}(x, y))} \\ R_2^{TE}(x, y) \cdot e^{i \cdot \Phi_2^{TE}(x, y)} \end{pmatrix} \\ \mathbf{E}_{det}^{TM}(x, y) &= \begin{pmatrix} R_1^{TM}(x, y) \cdot e^{i \cdot (\Phi_1^{TM}(x, y) - \Phi_{21}(x, y))} \\ R_2^{TM}(x, y) \cdot e^{i \cdot \Phi_2^{TM}(x, y)} \end{pmatrix}. \end{aligned} \quad (8.6)$$

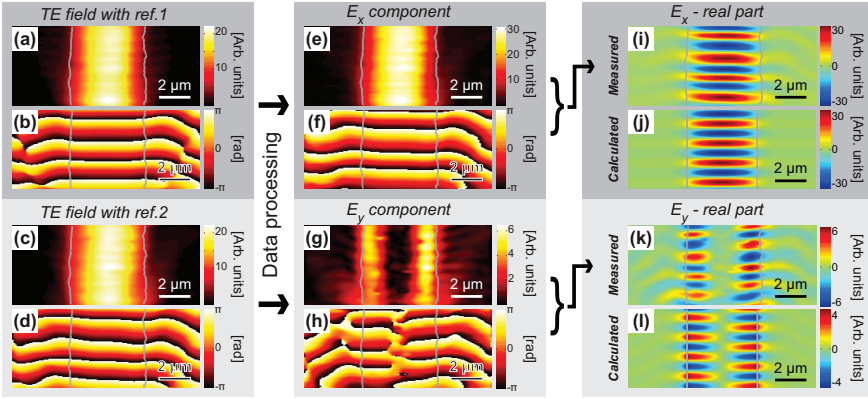
In the following, we show how these fields, combined with the method presented in the last section, allows the retrieval of the vectorial components of the modes propagating within the BSW waveguide.

8.4.3.3 Transverse and longitudinal components

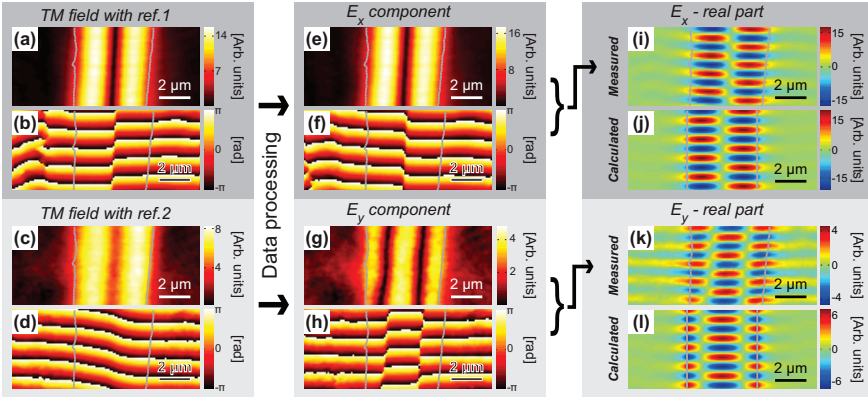
We apply step by step the numerical method developed in the previous section. As demonstrated in Sec. 8.4.2, by tuning the wavelength and choosing the excitation polarization, we can selectively excite each of the three modes sustained by the waveguide. The modes 0 and 2 are excited with TE-polarized light at $\lambda = 1568$ nm and $\lambda = 1478$ nm, respectively. The mode 1 is excited with TM-polarized light at $\lambda = 1514$ nm. The sub-figures (A-C) of Fig. 8.8 respectively show the results for the modes 0, 1 and 2.

In each sub-figure, (a-b) and (c-d) show the raw amplitudes and phases resulting from the interference of the object beam with the reference beams 1 and 2. We arbitrarily choose to minimize the field intensity corresponding to the component (c-d). The processed amplitude and the phase of this component are shown in (g-h), respectively. The component (a-b) is therefore automatically maximized and displayed in (e-f). In order to compare the measurements with the calculations, we compute, from the amplitudes and phases shown in (e-h), the real parts of E_x and E_y . (i-j) and (k-l) respectively show the measured and calculated real parts of E_x and E_y . The calculated maps are obtained as follows. From the computed transverse field distributions, we extract a line at 7 nm above the ridge interface. Then, we make it propagate with the effective index obtained from the

(A) Mode 0



(B) Mode 1



(C) Mode 2

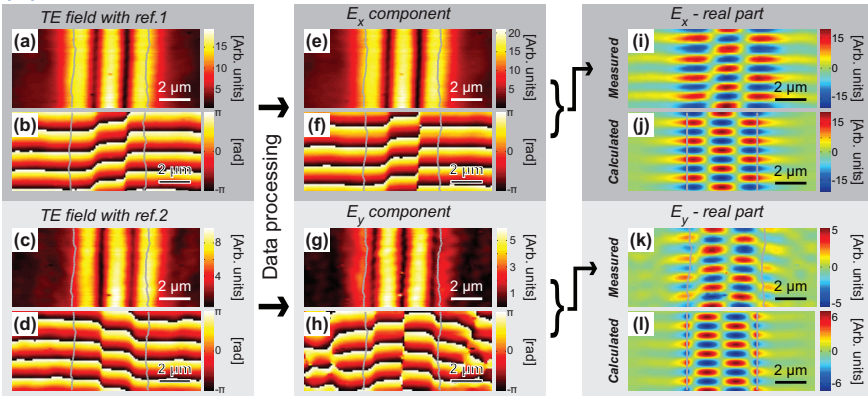


Figure 8.8: (Color online) (A): (a-b) and (c-d) Amplitudes and phases of the mode 0 projected onto the two reference beams 1 and 2. (e-f) and (g-h) Respective amplitudes and phases of E_x and E_y retrieved after numerical data processing, (i-j) and (k-l) Measured and calculated real parts of E_x and E_y ($\lambda = 1568 \text{ nm}$). In (B) and (C), the equivalent for mode 1 ($\lambda = 1514 \text{ nm}$) and mode 2 ($\lambda = 1478 \text{ nm}$).

same simulation (mode 0: $n_{eff} = 1.256$ at $\lambda = 1568$ nm, mode 1: $n_{eff} = 1.274$ at $\lambda = 1514$ nm, mode 2: $n_{eff} = 1.273$ at $\lambda = 1478$ nm). For the sake of clarity, a global phase delay is added to the calculated real parts. The gray lines represent the edges of the ridge as provided by the shear-force topography.

For each of the modes, the measured real parts of the transverse and longitudinal components are found in good agreement with the calculated ones. First, their spatial distributions almost have the same extent. Secondly, the amplitude ratios $|E_x|/|E_y|$ of the measured and simulated values are satisfactory close: 5 versus 7.5 for the mode 0, 3.8 versus 4 for the mode 1, and 3.6 versus 2.9 for the mode 2. Third, the symmetry of each measured component is retrieved. Because E_x is stronger – and so defines the mode symmetry – we verify that the modes 0 and 2 are symmetric whereas the mode 1 is antisymmetric.

Comparing the results of the three modes, we can draw two overall conclusions. First, the measured and calculated modes shows slightly different periodicities. This may be due either to a waveguide cross-section that departs from the ideal rectangular shape of the simulated structure (see Fig. 8.5 (a)), or to a possible deviation between the real and theoretical effective indices of the polymer. Furthermore, the sample has a slightly inhomogeneous topography leading to some local fluctuations of the effective indices.

Secondly, in this particular experiment, the relative phase difference between E_x and E_y is not measured. The apparent relative phase differences appearing in Figs. 8.8 (A-C) (i) and (k) arise because of the arbitrary optical path differences within the multi-heterodyne interferometer. This can be solved in the future by a proper calibration of the system using a field of known polarization, or by implementing a two-detector detection system discussed in Sec. 3.3.2, Chap. 3.

8.4.4 Dispersion relations of the modes

From the amplitude and phase of an optical signal, one can compute the complex field [48]. Considering lines in the y direction (propagation direction), the four amplitudes and phases of Eqs. 4.7 (Chap. 4) leads to the four scalar complex

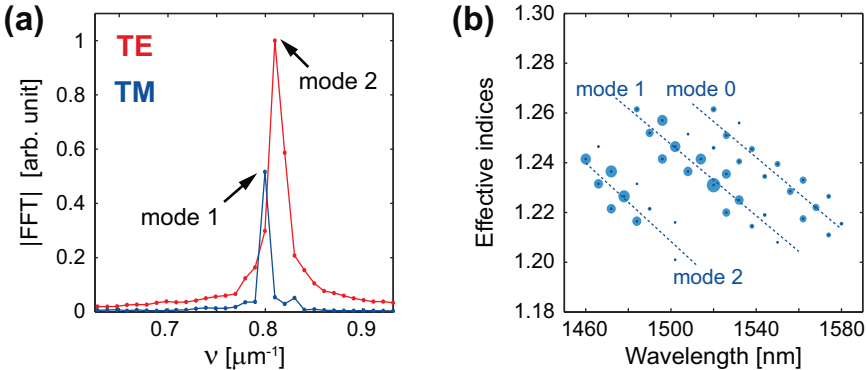


Figure 8.9: (Color online) (a) A typical Fourier spectrum obtained for both TE- and TM-polarized fields along the BSW propagation direction ($\lambda = 1530 \text{ nm}$). (b) Repartition of the measured effective indices over the whole wavelength range. The blue disk diameters account for the peak occurrences. The dashed lines are the fitted curves.

fields

$$\begin{aligned}
 V_1^{TE}(y) &= R_1^{TE}(y) \cdot \exp[i\Phi_1^{TE}(y)] \\
 V_2^{TE}(y) &= R_2^{TE}(y) \cdot \exp[i\Phi_2^{TE}(y)] \\
 V_1^{TM}(y) &= R_1^{TM}(y) \cdot \exp[i\Phi_1^{TM}(y)] \\
 V_2^{TM}(y) &= R_2^{TM}(y) \cdot \exp[i\Phi_2^{TM}(y)].
 \end{aligned} \tag{8.7}$$

As seen in Sec. 4.2.3, a Fourier analysis of these complex fields provides the k_y components of the in-plane wavevectors of the optical field. For guided or bound modes, the propagation constants can be deduced [9, 49, 50, 118], and the effective indices determined through the relation $n_{eff} = \lambda k_y / (2\pi)$. As the resolution in the Fourier space is inversely proportional to the scanning length L , we use the entire travel range of the piezo actuator ($L = 100 \mu\text{m}$). This condition leads to a theoretical wavevector resolution of $dk_y = 2\pi/L = 6.3 \cdot 10^4 \text{ m}^{-1}$, which in this experiment corresponds to a low effective index resolution of $dn_{eff} = \lambda dk_y / (2\pi) \simeq 0.015$. This poor resolution will be overcome by a statistical treatment of the data acquired at different wavelengths.

At a given wavelength, because the transverse field distributions of the modes

are different, six high-resolution y -lines are acquired on both sides of the ridge. For each line, the FFT spectra are computed on the four complex fields of Eqs. 8.7. The relevant peaks are identified and their effective indices calculated. Two representative TE and TM spectra are shown in Fig. 8.9 (a) ($\lambda = 1530$ nm). At this wavelength, the analysis performed on Figs. 8.6 (c) and (d) allows identification of the dominant TE and TM peaks with the modes 0 and 1 respectively. These peaks are only separated by dk_y , which highlights the low effective index resolution.

This procedure is repeated over the entire wavelength range (1460 – 1580 nm) in steps of 6 nm. The measured effective indices are indicated by the blue disks in Fig. 8.9 (b). The disk diameters account for the peak occurrences: six scanning lines with four complex fields leads to 24 spectra per wavelength. Three regions can be distinguished: one at larger wavelengths (1520 – 1580 nm) and higher n_{eff} , an intermediate zone (1484 – 1552 nm) with intermediate n_{eff} , and a region at shorter wavelengths (1460 – 1502 nm) and lower n_{eff} . The wavelength ranges covered by the different modes (see Figs. 8.6 (c) and (d)) and the fact that lower order modes have higher n_{eff} identify these region with the modes 0, 1 and 2 respectively. Linear curve fits accounting for the weights (occurrences) of the experimental values are plotted with the dashed lines.

In Fig. 8.10, the fitted curves are reported in a dispersion diagram. The dispersion curves of the modes 0, 1 and 2 are respectively displayed in red, green and blue. In addition the measured dispersion curves of the bare multilayer as obtained from far-field measurements (see Sec. 5.6), and the calculated dispersion curve of the multilayer coated with a 140 nm thick polymeric layer ($n_{pol} = 1.625$) are reported. As expected, the dispersion curves of the ridge waveguide modes lie between the bare and coated ones. An increase in the mode order decreases the field fraction confined in the ridge region and the mode effective index therefore decreases, leading to the observed blue shifts of the higher order modes.

Despite the low resolution in terms of the effective indices, this experiment shows that accounting for the tunability of the system, the individual dispersion curves of the three modes sustained by the BSW waveguide can be measured.

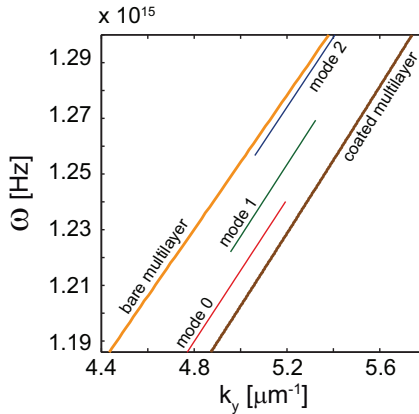


Figure 8.10: (Color online) Dispersion curves of the three modes. In addition the dispersion relations of the bare multilayer and coated multilayer (with a 140 nm thick polymeric layer) are reported.

8.5 Conclusion

We have demonstrated the possibility of guiding BSW by patterning a multilayer sustaining BSWs with dielectric stripes of nanometric thicknesses. Contrary to DLSPWs in Insulator-Metal-Insulator waveguides, guided BSW losses are small even for very thin dielectric ridges because of the all-dielectric structure. This characteristic opens interesting possibilities for sensing applications in which thin, patterned organic functional films provide a field confinement on the chemically active area of the sensor.

In the second part of this chapter, we have focused our attention on a particular BSW waveguide whose width and height were $4.5 \mu\text{m}$ and 140 nm , respectively. We have experimentally demonstrated that this BSW waveguide sustains only three modes, and that we were able to selectively excite them by tuning the wavelength and choosing the excitation polarization. The individual dispersion relations of the modes have been measured and we have shown that they lie, as expected, between the dispersion curves of the bare and coated (140 nm thick polymeric film) multilayer. Exploiting the ability of the MH-SNOM to simulta-

neously detect in amplitude and phase two arbitrary orthogonal components of the near field, we were able to solve the inverse problem of retrieving the field components of the modes at the sample surface from the fields at the detector plane. This task has been achieved through a simple *a priori* energy consideration; the calculations indeed show that the longitudinal field component is much weaker than the transverse one. The individual transverse and longitudinal components of each of the modes have hence been measured, and a good agreement with the simulation results was found. This work provides new insights on the propagation of guided BSWs on ultra-thin guiding structures that might be fruitfully exploited in variety of applications in the domain of low-dimensional optics. Although we have not directly measured the relative phase between the mode components, this task could be achieved in the future with a preliminary calibration of the multi-heterodyne interferometer or by implementing a two-detector detection system as described in Sec. 3.3.2, Chap. 3, allowing in this way the integral measurement of the states of polarization.

The method developed here for separating the vectorial field components ultimately relies on a simultaneous detection in amplitude and phase of two arbitrary orthogonal field components, followed by a post-processing of the data based on an *a priori* knowledge of the field distribution. By refining the optimization criterion, this method can be applied to a broad variety of near-field phenomena including waveguide structures, cavities, resonators, etc. To a certain extent, we can even think of applying this technique without any preliminary information on the desired field, but by processing the experimental data with mathematical tools. For instance, we can imagine using the symmetries of the topography to analyze the optical information, or to find transformations that maximize the contrast between intensity maps.

To this end, many of the current standard heterodyne SNOMs may significantly increase their measuring power by adding a second orthogonal reference, provide that their electronics allows the acquisition of supplementary signals.

The major content of this work has been submitted in [119,120]. This chapter concludes the series of chapters dedicated to BSW structures.

9

Asymmetrical excitation of surface plasmon polaritons on a blazed grating

The excitation of Surface Plasmon Polaritons (SPPs) is a crucial issue for many nanophotonic applications such as highly integrated photonic circuits [54]. As one of several alternatives for the excitation of SPPs, diffraction gratings have been widely used to couple incident light to SPPs on metal films [121]. Directional excitation can be achieved, for example, by oblique incidence of light on the grating [122,123], via the phase matching of one evanescent diffraction order to a SPP mode. The oblique incidence condition is not always possible in integrated optics applications and therefore, a simple and more flexible coupling mechanism that allows unidirectional SPP excitation under normal incidence is of interest.

Bonod *et al.* proposed using slanted lamellar or sinusoidal gratings to launch unidirectional propagating SPPs [124]. The blazing effect indeed leads to ex-

citation of the $\pm 1^{\text{st}}$ evanescent orders with highly asymmetrical strength. By phase matching the momentum of the $\pm 1^{\text{st}}$ evanescent orders with the in-plane plasmon wave vector, the incident energy can be asymmetrically coupled to the counterpropagating SPPs along the periodic direction.

The canonical structure generating an asymmetry between positive and negative orders is the classical one-dimensional (1D) blazed grating [125]. However, the fabrication of such structures is more difficult than that of binary structures due to their slanted profiles. The asymmetrical profiles have to be manufactured by, e.g., direct laser-beam or ion-beam milling, a series of photolithographic processes that approximate the continuous surface profile by a staircase multilevel structure, or inclined-angle reactive ion-beam etching with a binary grating mask. In addition to the complexity of the fabrication process (e.g., several masks have to be used to create a multilevel profile), the control of depth variations within a period, which is crucial for achieving the blazing effect, is rather difficult. In electron-beam lithography (EBL), controlling the in-plane dimensions of a binary structure is much easier than modulating its depth. Based on this consideration, Kleemann *et al.* [126] proposed a novel type of binary-blazed gratings, called the Blazed Area-Coded Effective-Medium Structures (BLACES), to achieve the blazing effect through an effective index variation in a single layer by modulating the local filling factor of a binary two-dimensional (2D) grating pattern. Unlike the 1D slanted gratings or conventional binary-blazed gratings with high-aspect-ratio ridges or pillars [127], the BLACES have more reasonable dimensions and are easier to fabricate with, e.g., standard EBL [128].

In classical diffractive optics, conventional binary-blazed gratings use a subwavelength sampling period along the grating period. In contrast, BLACES use a subwavelength sampling period perpendicular to the grating period [126]. Dedicated to SPP coupling, the metallic BLACES that will be characterized in the following work has the particularity of being subwavelength in both directions. In the transverse direction, the period is much smaller than the wavelength. All the diffraction orders, except for the zeroth order, are therefore evanescent. In the blaze direction, the period is chosen slightly subwavelength so as to excite SPPs through the phase matching condition.

In this chapter, the asymmetric excitation of SPPs in BLACES will be directly

investigated in the near field with the Multi-Heterodyne Scanning Near-Field Optical Microscope (MH-SNOM). In particular, it will be seen that due to the short propagation length of the SPPs, the quantitative assessment of the blazing effect in the spatial domain is difficult. In contrast, the Fourier analysis of the complex optical near fields (see Sec. 4.2.3) will prove to be much more appropriate.

9.1 Principle

Surface plasmons are electron oscillations near a metal surface stemming from the broken translational invariance in the direction normal to the surface. A combined excitation consisting of a surface plasmon and a photon is called a SPP [53]. The dispersion relation of a SPP on a smooth metal surface is given by [121]

$$k_{SPP} = k_0 \sqrt{\frac{\varepsilon_{\text{met}} \varepsilon_{\text{die}}}{\varepsilon_{\text{met}} + \varepsilon_{\text{die}}}}, \quad (9.1)$$

where k_{SPP} is the modulus of the SPP wave vector \mathbf{k}_{SPP} , $k_0 = 2\pi/\lambda_0$ is the light wave number in vacuum, and ε_{met} and ε_{die} are the permittivities of the metal and the adjacent dielectric, respectively.

Since the SPP dispersion curve always lies on the right side of the dielectric light line without crossing it (see, for example, Ref. [121]), a SPP cannot couple to a radiative mode and, conversely, cannot be directly excited by light propagating in the dielectric. However, if a grating with period d is introduced, momentum conservation can be satisfied through the m^{th} evanescent diffraction order by [121]

$$\mathbf{k}_{SPP} = \mathbf{k}_{\parallel}^{\text{inc}} + mK\hat{\mathbf{x}}, \quad (9.2)$$

where $\mathbf{k}_{\parallel}^{\text{inc}}$ is the in-plane wave vector of the incident light and $K = 2\pi/d$. Specifically, if the grating is mounted under normal incidence (so that $\mathbf{k}_{\parallel}^{\text{inc}} = 0$) and the SPP is to be excited by the $\pm 1^{\text{st}}$ orders, Eq. 9.2 is reduced to

$$\mathbf{k}_{SPP} = \pm K\hat{\mathbf{x}}. \quad (9.3)$$

Therefore, according to Eqs. 9.1 and 9.3, we can estimate, e.g., the excitation light wavelength λ_0 , the SPP wavelength $\Lambda_{SPP} = 2\pi/k_{SPP}$ on the metal surface, or the grating period d , to obtain a preliminary guess of the parameters for a specific design.

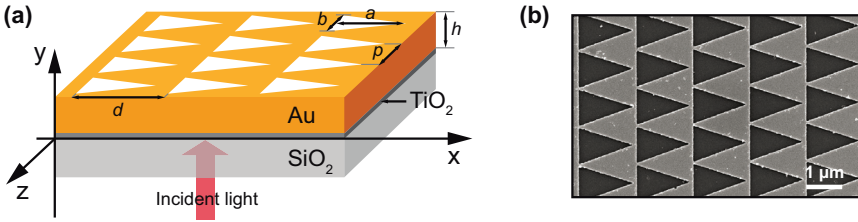


Figure 9.1: (Color online) (a) Schematic view of the gold BLACES grating whose geometrical parameters are approximately $d = 1520$ nm, $p = 1050$ nm, $a = 1360$ nm, $b = 955$ nm, and $h = 40$ nm; (b) SEM image of the grating.

By blazing, the diffraction efficiencies of the $\pm 1^{\text{st}}$ transmitted orders (in the x direction in Fig. 9.1) can be highly asymmetric, i.e., most of the diffracted light is redirected into a single order. In such circumstances, if the grating period d decreases so that the $\pm 1^{\text{st}}$ orders turn from propagating to evanescent and match the SPP momentum via Eq. 9.3, the excited SPP modes propagating in $+x$ and $-x$ directions could have asymmetric strengths as the incident energy is transferred to the SPPs via the $\pm 1^{\text{st}}$ orders. This is the fundamental principle for the asymmetrical excitation of SPPs on blazed gratings.

9.2 Sample design and fabrication

A schematic view of the BLACES is presented in Fig. 9.1 (a). It consists of a planar gold film perforated with an array of isosceles triangular holes deposited on a substrate. The structural parameters are approximately $d = 1520$ nm, $p = 1050$ nm, $a = 1360$ nm, $b = 955$ nm, and $h = 40$ nm. For a discussion of how these parameters have been numerically optimized, we refer to Ref. [118]. Since the transverse period p is much smaller than the incident wavelength λ_0 and the blaze period d , all diffraction orders, except for the zeroth order, are evanescent in the z direction. Therefore, the diffraction spectrum of this 2D grating is similar to that of a 1D grating, with the blazing effect induced by the local effective refractive index modulation within each period along the x direction [126, 128].

The BLACES is fabricated by standard electron-beam lithography (EBL) and

lift-off techniques. A fused-silica substrate was first deposited with a 5 nm thick TiO_2 adhesion layer by thermal evaporation. Then a 120 nm thick polymethyl methacrylate electron-beam resist layer was spin coated, which was covered by a 20 nm thick conductive copper layer. The resist was patterned by a high-resolution electron-beam writer (*Vistec, Model EBPG5000+ES*). After the copper layer was removed and the resist developed, the sample was coated with a 40 nm thick gold layer by thermal evaporation. The remaining resist and thus the gold on top of it were removed with acetone, and the sample was rinsed with isopropanol. A scanning electron microscope (SEM) image of the fabricated sample is shown in Fig. 9.2 (b). The sample fabrication was carried out by Janne Laukkanen and Xiangfeng Meng at the Department of Physics and Mathematics (University of Joensuu, Finland) [118].

We should note that the sample design is not ideal due to some practical restrictions. First, the illumination wavelength λ_0 has to be set around 1530 nm to match the light source of the MH-SNOM although the SPP excitation is less efficient in the infrared due to the increased metal conductivity [129, 130]. Moreover, because the probe can only access the air-metal interface and because the illumination should be at normal incidence, the air-metal interface can only be characterized with illumination from the back side of the sample. The back side illumination is also disadvantageous for efficient asymmetrical excitation of SPPs on the front interface of the perforated metal film. Even though we have these limitations, it is still meaningful to characterize the effect (on the air-metal interface at the *transmission* side hereafter) experimentally and compare it with theoretical predictions. Detailed calculations concerning the optimization of the sample were performed by Benfeng Bai and may be found in [118].

9.3 Experiment

We use the Multi-Heterodyne Scanning Near-Field Optical Microscope (MH-SNOM) described in Chap. 4 to investigate the optical response of the sample. The illumination system is shown in Fig. 9.2. The two object channels 3 and 4 of Fig. 4.1 (Chap. 4) enter a focuser (*OZ Optics*) that creates a spot whose diameter is about $20\ \mu\text{m}$ at the sample surface. The focuser is rotated so as to generate

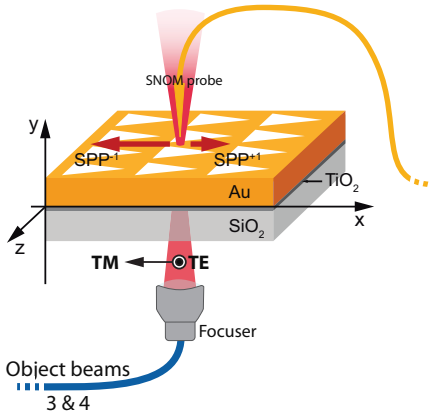


Figure 9.2: (Color online) Schematic view of the illumination system. $SPP^{\pm 1}$ refer to the two SPP modes asymmetrically excited by the $\pm 1^{st}$ evanescent orders at normal incidence (the length of the arrows show the relative strength).

TM and TE-polarized beams (x and z directions respectively). The TM and TE polarizations respectively correspond to the channels 3 and 4, i.e., the 30 kHz and 50 kHz heterodyne signals (resp. 50 kHz and 90 kHz) constitute the response of the sample under TM (resp. TE) illumination. By means of a tilt stage acting on the sample, the incident light is brought to normal incidence with an accuracy of ± 2 deg. As the focuser divergence is $\delta \simeq 4$ deg, normal incidence is necessarily reached by a particular component of the illumination angular spectrum.

As will be seen throughout this chapter, one significant difficulty in this experiment lies in the fact that the 0^{th} order of the grating is intense. It is therefore difficult to observe weak phenomena in the region of incidence.

9.4 Analysis in the spatial domain

Since the sample is designed to work close to $\lambda = 1530$ nm, a preliminary $100 \times 100 \mu\text{m}$ scan is performed at this wavelength. Figures 9.3 (a) and (b) respectively show the optical near-field amplitude (square root of Eq. 4.9) collected at the

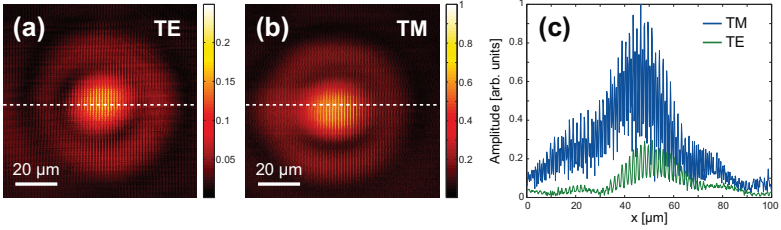


Figure 9.3: (Color online) (a-b) Amplitudes corresponding to the optical response of the sample under TE and TM-polarized illumination, respectively ($\lambda = 1530$ nm). (c) Amplitude cross-profile along the white dashed lines crossing (a) and (b).

sample surface under TE and TM-polarized illumination. These two maps are normalized with respect to the maximum amplitude. The TM field reveals a small asymmetry on the left, as if a weak signal propagates away from the central spot. To better appreciate this phenomenon, a cross-sectional profile along the white dashed lines is extracted and displayed in Fig. 9.3 (c). In addition to the large amplitude variations originating from the alternating series of metal islands and apertures, the cross-section reveals an intensity enhancement of about 16 (4 in amplitude) of the TM polarization with respect to the TE polarization. The $5 \mu\text{m}$ shift to the left of the TM spot with respect to the TE spot seems to indicate a favored SPP propagation in the $-x$ direction.

In order to quantitatively compare the strengths of the two counterpropagating excited SPP waves, we performed a one-dimensional scan across the central spot (dashed lines in Figs. 9.3 (a-b)) at different wavelengths. The measured maps of near-field amplitudes (square root of Eq. 4.9) under TE and TM illumination are shown in Fig. 9.4. For the TM case, the near-field enhancement is evident and we can see waves propagating outside the central spot area to the left ($-x$) and right ($+x$) sides, with the left-propagating waves being a bit stronger. For $\lambda_0 < d$, the propagating $\pm 1^{\text{st}}$ transmitted orders should make a major contribution to the asymmetrical near field. For $\lambda_0 > d$, however, the $\pm 1^{\text{st}}$ orders become evanescent and are bound to the air-metal interface. In particular, when λ_0 is around 1520-1540 nm, the phase-matching condition of SPPs is quasi-satisfied and the near field should largely consist of the excited SPPs.

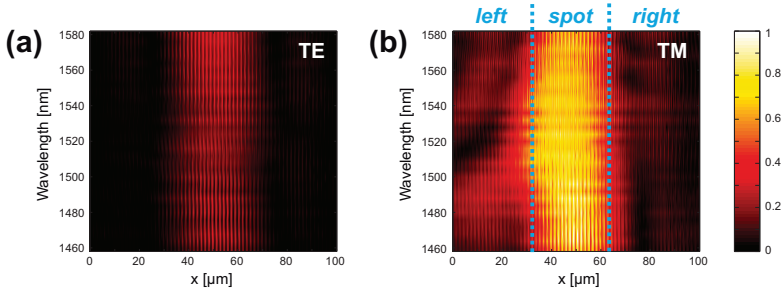


Figure 9.4: (Color online) Near-field amplitude (square root of the field intensity) scanned in x direction across the illumination spot: (a) TE (z -polarized) incidence, (b) TM (x -polarized) incidence. The scan length is $100\ \mu\text{m}$ and the wavelength is changed from 1460 to 1580 nm with a step of 4 nm. The spot diameter is about $20\ \mu\text{m}$. The amplitude scale is in arbitrary units.

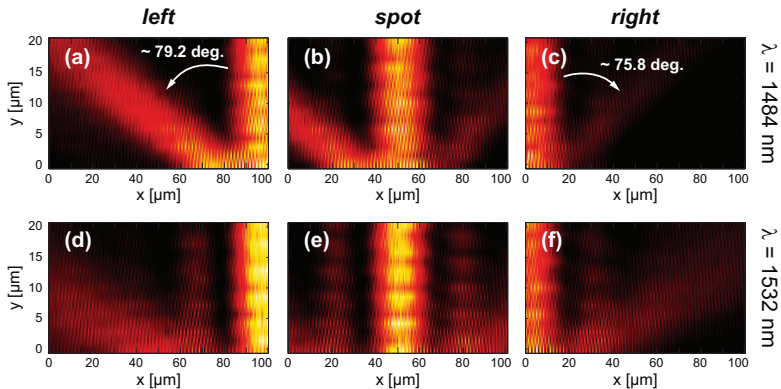


Figure 9.5: (Color online) x - y scan of the field intensity above the air-Au interface under TM illumination. (a-c): scans of the left side, across the central spot, and of the right side, respectively, at $\lambda_0 = 1484\ \text{nm}$. (d-f): the same as (a-c) but at $\lambda_0 = 1532\ \text{nm}$. Note that in this figure the origin of the y axis is moved to 500 nm above the air-metal interface for the convenience of illustration.

The propagating and evanescent behaviors can be particularly well identified through an xy scan. The shear-force feedback of the probe is switched off and xy intensity maps are acquired at a diffracting wavelength $\lambda_0 = 1484$ nm ($\lambda_0 < d$) as well as at a nondiffracting SPP-excitation wavelength $\lambda_0 = 1532$ nm ($\lambda_0 > d$). The scan starts with a horizontal line at about 500 nm from the sample surface and ends at 20 μm above the surface. As shown in Fig. 9.5, which clearly exhibits the different characteristics of the propagating and evanescent $\pm 1^{\text{st}}$ orders. At $\lambda_0 = 1484$ nm, the intensity maps clearly show the 0^{th} , $+1^{\text{st}}$ and -1^{st} propagating orders of the grating. The diffraction angles of the $+1^{\text{st}}$ and -1^{st} orders are respectively around 75.8 deg and 79.2 deg. With the help of Eq. 9.2, the 3.5 deg discrepancy indicates a light incidence at about 0.4 deg instead of exact normal incidence. Note that the numerically calculated diffraction efficiencies of the -1^{st} and $+1^{\text{st}}$ transmitted orders are 16.1 % and 1.6 %, respectively, at $\lambda_0 = 1484$ nm. At $\lambda_0 = 1532$ nm, the lateral beams spread over a broader area. This behavior indicates the progressive leakage of the SPPs at the Au-air interface back to the air [53].

9.5 Analysis in the Fourier domain

The near-field composition on a nanostructured metal surface has been thoroughly investigated by previous authors [129–132]. It was found that, at near-infrared frequencies, the near field consists of not only SPPs but also a surface wave with radiative and evanescent field components (called the REC wave in the following). The REC wave creeps along the interface, having a wave number very close to k_{SPP} but not exactly the same [129].

We analyze the near-field composition by performing a fast Fourier transform (FFT) of the measured complex field as explained in Sec. 4.2.3. We only consider the TM-polarized field with the heterodyne signal at 30 kHz. The spectra with the same object beam but interfering with the other reference beam (i.e. at 50 kHz) are indeed very similar. A high resolution scan (512 points) is acquired over 100 μm across the central spot.

Then we performed the FFT analysis on the complex fields in the left and right sides of the spot separately in the same scan so as to compare the left-

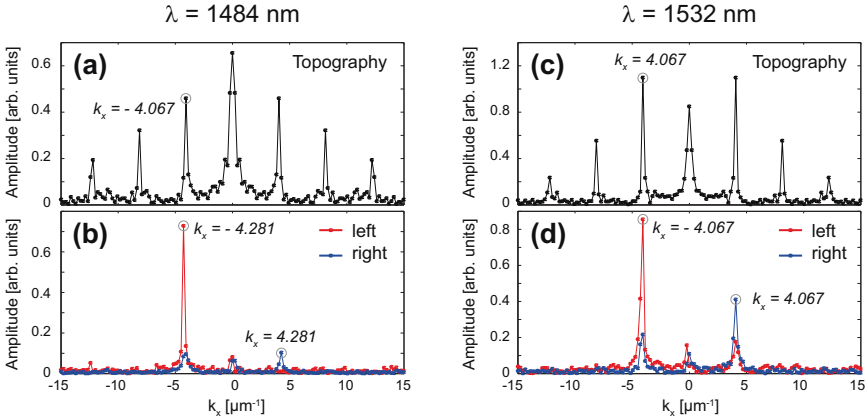


Figure 9.6: (Color online) FFT analysis of the grating topography and the TM fields measured in the left and right regions indicated in Fig. 9.4 (b), for (a-b) $\lambda_0 = 1484$ nm and (c-d) $\lambda_0 = 1532$ nm.

and right-propagating field strengths quantitatively. Moreover, the central spot intensity is so strong that the detection system saturates when the probe crosses it. Then, the lock-in amplifiers of the detection system needs time to exit the overload regime when the probe moves out. We therefore exclude the central spot area and select a $30 \mu\text{m}$ wide region in both the left and right sides for our analysis, as indicated in Fig. 9.4 (b). The number of sampling points in each region is therefore 150. The resolution in the Fourier space becomes (Eq. 4.15) $dk_x \simeq 2.1 \cdot 10^5 \text{ m}^{-1}$.

We perform the FFT analysis on the wavelength range of $1460 - 1580$ nm. Figure 9.6 demonstrates two typical FFT spectra of the fields (at $\lambda_0 = 1484$ nm and $\lambda_0 = 1532$ nm) as well as those of the sample topography. Note that the real topography signal produces a symmetric FFT spectrum. A main characteristic of the spectra is that for $\lambda_0 < d$ the left/right fields always have a peak k component larger than that of the topography (e.g., $k_{field} = 4.281 \mu\text{m}^{-1} > k_{topo} = 4.067 \mu\text{m}^{-1}$ in Fig. 9.6 (a-b)), which should correspond to the REC wave as there is no SPP excitation in this regime.

For $\lambda_0 > d$, however, the $\pm 1^{\text{st}}$ orders become evanescent and the peak k value

λ [nm]	$r_{\text{exp_fwd}}$	$r_{\text{exp_bwd}}$	$r_{\text{exp_mean}}$	r_{num}
1524	2.02	2.03	2.03	1.50
1528	1.88	1.74	1.81	1.58
1532	2.08	1.64	1.86	1.70
1536	1.33	1.49	1.41	1.84
1540	2.11	1.59	1.85	1.99

Table 9.1: Experimental and numerically calculated asymmetrical coupling ratio r_{\pm} of the SPPs on the BLACES sample. $r_{\text{exp_fwd}}$ and $r_{\text{exp_bwd}}$ are experimental results obtained from forward and backward acquisitions, respectively, and $r_{\text{exp_mean}}$ is the mean value of the two. r_{num} is the numerically calculated ratio (see [118] for calculation details).

of the field FFT spectra is the same as that of the topography spectra, as shown in Figs. 9.6 (c-d). This is a characteristic of the SPP excitation as the phase-matching condition Eq. 9.3 leads to $k_{SPP} = k_{\text{topo}}$. In Fig. 9.6 (d), the left-field spectrum has a dominant negative k component representing a SPP wave propagating in $-x$ direction and the right field has a dominant SPP wave propagating in $+x$ direction. The amplitude ratio of the two peaks can to some extent demonstrate the asymmetrical coupling effect of SPPs because in this regime the SPPs contribute the most to the near field. To best avoid the influence of the detection system saturation, we have implemented both forward and backward acquisitions (i.e., the probe scans from left to right and also from right to left). The asymmetrical coupling ratio r_{\pm} derived from the experimental data is listed in Tab. 9.1 for several wavelengths in the SPP excitation regime, which are also compared with the numerical results. We can see a certain correspondence between the experimental and theoretical ratios.

We should note that at SPP excitation the REC wave is still present. Therefore, the experimental ratio in Tab. 9.1 is just an estimate of the asymmetrical excitation of SPPs rather than an exact evaluation. To have a close look at the surface wave composition, we have performed an FFT analysis on the field

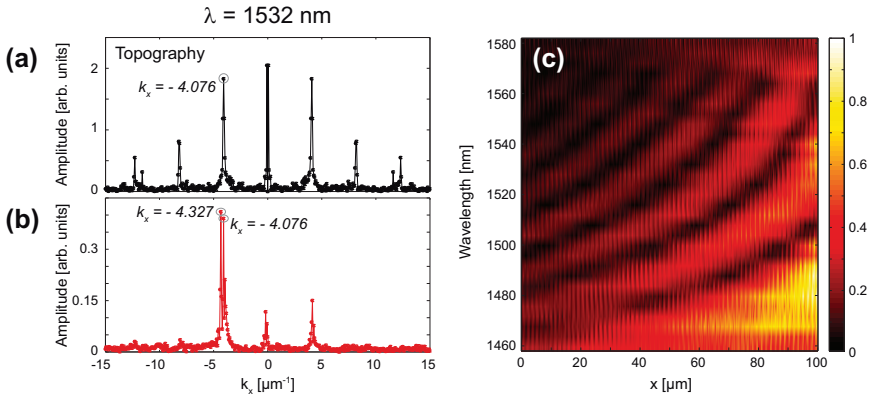


Figure 9.7: (Color online) (a-b) FFT analysis of the grating topography and the TM field measured on the left side of the spot with $L = 100 \mu\text{m}$, $N = 512$, and $\lambda_0 = 1532 \text{ nm}$. (c) Similar scan as in Fig. 9.4 on the left side of the spot under TM illumination. The color scale is normalized to the maximum value.

scanned only on the left side of the spot with the best resolution ($L = 100 \mu\text{m}$ and $N = 512$), as shown in Figs. 9.7 (a-b). The grating period derived from $k_{\text{topo}} = 4.076 \mu\text{m}^{-1}$ is

$$d \pm \delta d = \frac{2\pi}{k} \pm \frac{2\pi}{k^2} \delta k = 1.541 \pm 0.024 \mu\text{m}, \quad (9.4)$$

which coincides with our sample design. We can see that within the main peak there are two subpeaks $k_{\text{field}} = 4.076 \mu\text{m}^{-1} = k_{\text{topo}}$ and $k_{\text{field}} = 4.327 \mu\text{m}^{-1} > k_{\text{topo}}$ (the negative sign representing the propagation direction is omitted); the former is the SPP wave and the latter is the REC wave. It is known that when the SPPs are excited and are propagating on the surface of the grating, the SPPs are scattered by the periodic features into SPPs (primarily the backward propagating SPP wave corresponding to the small positive k peak in Fig. 9.7 (b)) and into leakage radiation [53]. This leads to the broadening of the spectral peak as well as its splitting into subpeaks. The interference of the SPP wave and the REC wave makes a major contribution (as their k peaks are dominant in the spectrum of Fig. 9.7 (b)) to the near-field interference pattern, which can be seen clearly as the main bright-dark beat fringes in Fig. 9.7 (c). The fringe spacing calculated from

the beat frequency $\Delta k = 4.327 - 4.076 = 0.251 \mu\text{m}^{-1}$ is $25 \mu\text{m}$ at $\lambda_0 = 1532 \text{ nm}$, which is consistent with that observed in Fig. 9.7 (c). The other small features in the near-field pattern of Fig. 9.7 (c), such as the additional modulation around $\lambda_0 = 1540 \text{ nm}$, may be ascribed to other interference processes. For example, the SPP waves may be scattered by the triangular surface features and propagate in different directions, leading to the other minor k values within the main k peak in Fig. 9.7 (b). These minor interactions are more complicated and are beyond the scope of the current study.

9.6 Conclusion

The optical response of a BLACES grating illuminated at normal incidence has been characterized with the MH-SNOM, both in the spatial and Fourier domain. The asymmetrical coupling effects of SPPs were found to be in satisfactory agreement with the theoretical results. Moreover, with a fine resolution in the Fourier domain, we were able to discriminate between two distinct phenomena having very similar in-plane wave vectors: the SPPs and the REC waves.

This work is part of a more general and comparative survey between slanted and BLACES 1D gratings. The major content of this chapter has been published in [118].

10

Conclusions

To characterize an electromagnetic field, the amplitude is not always sufficient. It is often essential to have the knowledge of its phase and polarization. The main objective of this work was to set up an optical instrument sensitive to the amplitude, phase and polarization with subwavelength resolution. For this purpose, we have developed a coherent scanning probe system based on the combination of a multi-heterodyne interferometer with a Scanning Near-field Optical Microscope (SNOM). On the one hand, the standard heterodyne method increases by a factor of 2 the detection sensitivity with respect to direct detection. Typical optical signals of 5 pW have been detected, leading to a phase accuracy of 0.18 deg. On the other hand, the multi-heterodyne technique allows the simultaneous detection, in amplitude and phase, of the optical response of a structure illuminated with two orthogonally polarized fields. In addition, these two responses are independently projected onto a basis consisting of two orthogonally and linearly

polarized beams, leading, in particular cases (paraxial near fields), to a complete measurement of the field. Furthermore, the microscope is tunable, with wavelengths ranging from 1460 to 1580 nm. Such a capability is indeed extremely useful when studying bandgap structures or measuring dispersion relations, for example.

Our instrument has been tested on different structures sustaining Surface Electromagnetic Waves (SEWs), i.e., optical modes confined at the interface between two media. Most of the samples were based on a silicon nitride multilayer sustaining a particular class of SEWs known as Bloch Surface Waves (BSWs). These modes have been excited in the Kretschmann configuration. We first performed a detailed analysis of the BSWs within a bare multilayer. Through a direct near-field visualization of the mode, we have directly measured its relevant characteristics such as the propagation constant, the decay length and the exponential decay from the surface. A field enhancement of about 100 with respect to a simple glass-air interface has also been demonstrated. We have found a good agreement with far-field estimations and/or calculations.

The BSW propagation within the bare multilayer was then perturbed by the presence of a shallow dielectric grating deposited onto the top interface. We have designed this subwavelength grating in order to create a bandgap within the wavelength range available to our instrument. The field distribution has been investigated at the band edges as well as outside of the bandgap. As expected from photonic crystal theory, we have found that the fields at the band edges consist of standing waves with energy maxima localized in the grating low- and high-index regions (air and polymer, respectively) for the high- and low-energy band edges, respectively. Outside of the bandgap, the BSW shows either forward or backward propagating behaviors, depending on its position either on the “regular” or back-folded dispersion curve. We have also perturbed the BSW propagation by depositing a thin and flat polymeric coating on top of the multilayer. We have demonstrated that, at the straight interface between the bare and coated multilayer, the BSW propagation sustains a refractive deflection fully described by Snell’s law, accounting for the effective indices in both regions. This result is of importance because it permits consideration of the BSW as a two-dimensional (2D) phenomenon, allowing the use of simple 2D laws for the conception of BSW

devices.

Finally, we have deposited a very thin polymeric ridges (thickness $< \lambda/10$) onto the multilayer surface and shown that they can act as BSW waveguides. Using a $4.5 \mu\text{m}$ wide and 140 nm high waveguide, we have experimentally demonstrated that the structure sustains three modes which can be selectively excited by tuning the wavelength and choosing the incident polarization. Their individual dispersion relations have also been measured. Accounting for the ability of our microscope to simultaneously detect in amplitude and phase two arbitrary orthogonal components of the near field, we have performed a numerical post-processing on the experimental data, and retrieved the transverse and longitudinal components of each of the modes. These results were found to be in very good agreement with calculations. This fast and simple technique is based on *a priori* information about the field distribution. At the low cost of adding a second orthogonal reference in standard heterodyne SNOM, we believe that this technique may be extremely useful, especially for the characterization of guiding structures, microcavities, resonators, etc. We can even think of applying this method without any preliminary information, by analyzing the structure of the detected field with mathematical tools such as symmetries.

All of these experiments have provided important insights into BSWs and their interaction with ultra-thin dielectric structures. Although BSWs cannot be laterally confined as much as surface plasmons polaritons in metals, for example, they are very attractive for sensing applications and/or reasonably dense 2D integrated optics. The combination of these two fields may also lead to new ultra-thin waveguide-based sensors in which the guiding structures are realized with functionalized molecular layers. The advantages of BSWs essentially arise from the possibility of engineering the BSW dispersion relation by designing the multilayer structure (choice of the materials and layer thicknesses) and from the field enhancement that occurs at the multilayer surface. For example, by properly choosing the dielectric materials, one can potentially design BSWs at any wavelength with very low losses, i.e., long propagation distances. Furthermore, in contrast to conventional waveguide-based sensors for which the penetration depth is fixed by the waveguide structure (materials and dimensions), the tail of the BSWs can be made arbitrarily short or long in the analyte, depending on

the need to detect volume or surface changes. One can also design the multilayer structure in such a way that it sustains several BSWs at a certain wavelength.

At the end of this work, we have presented measurements involving another class of SEWs, Surface Plasmons Polaritons (SPPs). The goal was to demonstrate the expected asymmetrical coupling of SPPs at normal incidence on a binary structure made of subwavelength triangular holes in a thin gold layer. Although weak, the asymmetrical coupling has been observed. A detailed analysis of the spatial spectra at the sample surface has revealed that SPPs were not the only components constituting the near field. The presence of creeping waves has indeed been found with propagation constants very close to those of the SPPs.

The main goals of this thesis have been achieved. We have set up an instrument for amplitude, phase and polarization sensitive measurements and its performance has been demonstrated using several samples. Its capability of simultaneously measuring the response of a sample (in amplitude and phase) illuminated with two orthogonally polarized beams makes it very attractive for the study of structures presenting strong polarization effects. Moreover, its functionalities can be extended, under specific conditions, to the integral measurement of the state of polarization at the sample surface. This instrument may therefore be helpful in several domains, particularly for the understanding and the characterization of optical micro- and nano-structures.

List of abbreviations

AFM Atomic Force Microscope

AI Analog Input

AO Analog Output

AOM Acousto-Optic Modulator

BLACES Blazed Area-Coded Effective-Medium Structures

BS Beam Splitter

BSW Bloch Surface Wave

DAQ Data Acquisition Card

DLSPPW Dielectric-Loaded Surface Plasmon Polariton Waveguide

EBL Electron-Beam Lithography

FEM Finite Element Method

FFT Fast Fourier Transform

FIFO First In First Out

GUI Graphical User Interface

IMI Insulator-Metal-Insulator

MH-SNOM Multi-Heterodyne Scanning Near-Field Optical Microscope

MIM Metal-Insulator-Metal

OP-AMP Operational Amplifier

OTF Optical Transfer Function

PBS Polarizing Beam Splitter

PC Photonic Crystal

PECVD Plasma Enhanced Chemical Vapor Deposition

PID Proportional Integral Derivative

PMF Polarization Maintaining Fiber

SEM Scanning Electron Microscope

SEW Surface Electromagnetic Wave

SMF Single Mode Fiber

SNOM Scanning Near-Field Optical Microscope

SNR Signal to Noise Ratio

SOP State Of Polarization

SPP Surface Plasmon Polariton

STM Scanning Tunneling Microscope

TE Transverse Electric

TM Transverse Magnetic

Bibliography

- [1] M. Paesler and P. Moyer, *Near-field Optics: Theory, Instrumentation and Applications*, John Wiley & Sons (1996).
- [2] E. H. Synge, “A suggested method for extending microscopic resolution into the ultra-microscopic region,” *Philosophical Magazine* **6**, 356–362 (1928).
- [3] G. Binnig, H. Rohrer, C. Gerber, and E. Weibel, “Surface Studies by Scanning Tunneling Microscopy,” *Physical Review Letters* **49**, 57–61 (1982).
- [4] G. Binnig, C. F. Quate, and C. Gerber, “Atomic Force Microscope,” *Physical Review Letters* **56**, 930–933 (1986).
- [5] D. W. Pohl, W. Denk, and M. Lanz, “Optical Stethoscopy - Image Recording With Resolution $\lambda/20$,” *Applied Physics Letters* **44**, 651–653 (1984).
- [6] A. Lewis, M. Isaacson, A. Harootunian, and A. Muray, “Development of a 500-Å spatial-resolution light-microscope. Light is efficiently transmitted through $\lambda/16$ diameter apertures,” *Ultramicroscopy* **13**, 227–231 (1984).
- [7] M. L. M. Balistreri, J. P. Korterik, L. Kuipers, and N. F. van Hulst, “Local observations of phase singularities in optical fields in waveguide structures,” *Physical Review Letters* **85**, 294–297 (2000).
- [8] A. Nesci, R. Dändliker, and H. P. Herzig, “Quantitative amplitude and phase measurement by use of a heterodyne scanning near-field optical microscope,” *Optics Letters* **26**, 208–210 (2001).
- [9] A. Huber, N. Ocelic, D. Kazantsev, and R. Hillenbrand, “Near-field imaging of mid-infrared surface phonon polariton propagation,” *Applied Physics Letters* **87**, 081103 (2005).

- [10] B. Deutsch, R. Hillenbrand, and L. Novotny, “Near-field amplitude and phase recovery using phase-shifting interferometry,” *Optics Express* **16**, 494–501 (2008).
- [11] F. Hitzel, A. Hangleiter, S. Miller, A. Weimar, G. Bruderl, A. Lell, and V. Harle, “High-resolution near-field spectroscopy investigation of GaN laterally overgrown structures on SiC,” *Applied Physics Letters* **82**, 4071–4073 (2003).
- [12] M. Brehm, A. Schliesser, and F. Keilmann, “Spectroscopic near-field microscopy using frequency combs in the mid-infrared,” *Optics Express* **14**, 11222–11233 (2006).
- [13] E. Betzig, J. K. Trautman, J. S. Weiner, T. D. Harris, and R. Wolfe, “Polarization contrast in near-field scanning optical microscopy,” *Applied Optics* **31**, 4563–4568 (1992).
- [14] K. Nakajima, Y. Mitsuoka, N. Chiba, H. Muramatsu, T. Ataka, K. Sato, and M. Fujihira, “Polarization effect in scanning near-field optic/atomic-force microscopy (SNOM/AFM),” *Ultramicroscopy* **71**, 257–262 (1998).
- [15] M. García-Parajó, B. de Bakker, M. Koopman, A. Cambi, F. de Lange, C. Figdor, and N. van Hulst, “Near-field fluorescence microscopy,” *NanoBioTechnology* **1**, 113–120 (2005).
- [16] N. F. van Hulst, J. A. Veerman, M. F. García-Parajó, and L. Kuipers, “Analysis of individual (macro)molecules and proteins using near-field optics,” *Journal of Chemical Physics* **112**, 7799–7810 (2000).
- [17] H. Gersen, E. M. H. P. van Dijk, J. P. Korterik, N. F. van Hulst, and L. Kuipers, “Phase mapping of ultrashort pulses in bimodal photonic structures: A window on local group velocity dispersion,” *Physical Review E* **70**, 066609 (2004).
- [18] T. Onuki, T. Tokizaki, Y. Watanabe, T. Tsuchiya, and T. Tani, “Nanometer-sized optical waveguides fabricated by anodic oxidation using a scanning near-field optical microscope,” *Applied Physics Letters* **80**, 4629–4631 (2002).

- [19] V. Likodimos, M. Labardi, L. Pardi, M. Allegrini, M. Giordano, A. Arena, and S. Patane, “Optical nanowriting on azobenzene side-chain poly-methacrylate thin films by near-field scanning optical microscopy,” *Applied Physics Letters* **82**, 3313–3315 (2003).
- [20] S. W. Hell and J. Wichmann, “Breaking the diffraction resolution limit by stimulated-emission: stimulated-emission-depletion fluorescence microscopy,” *Optics Letters* **19**, 780–782 (1994).
- [21] T. A. Klar, E. Engel, and S. W. Hell, “Breaking Abbe’s diffraction resolution limit in fluorescence microscopy with stimulated emission depletion beams of various shapes,” *Physical Review E* **64**, 066613 (2001).
- [22] R. Zengerle, “Light propagation in singly and doubly periodic planar waveguides,” *Journal of Modern Optics* **34**, 1589–1617 (1987).
- [23] M. Loncar, D. Nedeljkovic, T. P. Pearsall, J. Vuckovic, A. Scherer, S. Kuchinsky, and D. C. Allan, “Experimental and theoretical confirmation of Bloch-mode light propagation in planar photonic crystal waveguides,” *Applied Physics Letters* **80**, 1689–1691 (2002).
- [24] N. Le Thomas, R. Houdre, M. V. Kotlyar, D. O’Brien, and T. E. Krauss, “Exploring light propagating in photonic crystals with Fourier optics,” *Journal of the Optical Society of America B* **24**, 2964–2971 (2007).
- [25] N. Le Thomas, R. Houdre, L. H. Frandsen, J. Fage-Pedersen, A. V. Lavrinenko, and P. I. Borel, “Grating-assisted superresolution of slow waves in Fourier space,” *Physical Review B* **76**, 035103 (2007).
- [26] J. Jagerska, N. Le Thomas, R. Houdre, D. M. Beggs, D. O’Brien, and T. F. Krauss, “Coupling length of silicon-on-insulator directional couplers probed by Fourier-space imaging,” *Applied Physics Letters* **92**, 151106 (2008).
- [27] R. Dändliker, “Heterodyne, quasi-heterodyne and after,” in *Fringe 2005: the 5th international workshop on automatic processing of fringe patterns*, edited by W. Osten, pp. 65–73, Springer, Berlin Heidelberg, Germany (2006).

BIBLIOGRAPHY

- [28] R. Dändliker, “Heterodyne Holographic Interferometry,” in *Progress in Optics XVII*, edited by E. Wolf, chap. 1, pp. 1–84, North-Holland, Amsterdam, The Netherlands (1980).
- [29] H. D. Polster, J. Pastor, R. M. Scott, R. Crane, P. H. Langenbeck, R. Pilston, and R. Steinberg, “New developments in interferometry,” *Applied Optics* **8**, 538–542 (1969).
- [30] H. Z. Cummins and N. Knable, “Single sideband modulation of coherent light by Bragg reflection from acoustical waves,” *Proceedings of the IEEE* **51**, 1246 (1963).
- [31] W. H. Stevenson, “Optical frequency shifting by means of a rotating diffraction grating,” *Applied Optics* **9**, 649–652 (1970).
- [32] A. Yariv, *Optical Electronics in Modern Communications*, Oxford University Press, New York, USA (1997).
- [33] B. E. A. Saleh and M. C. Tech, *Fundamentals of photonics*, Wiley & Sons, New York, USA (1991).
- [34] W. H. Steel, *Interferometry*, Cambridge University Press, Cambridge, Great Britain (1983).
- [35] R. Dandliker, P. Tortora, L. Vaccaro, and A. Nesci, “Measuring three-dimensional polarization with scanning optical probes,” *Journal Of Optics A-Pure And Applied Optics* **6**, S18–S23 (2004).
- [36] P. Tortora, R. Dändliker, W. Nakagawa, and L. Vaccaro, “Detection of non-paraxial optical fields by optical fiber tip probes,” *Optics Communications* **259**, 876–882 (2006).
- [37] M. Vaez-Iravani and R. Toledo-Crow, “Phase-contrast and amplitude pseudoheterodyne interference near-field scanning optical microscopy,” *Applied Physics Letters* **62**, 1044–1046 (1993).
- [38] H. Masuda, Y. Suzui, A. Takayanagi, and N. Umeda, “Development of heterodyne photon scanning tunneling microscope,” in *International Workshop*

- on Interferometry*, pp. 141–142, Satellite Meeting for ICO-17, Wako, Japan (1996).
- [39] P. Tortora, M. Abashin, I. Marki, W. Nakagawa, L. Vaccaro, M. Salt, H. P. Herzig, U. Levy, and Y. Fainman, “Observation of amplitude and phase in ridge and photonic crystal waveguides operating at $1.55\ \mu\text{m}$ by use of heterodyne scanning near-field optical microscopy,” *Optics Letters* **30**, 2885–2887 (2005).
- [40] D. Charraut, C. Bainier, D. Courjon, and C. Girard, “Near-field phase measurement by Fourier analysis of the fringe pattern,” *Pure and Applied Optics* **6**, 491–502 (1997).
- [41] P. L. Phillips, J. C. Knight, J. M. Pottage, G. Kakarantzas, and P. S. J. Russell, “Direct measurement of optical phase in the near field,” *Applied Physics Letters* **76**, 541–543 (2000).
- [42] A. Bouhelier, M. R. Beversluis, and L. Novotny, “Near-field scattering of longitudinal fields,” *Applied Physics Letters* **82**, 4596–4598 (2003).
- [43] K. G. Lee, H. W. Kihm, J. E. Kihm, W. J. Choi, H. Kim, C. Ropers, D. J. Park, Y. C. Yoon, S. B. Choi, H. Woo, J. Kim, B. Lee, Q. H. Park, C. Lienau, and D. S. Kim, “Vector field microscopic imaging of light,” *Nature Photonics* **1**, 53–56 (2007).
- [44] M. Burresti, R. J. P. Engelen, A. Opheij, D. van Oosten, D. Mori, T. Baba, and L. Kuipers, “Observation of polarization singularities at the nanoscale,” *Physical Review Letters* **102**, 033902 (2009).
- [45] S. Vignolini, F. Intonti, F. Riboli, D. S. Wiersma, L. Balet, L. H. Li, M. Francardi, A. Gerardino, A. Fiore, and M. Gurioli, “Polarization-sensitive near-field investigation of photonic crystal microcavities,” *Applied Physics Letters* **94**, 163102 (2009).
- [46] L. Novotny and B. Hecht, *Principles of Nano-Optics*, Cambridge University Press, Cambridge, Great Britain (2006).

- [47] S. A. Teukolsky, W. H. Press, B. P. Flannery, and W. T. Vetterling, *Numerical recipes in pascal: the art of scientific computing*, Cambridge University Press, New York, USA (1989).
- [48] R. Hillenbrand and F. Keilmann, “Complex optical constants on a subwavelength scale,” *Physical Review Letters* **85**, 3029–3032 (2000).
- [49] M. Sandtke and L. Kuipers, “Spatial distribution and near-field coupling of surface plasmon polariton Bloch modes,” *Physical Review B* **77**, 235439 (2008).
- [50] E. Descrovi, T. Sfez, L. Dominici, W. Nakagawa, F. Michelotti, F. Giorgis, and H.-P. Herzig, “Near-field imaging of Bloch surface waves on silicon nitride one-dimensional photonic crystals,” *Optics Express* **16**, 5453–5464 (2008).
- [51] A. D. Boardman, *Electromagnetic Surface Modes*, Wiley-Interscience, Toronto, Canada (1982).
- [52] W. Knoll, “Interfaces and thin films as seen by bound electromagnetic waves,” *Annual Review of Physical Chemistry* **49**, 569–638 (1998).
- [53] A. V. Zayats and I. I. Smolyaninov, “Near-field photonics: surface plasmon polaritons and localized surface plasmons,” *Journal of Optics A: Pure and Applied Optics* **5**, S16–S50 (2003).
- [54] W. L. Barnes, A. Dereux, and T. W. Ebbesen, “Surface plasmon subwavelength optics,” *Nature* **424**, 824–830 (2003).
- [55] J. LeGall, M. Olivier, and J. J. Greffet, “Experimental and theoretical study of reflection and coherent thermal emission by a SiC grating supporting a surface-phonon polariton,” *Physical Review B* **55**, 10105–10114 (1997).
- [56] R. Hillenbrand, “Towards phonon photonics: scattering-type near-field optical microscopy reveals phonon-enhanced near-field interaction,” *Ultramicroscopy* **100**, 421–427 (2004).
- [57] D. Artigas and L. Torner, “Dyakonov surface waves in photonic metamaterials,” *Physical Review Letters* **94**, 013901 (2005).

- [58] R. D. Meade, K. D. Brommer, A. M. Rappe, and J. D. Joannopoulos, "Electromagnetic Bloch Waves At The Surface Of A Photonic Crystal," *Physical Review B* **44**, 10961–10964 (1991).
- [59] W. M. Robertson, G. Arjavalingam, R. D. Meade, K. D. Brommer, A. M. Rappe, and J. D. Joannopoulos, "Observation of surface photons on periodic dielectric arrays," *Optics Letters* **18**, 528–530 (1993).
- [60] M. Sarrazin and J. . P. Vigneron, "Bounded modes to the rescue of optical transmission," *Europhysics News* **38**, 27–31 (2007).
- [61] A. V. Kavokin, I. A. Shelykh, and G. Malpuech, "Lossless interface modes at the boundary between two periodic dielectric structures," *Physical Review B* **72**, 233102 (2005).
- [62] X. I. Saldana and G. G. Delacruz, "Electromagnetic surface waves in semi-infinite superlattices," *Journal of the Optical Society of America A: Optics Image Science and Vision* **8**, 36–40 (1991).
- [63] A. Shinn and W. M. Robertson, "Surface plasmon-like sensor based on surface electromagnetic waves in a photonic band-gap material," *Sensors and Actuators B-Chemical* **105**, 360–364 (2005).
- [64] J. Martorell, D. L. Sprung, and G. V. Morozov, "Surface TE waves on 1D photonic crystals," *Journal of Optics A: Pure And Applied Optics* **8**, 630–638 (2006).
- [65] P. Yeh, A. Yariv, and A. Y. Cho, "Optical surface waves in periodic layered media," *Applied Physics Letters* **32**, – (1978).
- [66] W. Ng, P. Yeh, P. C. Chen, and A. Yariv, "Optical surface-waves in periodic layered medium grown by liquid-phase epitaxy," *Applied Physics Letters* **32**, 370–371 (1978).
- [67] F. Ramos-Mendieta and P. Halevi, "Propagation constant – limited surface modes in dielectric superlattices," *Optics Communications* **129**, 1–5 (1996).

- [68] C. Vandembem, “Electromagnetic surface waves of multilayer stacks: coupling between guided modes and Bloch modes,” *Optics Letters* **33**, 2260–2262 (2008).
- [69] W. M. Robertson, “Experimental measurement of the effect of termination on surface electromagnetic waves in one-dimensional photonic bandgap arrays,” *Journal of Lightwave Technology* **17**, 2013–2017 (1999).
- [70] V. N. Konopsky and E. V. Alieva, “Photonic crystal surface waves for optical biosensors,” *Analytical Chemistry* **79**, 4729–4735 (2007).
- [71] F. Villa, L. E. Regalado, F. Ramos-Mendieta, J. Gaspar-Armenta, and T. Lopez-Rios, “Photonic crystal sensor based on surface waves for thin-film characterization,” *Optics Letters* **27**, 646–648 (2002).
- [72] M. Liscidini and J. E. Sipe, “Enhancement of diffraction for biosensing applications via Bloch surface waves,” *Applied Physics Letters* **91**, 253125 (2007).
- [73] E. Guillermain, V. Lysenko, R. Orobtcouk, T. Benyattou, S. Roux, A. Pilonnet, and P. Perriat, “Bragg surface wave device based on porous silicon and its application for sensing,” *Applied Physics Letters* **90**, 241116 (2007).
- [74] E. Descrovi, F. Frascella, B. Sciacca, F. Geobaldo, L. Dominici, and F. Michelotti, “Coupling of surface waves in highly defined one-dimensional porous silicon photonic crystals for gas sensing applications,” *Applied Physics Letters* **91**, 241109 (2007).
- [75] J. A. Gaspar-Armenta and F. Villa, “Band-structure properties of one-dimensional photonic crystals under the formalism of equivalent systems,” *Journal of the Optical Society of America B* **21**, 405–412 (2004).
- [76] L. F. Li, J. Chandezon, G. Granet, and J. P. Plumey, “Rigorous and efficient grating-analysis method made easy for optical engineers,” *Applied Optics* **38**, 304–313 (1999).
- [77] P. Yeh, A. Yariv, and C. S. Hong, “Electromagnetic propagation in periodic stratified media .1. General Theory,” *Journal of the Optical Society of America* **67**, 423–438 (1977).

- [78] E. Descrovi, F. Giorgis, L. Dominici, and F. Michelotti, "Experimental observation of optical bandgaps for surface electromagnetic waves in a periodically corrugated one-dimensional silicon nitride photonic crystal," *Optics Letters* **33**, 243–245 (2008).
- [79] R. Ulrich, "Theory of prism-film coupler by plane-wave analysis," *Journal of the Optical Society of America* **60**, 1337–1350 (1970).
- [80] E. Bontempi, L. E. Depero, L. Sangaletti, F. Giorgis, and C. F. Pirri, "Growth process analysis of a-Si_{1-x}N_x:H films probed by X-ray reflectivity," *Materials Chemistry and Physics* **66**, 172–176 (2000).
- [81] G. Vitrant, R. Reinisch, and F. Kajzar, "M-line spectroscopy for nonlinear characterization of polymeric waveguides," *Optical Engineering* **34**, 3418–3426 (1995).
- [82] E. F. Y. Kou and T. Tamir, "Excitation of surface-plasmons by finite width beams," *Applied Optics* **28**, 1169–1177 (1989).
- [83] A. S. Ramirez-Duverger, J. Gaspar-Armenta, and R. Garcia-Llamas, "Surface wave effect on light scattering from one-dimensional photonic crystals," *Optics Communications* **277**, 302–309 (2007).
- [84] R. C. Nesnidal and T. G. Walker, "Multilayer dielectric structure for enhancement of evanescent waves," *Applied Optics* **35**, 2226–2229 (1996).
- [85] A. Bouhelier and G. P. Wiederrecht, "Surface plasmon rainbow jets," *Optics Letters* **30**, 884–886 (2005).
- [86] P. L. Rochon and L. Levesque, "Standing wave surface plasmon mediated forward and backward scattering," *Optics Express* **14**, 13050–13055 (2006).
- [87] W. L. Barnes, T. W. Preist, S. C. Kitson, and J. R. Sambles, "Physical origin of photonic energy gaps in the propagation of surface plasmons on gratings," *Physical Review B* **54**, 6227–6244 (1996).
- [88] C. J. Alleyne, A. G. Kirk, R. C. McPhedran, N. A. P. Nicorovici, and D. Maystre, "Enhanced SPR sensitivity using periodic metallic structures," *Optics Express* **15**, 8163–8169 (2007).

BIBLIOGRAPHY

- [89] A. J. Benahmed and C. M. Ho, “Bandgap-assisted surface-plasmon sensing,” *Applied Optics* **46**, 3369–3375 (2007).
- [90] J. C. Weeber, A. Bouhelier, G. C. des Francs, L. Markey, and A. Dereux, “Submicrometer in-plane integrated surface plasmon cavities,” *Nano Letters* **7**, 1352–1359 (2007).
- [91] E. Meyer, H. J. Hug, and R. Bennewitz, *Scanning Probe Microscopy: The Lab on a Tip*, Berlin, Germany, Springer (2004).
- [92] T. Sfez, E. Descrovi, L. Dominici, W. Nakagawa, F. Michelotti, F. Giorgis, and H. P. Herzig, “Near-field analysis of surface electromagnetic waves in the bandgap region of a polymeric grating written on a one-dimensional photonic crystal,” *Applied Physics Letters* **93**, 061108 (2008).
- [93] S. Griesing, A. Englisch, and U. Hartmann, “Refractive and reflective behavior of polymer prisms used for surface plasmon guidance,” *Optics Letters* **33**, 575–577 (2008).
- [94] D. G. Zhang, X. C. Yuan, J. Bu, G. H. Yuan, Q. Wang, J. Lin, X. J. Zhang, P. Wang, H. Ming, and T. Mei, “Surface plasmon converging and diverging properties modulated by polymer refractive structures on metal films,” *Optics Express* **17**, 11315–11320 (2009).
- [95] T. Kitazawa, S. Miyanishi, Y. Murakami, K. Kojima, and A. Takahashi, “Refraction of surface plasmon-polaritons at Au-Al boundaries observed by scanning near-field optical microscopy,” *Physical Review B* **77**, 193404 (2008).
- [96] A. L. Campillo, J. W. P. Hsu, K. R. Parameswaran, and M. M. Fejer, “Direct imaging of multimode interference in a channel waveguide,” *Optics Letters* **28**, 399–401 (2003).
- [97] T. Holmgaard and S. I. Bozhevolnyi, “Theoretical analysis of dielectric-loaded surface plasmon-polariton waveguides,” *Physical Review B* **75**, 245405 (2007).

- [98] T. Sfez, E. Descrovi, L. Yu, M. Quaglio, L. Dominici, W. Nakagawa, F. Michelotti, F. Giorgis, and H. P. Herzig, “Two-dimensional optics on silicon nitride multilayer: Refraction of Bloch surface waves,” *Appl. Phys. Lett.* **96**, 151101–3 (2010).
- [99] S. Lal, S. Link, and N. J. Halas, “Nano-optics from sensing to waveguiding,” *Nature Photonics* **1**, 641–648 (2007).
- [100] S. I. Bozhevolnyi, ed., *Plasmonic nanoguides and circuits*, Pan Stanford Publishing Pte Ltd, Singapore (2008).
- [101] P. Berini, R. Charbonneau, and N. Lahoud, “Long-range surface plasmons on ultrathin membranes,” *Nano Letters* **7**, 1376–1380 (2007).
- [102] S. A. Maier, P. G. Kik, H. A. Atwater, S. Meltzer, E. Harel, B. E. Koel, and A. A. G. Requicha, “Local detection of electromagnetic energy transport below the diffraction limit in metal nanoparticle plasmon waveguides,” *Nature Materials* **2**, 229–232 (2003).
- [103] G. Lévêque and R. Quidant, “Channeling light along a chain of near-field coupled gold nanoparticles near a metallic film,” *Optics Express* **16**, 22029–22038 (2008).
- [104] A. V. Akimov, A. Mukherjee, C. L. Yu, D. E. Chang, A. S. Zibrov, P. R. Hemmer, H. Park, and M. D. Lukin, “Generation of single optical plasmons in metallic nanowires coupled to quantum dots,” *Nature* **450**, 402–406 (2007).
- [105] R. F. Oulton, V. J. Sorger, D. A. Genov, D. F. P. Pile, and X. Zhang, “A hybrid plasmonic waveguide for subwavelength confinement and long-range propagation,” *Nature Photonics* **2**, 496–500 (2008).
- [106] J. Dintinger and O. J. F. Martin, “Channel and wedge plasmon modes of metallic V-grooves with finite metal thickness,” *Optics Express* **17**, 2364–2374 (2009).
- [107] R. Zia, M. D. Selker, P. B. Catrysse, and M. L. Brongersma, “Geometries and materials for subwavelength surface plasmon modes,” *Journal of the Optical Society of America A* **21**, 2442–2446 (2004).

BIBLIOGRAPHY

- [108] J. A. Dionne, L. A. Sweatlock, H. A. Atwater, and A. Polman, “Plasmon slot waveguides: Towards chip-scale propagation with subwavelength-scale localization,” *Physical Review B* **73**, 035407 (2006).
- [109] T. Goto, Y. Katagiri, H. Fukuda, H. Shinojima, Y. Nakano, I. Kobayashi, and Y. Mitsuoka, “Propagation loss measurement for surface plasmon-polariton modes at metal waveguides on semiconductor substrates,” *Applied Physics Letters* **84**, 852–854 (2004).
- [110] T. Holmgaard, S. I. Bozhevolnyi, L. Markey, A. Dereux, A. V. Krasavin, P. Bolger, and A. V. Zayats, “Efficient excitation of dielectric-loaded surface plasmon-polariton waveguide modes at telecommunication wavelengths,” *Physical Review B* **78**, 165431 (2008).
- [111] C. A. Barrios, K. B. Gylfason, B. Sanchez, A. Griol, H. Sohlstrom, M. Hologado, and R. Casquel, “Slot-waveguide biochemical sensor,” *Optics Letters* **32**, 3080–3082 (2007).
- [112] J.-J. Greffet and R. Carminati, “Image formation in near-field optics,” *Progress in Surface Science* **56**, 133–237 (1997).
- [113] S. I. Bozhevolnyi, B. Vohnsen, and E. A. Bozhevolnaya, “Transfer functions in collection scanning near-field optical microscopy,” *Optics Communications* **172**, 171–179 (1999).
- [114] M. Born and E. Wolf, *Principles of Optics*, Cambridge University Press, Cambridge, United Kingdom (1999).
- [115] E. Verhagen, M. Spasenovic, A. Polman, and L. Kuipers, “Nanowire plasmon excitation by adiabatic mode transformation,” *Physical Review Letters* **102**, 203904 (2009).
- [116] M. Spasenović, D. van Oosten, E. Verhagen, and L. Kuipers, “Measurements of modal symmetry in subwavelength plasmonic slot waveguides,” *Applied Physics Letters* **95**, 203109 (2009).
- [117] I. Stefanon, S. Blaize, A. Bruyant, S. Aubert, G. Lerondel, R. Bachelot, and P. Royer, “Heterodyne detection of guided waves using a scattering-type

- Scanning Near-Field Optical Microscope,” *Optics Express* **13**, 5553–5564 (2005).
- [118] B. F. Bai, X. F. Meng, J. Laukkanen, T. Sfez, L. B. Yu, W. Nakagawa, H. P. Herzig, L. F. Li, and J. Turunen, “Asymmetrical excitation of surface plasmon polaritons on blazed gratings at normal incidence,” *Physical Review B* **80**, 035407 (2009).
- [119] E. Descrovi, T. Sfez, M. Quaglio, D. Brunazzo, L. Dominici, F. Michelotti, H. P. Herzig, O. J. F. Martin, and F. Giorgis, “Guided Bloch surface waves on ultra-thin polymeric ridges,” Submitted to *Nanoletters*, Manuscript ID: nl-2010-00481q (2010).
- [120] T. Sfez, E. Descrovi, L. Yu, D. Brunazzo, M. Quaglio, L. Dominici, W. Nakagawa, F. Michelotti, F. Giorgis, O. J. F. Martin, and H. P. Herzig, “Bloch surface waves in ultra-thin waveguides: near-field investigation of mode polarization and propagation,” Submitted to *Journal of the Optical Society of America B*, Manuscript ID: 124950 (2010).
- [121] S. A. Maier, *Plasmonic: Fundamentals and Applications*, Springer, New York, USA (2007).
- [122] D. Egorov, B. S. Dennis, G. Blumberg, and M. I. Haftel, “Two-dimensional control of surface plasmons and directional beaming from arrays of sub-wavelength apertures,” *Physical Review B* **70**, 033404 (2004).
- [123] J. Y. Laluet, E. Devaux, C. Genet, T. W. Ebbesen, J. C. Weeber, and A. Dereux, “Optimization of surface plasmons launching from subwavelength hole arrays: modelling and experiments,” *Optics Express* **15**, 3488–3495 (2007).
- [124] N. Bonod, E. Popov, L. F. Li, and B. Chernov, “Unidirectional excitation of surface plasmons by slanted gratings,” *Optics Express* **15**, 11427–11432 (2007).
- [125] E. G. Loewen and E. Popov, *Diffraction gratings and applications*, Marcel Dekker, New York, USA (1997).

BIBLIOGRAPHY

- [126] B. H. Kleemann, J. Ruoff, and R. Arnold, “Area-coded effective medium structures, a new type of grating design,” *Optics Letters* **30**, 1617–1619 (2005).
- [127] P. Lalanne, S. Astilean, P. Chavel, E. Cambril, and H. Launois, “Blazed binary subwavelength gratings with efficiencies larger than those of conventional echelette gratings,” *Optics Letters* **23**, 1081–1083 (1998).
- [128] H. Elfstrom, M. Kuitinen, T. Vallius, B. H. Kleemann, J. Ruoff, and R. Arnold, “Fabrication of blazed gratings by area-coded effective medium structures,” *Optics Communications* **266**, 697–703 (2006).
- [129] P. Lalanne and J. P. Hugonin, “Interaction between optical nano-objects at metallo-dielectric interfaces,” *Nature Physics* **2**, 551–556 (2006).
- [130] L. Chen, J. T. Robinson, and M. Lipson, “Role of radiation and surface plasmon polaritons in the optical interactions between a nano-slit and a nano-groove on a metal surface,” *Optics Express* **14**, 12629–12636 (2006).
- [131] L. Aigouy, P. Lalanne, J. P. Hugonin, G. Julie, V. Mathet, and M. Mortier, “Near-field analysis of surface waves launched at nanoslit apertures,” *Physical Review Letters* **98**, 153902 (2007).
- [132] H. T. Liu and P. Lalanne, “Microscopic theory of the extraordinary optical transmission,” *Nature* **452**, 728–731 (2008).

Acknowledgments

First of all, my gratitude goes towards my thesis advisor, *Prof. Hans Peter Herzig*. I gave me the chance to work within his research group and to believe in me during the “non-results” first years of my work. His availability is remarkable: a discussion with him requires just to knock on his door. I also wish to thank him for the material support. The set-up has involved a lot of costly devices and no compromise have been done, as compromises were never done even when unwanted surprises arose. A good quality work have therefore been possible.

I am also grateful to the members of the jury, *Prof. Vahid Sandoghdar*, *Dr. María-Pilar Bernal* and *Prof. Wataru Nakagawa* for their critical review of my thesis.

I specially want to thank *Wataru Nakagawa* for his supervision all along this work. He was the only person understanding well enough my set-up and with who I have been able to solve very detailed problems. Even with an ocean between us, he was always available for long phone calls. He also taught me how to write scientific papers. I will always be very grateful to him for all his precious advices.

At the time when the microscope became ready for measurements, I didn't have any interesting structure to characterize. A the same time (I should say at the right time!), *Emiliano Descrovi* came with the multilayer that have been the basis structure all along this work. He was also always available for long discussion and fruitful comments on my work.

I am very grateful to *Marcel Groccia* who was always ready to help me into the laboratory, specially when I had the laborious task of assessing electrical noise or unveil ground loops. Some of the important electronic devices involved in the set-up have also been designed and realized by himself.

BIBLIOGRAPHY

I thank a lot *Libo Yu* who did a very good and accurate laboratory work. This thesis could't have been achieved without her.

A special thanks goes to *Hicham Farah* who realized the robust core of the software driving the microscope. Its architecture has been very well thought, allowing important further modifications without difficulty.

Many thanks to *Olivier Scherler* who reviewed a part of the manuscript and provided me Illustrator tricks.

I am particularly grateful to all my colleagues (and friends) for the nice atmosphere in the group. I thank *Mister Kim* for the interesting discussions on interferometry, *Matthieu Roussey* for the jokes we shared, *Sylvain Herminjard* for the L^AT_EX advices, *Vincent Paeder* for his help on theoretical aspect in optics, *Gerben Boer* for the funny atmosphere he brought into the cafeteria, *Omar Manzardo* and *Christophe Weiteneder* for the interesting philosophical discussions, *Patrick Ruffieux* and *Irène Philipoussis* for the nice coffee break, *Valeria Musi* for some revisions of the manuscript, and all the other group members for their good mood!

Finally, all my best feelings go to *Angélique* with whom I am sharing my life. I am particularly grateful to her for the important “logistic support” without which such a work would have been very much difficult. She has been very patient and understanding, specially at the end of the thesis. Thank you Angélique.

Appendices

.1 Publications and conferences

Most of this work has been published as regular papers or at conferences.

Regular papers

- T. Sfez, E. Descrovi, L. Yu, D. Brunazzo, M. Quaglio, L. Dominici, W. Nakagawa, F. Michelotti, F. Giorgis, O. J. F. Martin and H. P. Herzig, “Bloch surface waves in ultra-thin waveguides: near-field investigation of mode polarization and propagation,” submitted to Journal of Optical Society of America B.
- E. Descrovi, T. Sfez, M. Quaglio, D. Brunazzo, L. Dominici, F. Michelotti, H. P. Herzig, O. J. F. Herzig, and F. Giorgis, “Guided Bloch Surface Waves on ultra-thin polymeric ridges,” submitted to Nanoletters.
- T. Sfez, E. Descrovi, L. Yu, M. Quaglio, L. Dominici, W. Nakagawa, F. Michelotti, F. Giorgis, and H. P. Herzig, “Two-dimensional optics on silicon nitride multilayer: refraction of Bloch surface waves,” Applied Physics Letters **96**, 151101 (2010).
- B. Bai, Xi. Meng, J. Laukkanen, T. Sfez, L. Yu, W. Nakagawa, H. P. Herzig, L. Li, and J. Turunen, “Asymmetrical excitation of surface plasmon polaritons on blazed gratings at normal incidence,” Physical Review B **80**, 035407 (2009).
- T. Sfez, E. Descrovi, L. Dominici, W. Nakagawa, F. Michelotti, F. Giorgis, and H. P. Herzig, “Near-field analysis of surface electromagnetic waves in the bandgap region of a polymeric grating written on a one-dimensional photonic crystal,” Applied Physics Letters **93**, 061108 (2008).
- E. Descrovi, T. Sfez, L. Dominici, W. Nakagawa, F. Michelotti, F. Giorgis, and H. P. Herzig, “Near-field imaging of Bloch surface waves on silicon nitride one-dimensional photonic crystals,” Optics Express **16**, 5454-5464 (2008).

Conferences and workshops

- **H. P. Herzig**, T. Sfez, T. Scharf, “Opportunities in microstructured photonics,” **EOS Topical Meeting on Diffractive Optics**, Koli, Finland (2010).
- **T. Sfez**, E. Descrovi, L. Yu, D. Brunazzo, M. Quaglio, L. Dominici, W. Nakagawa, F. Michelotti, F. Giorgis, O. J. F. Martin, and H. P. Herzig, “Phase and polarization-resolved near-field investigation of ultrathin waveguides for Bloch Surface Waves,” **Photonics Day**, Lausanne, Switzerland (2009), oral presentation.
- **E. Descrovi**, F. Giorgis, F. Michelotti, L. Dominici, B. Sciacca, F. Frascella, F. Geobaldo, T. Sfez, H. P. Herzig, “Bloch Surface Waves on dielectric photonic crystals for sensing applications,” **2009 DGaO/SIOF Joint Meeting**, Brescia, Italy (2009).
- **F. Michelotti**, L. Dominici, E. Descrovi, F. Giorgis, T. Sfez, W. Nakagawa, H. P. Herzig, “Experimental studies of surface electromagnetic waves propagation in truncated 1D, 1+1D and 1+2D inorganic/organic photonic crystals for gas- and bio- sensing applications,” **ECONOS 2009**, Frascati, Italy (2009).
- **T. Sfez**, E. Descrovi, L. Dominici, W. Nakagawa, F. Michelotti, F. Giorgis, and H. P. Herzig, “Multi-heterodyne scanning near-field microscopy applied to surface electromagnetic waves on flat and corrugated multilayers,” **EOS Annual Meeting 2008**, Paris, France (2008), oral presentation.
- **F. Michelotti**, L. Dominici, E. Descrovi, F. Giorgis, T. Sfez, W. Nakagawa, H. P. Herzig, “Experimental study of surface electromagnetic waves propagation in truncated 1D, 1+1D, 1+2D inorganic/organic photonic crystals for gas and bio sensing applications,” **International Workshop on Advances in Nanoscale Nonlinear Optics**, Roma, Italy (2008).
- **T. Sfez**, E. Descrovi, L. Dominici, W. Nakagawa, F. Michelotti, F. Giorgis, and H. P. Herzig, “Near-field analysis of surface electromagnetic waves

generated on flat and corrugated multilayers,” **NFO-10**, Buenos Aires, Argentina (2008), poster.

- **F. Michelotti**, L. Dominici, E. Descrovi, F. Giorgis, T. Sfez, W. Nakagawa, H.P. Herzig, “Far-and near-field study of surface electromagnetic waves on silicon nitride one-dimensional photonic crystals,” **New frontiers in micro and nano photonics**, Florence, Italy (2008).

Tristan Sfez

quai Perdonnet 14

25 January 1977

1800 Vevey

swiss citizen

e-mail: tristan.sfez@gmail.com

Education

2010 **PhD Student in Near-Field Optics**, *Optics and Photonics Technology Laboratory (OPT), Swiss Federal Institute of Technology Lausanne (EPFL), Switzerland**.

**formerly Applied Optics Laboratory, Université de Neuchâtel, Neuchâtel, Switzerland*

- ▶ development of a multi-heterodyne Scanning Near-field Optical Microscope (SNOM) for amplitude, phase and polarization measurements in the near field.
- ▶ near-field characterization of structures involving Surface Electromagnetic Waves.

2004 **MSc-BSc in Physics**, *EPFL, Switzerland*.

- ▶ MSc practical work at the *Indian Institute of Technology, Kanpur, India (4 months)*. Computer simulation of geometrical and electronic structures of carbon clusters doped with nitrogen or phosphorus.

Professional Experience

2010 **Research assistant**, *OPT, EPFL*.

- ▶ near-field optics and software development (Labview)
- ▶ supervision of undergraduate, master and PhD students
- ▶ teaching assistantship in *Modern and Advanced Optics*

2004 ▶ teaching assistantship of Physics, Mechanics and laboratory works, *EPFL*

- ▶ financial consulting, *Fidicon SA, Lausanne, Switzerland*

2002 **Analysis and development** of applications on ERP BaaN database

computer department at Jean Gallay SA, Geneva, Switzerland (7 months)

Research Interests

- ▶ near-field optics
- ▶ surface electromagnetic waves
- ▶ integrated optics
- ▶ two-dimensional optics

Publications

Journals T. Sfez, E. Descrovi, L. Yu, D. Brunazzo, M. Quaglio, L. Dominici, W. Nakagawa, F. Michelotti, F. Giorgis, O. J. F. Martin and H. P. Herzig, "*Bloch surface waves in ultra-thin waveguides: near-field investigation of mode polarization and propagation*," submitted.

E. Descrovi, T. Sfez, M. Quaglio, D. Brunazzo, L. Dominici, F. Michelotti, H. P. Herzig, O. J. F. Herzig, and F. Giorgis, "*Guided Bloch Surface Waves on ultra-thin polymeric ridges*," submitted.

T. Sfez, E. Descrovi, L. Yu, M. Quaglio, L. Dominici, W. Nakagawa, F. Michelotti, F. Giorgis, and H. P. Herzig, "Two-dimensional optics on silicon nitride multilayer: refraction of Bloch surface waves," *Applied Physics Letters* **96**, 151101 (2010).

B. Bai, Xi. Meng, J. Laukkanen, T. Sfez, L. Yu, W. Nakagawa, H. P. Herzig, L. Li, and J. Turunen, "Asymmetrical excitation of surface plasmon polaritons on blazed gratings at normal incidence," *Physical Review B* **80**, 035407 (2009).

T. Sfez, E. Descrovi, L. Dominici, W. Nakagawa, F. Michelotti, F. Giorgis, and H. P. Herzig, "Near-field analysis of surface electromagnetic waves in the bandgap region of a polymeric grating written on a one-dimensional photonic crystal," *Applied Physics Letters* **93**, 061108 (2008).

E. Descrovi, T. Sfez, L. Dominici, W. Nakagawa, F. Michelotti, F. Giorgis, and H. P. Herzig, "Near-field imaging of Bloch surface waves on silicon nitride one-dimensional photonic crystals," *Optics Express* **16**, 5454-5464 (2008).

Conference Abstracts

T. Sfez, E. Descrovi, L. Yu, D. Brunazzo, M. Quaglio, L. Dominici, W. Nakagawa, F. Michelotti, F. Giorgis, O. J. F. Martin, and H. P. Herzig, "Phase and polarization-resolved near-field investigation of ultrathin waveguides for Bloch Surface Waves," *Photonics Day, Lausanne, Switzerland (2009)*.

T. Sfez, E. Descrovi, L. Dominici, W. Nakagawa, F. Michelotti, F. Giorgis, and H. P. Herzig, "Multi-heterodyne scanning near-field microscopy applied to surface electromagnetic waves on flat and corrugated multilayers," *EOS Annual Meeting 2008, Paris, France (2008)*.

T. Sfez, E. Descrovi, L. Dominici, W. Nakagawa, F. Michelotti, F. Giorgis, and H. P. Herzig, "Near-field analysis of surface electromagnetic waves generated on flat and corrugated multilayers," *NFO-10, Buenos Aires, Argentina (2008)*.

Languages

French	mother tongue	Spanish	spoken skills
English	fluent	German	basic knowledge rapidly perfectible

Computer Skills

Office	Word, Excel, Powerpoint, Latex	Graphics	Illustrator, Photoshop
Languages	Labview, Pascal, Fortran, FoxPro XBASE, Clipper, VBA	OS	Windows, Linux

Hobbies

Reading literature and philosophy

Sports footrace

Travels South America (6 months) – India (6 months) – Mexico, Guatemala (1 month)